

**Ingenieur fakultät Bau Geo Umwelt
Lehrstuhl für Statik
der Technischen Universität München**

Design Process for the Shape Optimization of Pressurized Bulkheads as Components of Aircraft Structures

Pablo Andrés Suárez Espinoza

Vollständiger Abdruck der von der Ingenieur fakultät Bau Geo Umwelt der Technischen Universität München zur Erlangung des akademischen Grades eines

Doktor–Ingenieurs

genehmigten Dissertation.

Vorsitzender: Univ.-Prof. Dr.-Ing. habil. Fabian Duddeck

Prüfer der Dissertation:

1. Univ.-Prof. Dr.-Ing. Kai-Uwe Bletzinger

2. Univ.-Prof. Dr.-Ing. Horst Baier

Die Dissertation wurde am 30.12.2014 bei der Technischen Universität München eingereicht und durch die Ingenieur fakultät Bau Geo Umwelt am 05.05.2015 angenommen.

Design Process for the Shape Optimization of Pressurized Bulkheads as Components of Aircraft Structures.

Abstract

One of the most recent efforts in aircraft design is the replacement of aluminium structures by carbon fibre reinforced composites. Due to high material and manufacturing costs, doubly curved shapes covering big areas are preferred over simpler surfaces integrating several adjacent components in a single unit. In this context, CAD parameterization of surfaces allows design solutions by means of classical shape optimization. Related geometrical parameters are manipulated towards optimal design, generating innovative configurations and detailing which are beyond classical and experienced standards. The final examples of this work are optimized by reducing the overall weight. The final optimum is guided using stability and strength restrictions in order to assure the safety of the component. Geometrical considerations are also included due to operational reasons. A hierarchical design procedure is developed which results in a work flow from preliminary "parameter-free" form finding motivated by solving the minimal surface problem. The geometrical model for optimization is recovered by generating a single B-Spline surface patch which preserves continuity requirements over large regions characterized by important differences in curvature. The number of geometrical coefficients will be defined by the accuracy in surface generation and the required freedom in surface control. The hierarchical approach reduces the possibilities of ending with an unsatisfactory optimum when several local minima characterize the non-linear problem, as it is usually the case in shape optimal design. Geometrical non-linear analysis verifies the performance of the final optimum.



Acknowledgments

This dissertation was written during my time as research assistant at the Chair of Structural Analysis, Lehrstuhl für Statik at the Technische Universität München.

Firstly, I would like to express my sincere gratitude to my advisor Prof. Dr.-Ing. Kai-Uwe Bletzinger for giving me the possibility to work in his research group. I want to thank him not only for his constant guidance and support of my Ph.D study and related research, but also for his patience, and persistent motivation.

I would like to thank the rest of my thesis committee. Prof. Dr.-Ing. Horst Baier for his interest in my topic of research, and significant contribution as examiner of this thesis. Prof. Dr.-Ing. Fabian Duddeck, chairman in the final defense of the theses, for his valuable participation in the final discussions.

To all coworkers at the Chair of Structural Analysis for their cooperation and for giving me time and effort in providing essential knowledge. Thanks to Dr. Roland Wüchner for his fundamental and friendly advice.

I am also grateful to the people from EADS Deutschland, departments of Structural Concepts and Optimization and Special Analysis, for the financial support and the possibility to work on such an interesting topic. Thank you for your assistance and guidance: Markus Klug, Georg Spenninger, Fernaß Daoud, Gerd Schuhmacher, and other colleagues, with whom I had the great chance of discussing not only work-related subjects. I am especially thankful to Herbert Hörnlein; his vast experience, and close supervision together with the required quota of encouragement made this work possible.

To my family for their love and support at any time.

Finally, to my caring, loving, and supportive wife Monica, who provided me with emotional comfort and wise counsel especially when the times got rough.

Pablo Andrés Suárez Espinoza



Contents

1	Introduction	1
1.1	Motivation and Objectives	2
1.1.1	Design Process	3
1.2	State of the Art	5
1.2.1	FE-Software at Hand	5
1.2.2	Topological Study	6
1.2.3	Initial Concepts	7
1.2.4	Loading and support conditions	8
1.2.5	Material	10
1.3	Contents of this report	12
2	Review of Continuum Mechanics and FE-Formulation	13
2.1	Differential Geometry	13
2.2	Kinematics	15
2.2.1	Strain Measurements	16
2.3	Stress Measures	17
2.4	Constitutive Equations	17
2.5	Governing Equations of Motion	18
2.5.1	Principle of virtual work	18
2.5.2	Linearization of Equilibrium Equations	19
2.5.3	Variation and Linearization of Strain Tensors	21
2.5.4	Finite Element Discretization	22
2.5.5	Solution of the Equilibrium Equations	25

3	Form Finding	27
3.1	Overview of the method	27
3.2	Applications of formfinding	28
3.2.1	Form finding in the design of pressurized thin-walled shell structures	29
3.2.1.1	Computation of Equilibrium Shapes	29
3.2.1.2	Structural Analysis	33
3.3	Numerical Solution - Update Reference Strategy	33
3.3.1	Discretization and Linearization	35
3.3.2	Regularization Due to Incompatible Stress Field	36
3.4	Generation of Surfaces for Different Concepts	36
4	Free Form Surfaces in CAGD-Based Shape Optimization using B-Splines	39
4.1	Introduction	40
4.2	Free Form Surfaces - Parametrical Representation	40
4.3	Shape Modification	41
4.3.1	Geometrical Model and its Parameterization	42
4.3.2	B-Splines	44
4.3.2.1	Basis Functions	45
4.3.2.2	Knot Vector	46
4.3.3	Continuity Conditions	46
4.3.4	NURBS	47
4.3.4.1	Homogeneous Representation	49
4.3.4.2	Weights	50
4.4	Surface Fitting - Surface Construction	52
4.4.1	Parameterization of data	53
4.4.2	Knot vector	56
4.4.3	B-spline Global Interpolation	56
4.4.4	B-spline Global Approximation	57
4.4.5	Surface Fitting Examples	58
4.4.6	Modification in the Number of Design Parameters	63
4.4.6.1	Knot Insertion	63
4.4.6.2	Knot Removal	65
4.5	Final Remarks	66

5	Stability Analysis	69
5.1	Introduction	69
5.2	Non-Linear Stability Analysis	71
5.2.1	Following the History Path, Incremental-Iterative Methods	72
5.2.1.1	Continuation Methods, Incremental Analysis	73
5.2.1.2	Corrective Phase, Iterative Methods	75
5.2.1.3	Solution Strategies	77
5.2.1.4	Tangent Stiffness Matrix	78
5.2.2	Follower Forces	79
5.2.3	Stability Analysis of Design-Concepts	80
5.2.3.1	Evolution of Shape	81
5.3	Linearized pre-buckling	86
5.3.1	Examples	88
5.3.1.1	One-Arch Model	88
5.3.1.2	Linearized Pre-buckling v/s Non-linear Estimations	90
5.4	Imperfections and their Influences in the Structural Behavior	90
5.4.1	Imperfection Analysis of Concept D2	93
6	Sensitivity Analysis of Discrete Systems	95
6.1	Introduction	95
6.1.1	Optimization Strategies	96
6.1.2	Variable Linking	98
6.2	Finite differences Approximation	99
6.3	Analytical Sensitivity Analysis of Discrete Systems	99
6.3.1	Direct Method	100
6.3.2	Adjoint Method	100
6.4	Semi-Analytical Sensitivity Analysis of Discrete Systems	102
6.5	Objective and Constraints	103
6.5.1	Stress Constraint	103
6.5.2	Buckling Constraint	104
6.6	Sensitivities of Free Form Surfaces	105
6.7	Test Example for Numerical Sensitivities	106

7 Applications	109
7.1 General Parameters for Numerical Examples	109
7.2 Form Finding and Geometrical Model	110
7.2.1 Generation of Geometrical Models - Surface fitting	111
7.2.2 Modification in the Number of Geometrical Coefficients	111
7.3 Optimization and Geometrically Non-Linear Verification	113
7.3.1 Variable Linking in Shape Optimization	114
7.3.2 Variable Linking in Sizing Optimization	115
7.3.3 FE-Discretization and Geometrical Restriction	116
7.3.4 Results	118
7.3.4.1 Shape Optimizaiton Followed by Sizing Optimization	118
7.3.4.2 Simultaneous Shape and Sizing Optimization	127
7.3.5 Final Remarks	132
8 Conclusions and Outlook	135
Bibliography	137

List of Figures

1.1	Data Flow.	3
1.2	Bulkhead location. Source [EAD].	4
1.3	Bulkhead and surroundings. Source [EAD], [Spe05].	4
1.4	Current design. Source [EAD].	5
1.5	Results of topology study. Source [Hör04a].	6
1.6	Topological interpretation and soap-film model.	7
1.7	Bulkhead and adjacent components. Source [Her05].	8
1.8	First concepts. Source [Her05].	9
1.9	Arch concepts. Minimal surfaces.	10
1.10	Multidirectional reinforcement. Source [Spe05].	11
2.1	Motion of a Section of Surface	13
3.1	In-plane stress. Source [Wüc07].	28
3.2	Form finding on extended concept.	31
3.3	Arch concepts. Minimal surfaces, equilibrium configuration.	37
3.4	Concept C. Variation of minimal surfaces.	38
4.1	Parametrical representation of a surface.	41
4.2	Control points \mathbf{P}_i of surface $\mathbf{S}(u, v)$	42
4.3	B-spline basis functions $N_{i,p}(u)$ of polynomial degree $p = 0, 1, 2$ and 3	45
4.4	Basis functions of polynomial degree 2, $\mathbf{U} = \{0, 0, 0, 0.1, 0.3, 0.5, 1, 1, 1\}$	46
4.5	Decreasing continuity by increasing knot multiplicity.	48
4.6	Rendered surface for unaltered knot vector	48
4.7	Basis functions of polynomial degree 2, $\mathbf{U} = \{0, 0, 0, 0.1, 0.3, 0.5, 0.5, 1, 1, 1\}$	49
4.8	Modification in shape by modification of weights.	51

4.9	Data projection on base surface.	55
4.10	FE-mesh of a pressurized bulkhead, 3148 nodes. Units in [mm].	59
4.11	Base surfaces to approximate FE-mesh of figure 4.10. Units in [mm].	59
4.12	Approximated surfaces of example in fig. 4.10. Units in [mm].	60
4.13	Free FE-mesh of 2309 nodes. Units in [mm].	61
4.14	Base surface (4x22 CP) to approximate FE-mesh of figure 4.13. Units in [mm].	61
4.15	Approximated surfaces of example in fig. 4.13 (base 4x22 CP). Units in [mm].	62
4.16	Girded meshes. Parametric domain divided into 20x70 equal spaces.	62
4.17	Knot insertion and removal. Compare with example shown in fig. 4.5(a) . . .	66
5.1	Buckling modes. Load-deflection response diagrams.	70
5.2	Stability analysis of concept A to D.	82
5.3	Stability analysis of Concepts A. Displacement field.	82
5.4	Stability analysis of Concepts B & C. Displacement field.	83
5.5	Comparison between load and displacement control strategies, Concept D2. .	83
5.6	Stability analysis of Concepts D. Displacement field.	84
5.7	Maximum principal stresses, Concept D.	84
5.8	Maximum principal stresses, Concept D2.	85
5.9	Maximum principal stresses, Concept D2, linear kinematics.	85
5.10	Geometric study of arches' radius. Geometry	89
5.11	Extension of Concept C to Concept D. Source [Hör08].	90
5.12	Linearized pre-buckling v/s non-linear analysis. Geometry 1. Source [Hör08].	91
5.13	Linearized pre-buckling v/s non-linear analysis. Geometry 2. Source [Hör08].	91
5.14	Imperfection analysis of Concept D2.	94
6.1	Optimization strategies. Source [Dao05].	97
6.2	Affected region by modifying a design variable y_l	106
6.3	Regions of influence and control point network (20x5).	107
6.4	Sensitivity approximations of structural responses w.r.t. opt. variables.	108
7.1	Concept D2. Equilibrium shape.	110

7.2	Non-linear analysis concept D2. Initial design.	110
7.3	Approximated surfaces, degree 2x2. Base surface of 20x5 CP. Approx. errors.	112
7.4	Approximated surfaces, degree 2x2. Base surface of 20x7 CP. Errors.	113
7.5	Knot insertion. Comparison between errors.	114
7.6	Knot removal. Comparison between errors.	114
7.7	Variable linking and through CP affected regions. Surface of 20x7 CP.	115
7.8	Distribution of design variables for sizing optimization.	116
7.9	Initial finite element mesh for optimization.	116
7.10	Landing-gear conflict.	117
7.11	First modification of CP.	117
7.12	Control point modification. Shape optimization - Base surface.	119
7.13	Final configuration. Shape optimization - Base surface.	120
7.14	Non-linear results. Shape optimization - Base surface.	120
7.15	Final analysis. sizing (after shape) optimization - Base surface.	122
7.16	Control point modification. Shape optimization - Approximated surface.	123
7.17	Final configuration. Shape optimization - Approximated surface.	124
7.18	Non-linear results. Shape optimization - Approximated surface.	124
7.19	Final analysis. sizing (after shape) optimization - Approximated surface.	126
7.20	Control point modification. Shape & sizing optimization - Base surface.	127
7.21	Final configuration. Shape & sizing optimization - Base surface.	127
7.22	Non-linear results. Shape & sizing optimization - Base surface.	128
7.23	Control point modification. Shape & sizing opt. - Approximated surface.	129
7.24	Final configuration. Shape & sizing optimization - Approximated surface.	129
7.25	Non-linear results. Shape & sizing optimization - Approximated surface.	130
7.26	Thickness distribution for final optima.	131

List of Tables

3.1	Comparison between form finding and structural analysis.	33
5.1	Examples for additional constraint $g(\mathbf{u}, \lambda)$. Source [Wri01].	78
5.2	Material properties and load of stability-examples.	80
5.3	Characteristics of shape concepts.	86
5.4	One arch model. Results.	89
5.5	Imperfections of Concept D2. Knock-down factors.	93
7.1	General parameters for applications	109

Chapter 1

Introduction

Engineering design has always involved great amount of time and human resources towards a satisfactory final concept that has to fulfill certain conditions depending on some functionality restrictions. The experience of the designer, the appropriate know-how together with abilities and talent have been the most important prerequisites for the development of adequate configurations subjected to gradual modifications which are translated into progressive improvement.

Nowadays, the field of optimization and more specifically structural optimization allows solution of problems involving complex formulation of mathematical restrictions that have to be satisfied. Structural analysis, design sensitivity analysis and mathematical optimization are combined together in order to identify new feasible configurations which do not need to be previously conceived in the mind of the designer. Experience and ability is now used in the conception and formulation of the problem, which involves for instance the selection of restrictions and suitable algorithms that should be incorporated in order to steer the quality of the final result. In this way, an important amount of time can be saved and consequently design costs are reduced. At the same time, the finite element method is one of the most powerful approaches used to discretize continuous systems, so that the problem under study is formulated in such a way that can be solved with the help of mathematical programming. Increment in computer capabilities over the years plays another important role in the improvement of computational speed and therefore in the inclusion of more sophisticated algorithms to handle more complex problems.

The presented work is part of the collaboration between the Chair of Structural Analysis der Technischen Universität München, and the departments of Structural Concepts and Optimization and Special Analysis, EADS Deutschland, towards optimal design of pressurized light-weight shell structures, aiming cost reduction in terms of weight and manufacturing. One of the first outcomes of this collaboration are found in the Diploma thesis completed by Martin Herrenbrück [Her05] and internal reports written by Herbert Hörnlein [Hör04a], [Hör05].

1.1 Motivation and Objectives

The main objective of this work is to generate a process chain for the design of pressurized thin-walled shells to be constructed using fiber-reinforced composites as components of aircraft structures. The whole design process is divided into several steps. The first one is based on the form finding method, where the geometry can be subdivided into surfaces of minimal area, or variations of them. Afterwards, shape optimization is used to minimize structural weight, where additional restrictions and real boundary conditions are considered.

This chain process is based on two finite element software: CARAT, developed at the chair of structural analysis (Lehrstuhl für Statik der Technische universität München), and LAGRANGE, developed at the department of Optimization and Special Analysis, EADS Deutschland GmbH. Within the scope of this work, The first one will deal with form finding calculations and geometrical non-linear analysis, and the second one will take care of the shape optimal design and related mathematical algorithms. Theses software are briefly described in section 1.2.1.

The process chain involves the use of geometrically nonlinear analysis for the selection of a feasible configuration in order to set it as starting design for a subsequent shape optimization, as well as a tool for verifying the performance of the optimum. Geometrical nonlinear analysis plays a very important role in the design of pressurized thin-walled shell structures, which undergo large displacements under pressure loading and therefore become susceptible to generate unstable configurations.

Another important aspect under consideration is the generation of a suitable geometrical model for shape optimal design. The continuous geometry should be represented using a free from surface whose shape can be steered by the modification of discrete geometrical coefficients. The generation of the geometrical model involves a new geometrical parameterization which differs from standard isoparametrical concepts of finite elements, used during form finding. For this, surface fitting techniques are to be employed, where the concept of design elements arises through CAD representation.

Manufacturing considerations regarding Drapeability (for instance, geometrical restrictions of minimal radii in the design) and generation of cutting patterns for the layout of fabrics in the context of fiber-reinforced material, was left outside the scope of this work.

The following section shows a flow diagram of the design process, and provides a short explanation for each main stage. A detailed insight into each design step is given in the following chapters of this documentation.

1.1.1 Design Process

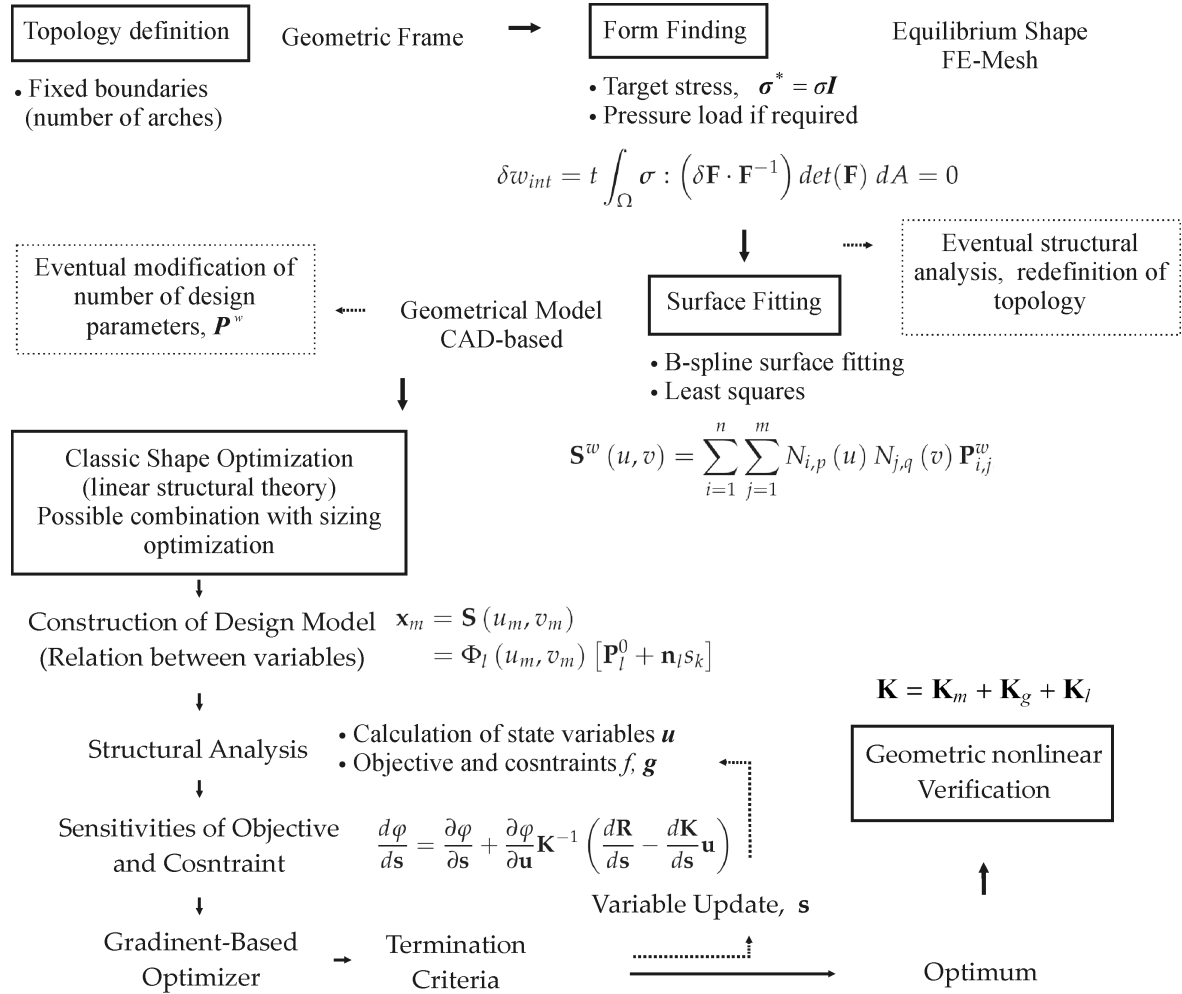


Figure 1.1: Data Flow.

Figure 1.1 contains a diagram with all steps which constitute the design process of pressurized thin-walled shells. It begins with the definition of the topology by setting the number of structural arches which set the boundary of the subsections whose geometry is defined by means of form finding. At this point, the structural shape is driven by the quality and quantity of fictitious applied loading. After a feasible design is found by evaluating the carrying capacity of the shell by means of geometrically non-linear simulations, the geometrical model needed for shape optimization is obtained after fitting a B-spline surface to the nodal coordinates of the equilibrium shape. The geometrical coefficients of the geometrical model are then linked to optimization variables according to the requisites of the analysed example and specifications of the designer. The design model for optimization is then defined. The optimization formulation is completed after defining the restrictions for the feasible domain together with the main objective function to be minimized. Values and gradients of objective and constraints are given to the gradient-based optimizer with the help of structural and sensitivity analyses, in order to compute the next point within the feasible domain towards optimal design. The optimum is found after certain termina-

tion criteria are met. Finally, the performance of the optimal design is checked by running another geometrically nonlinear analysis (large deformations and small strains) on the optimal configuration. Furthermore, modifications to the design process could be enforced at several points of the optimization work flow in order to improve one or more attributes of the structure.

One structural component was selected from a civil passenger aircraft as example for the evaluation and analysis of the different tools and mathematical algorithms that build every stage of the design process. This component divides the compartment where the landing gear is stored during flying time and the cargo area. Figure 1.2 shows the position of the bulkhead. Figure 1.3 shows one of the shape concepts for this structure including surrounding components.



Figure 1.2: Bulkhead location. Source [EAD].

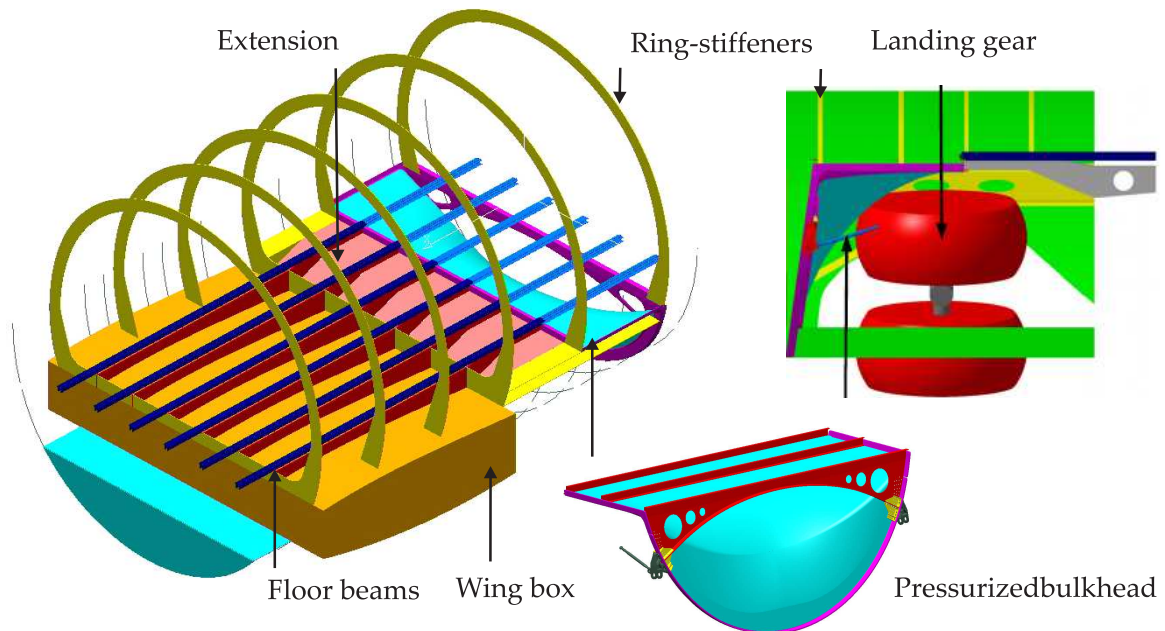


Figure 1.3: Bulkhead and surroundings. Source [EAD], [Spe05].

1.2 State of the Art

Figure 1.4 shows the current design of the previously described bulkhead. It consists basically of two stiffened metallic plates, a horizontal and a vertical one, which carry pressure loading mainly by means of bending stresses. The new concept to be constructed using carbon fiber reinforced composites consists of a single skin that is stiffened by doubly-curved surfaces (figures 1.9 and 1.8) where additional stiffener profiles are no longer needed. Applied loading is now controlled by a higher amount of membrane stresses, leading to material saving, which is also related to manufacturing costs.

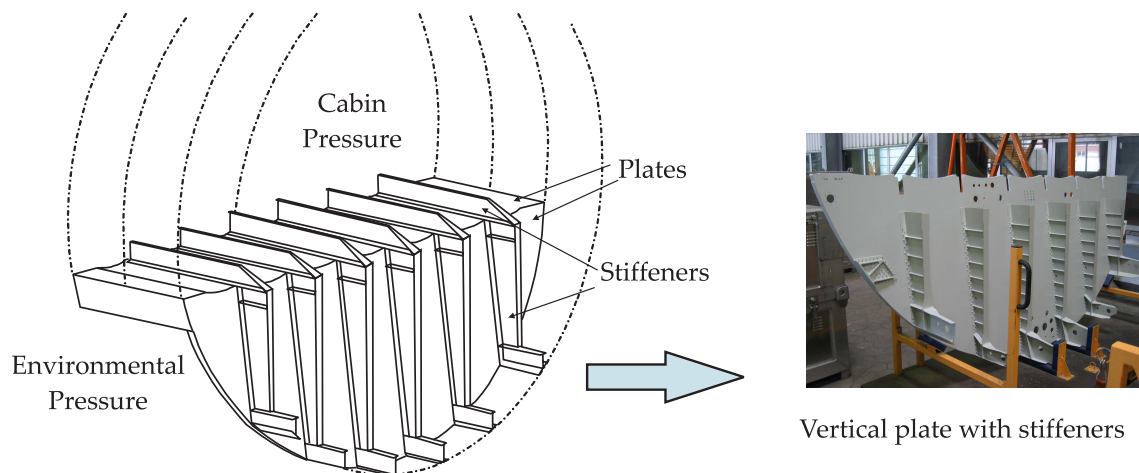


Figure 1.4: Current design. Source [EAD].

1.2.1 FE-Software at Hand

Two finite element software were used along this work: a) CARAT (see reference [BKS94]), which was created at the chair of Structural Analysis, in the University of Stuttgart, and it is also being currently developed at the chair of Structural Analysis at the Technical University of Munich; it is used, in the scope of this work, in form finding calculations and nonlinear simulations; b) LAGRANGE (see reference [Hör04b]), which is being developed at the department of optimization in EADS Deutschland GmbH (Manching, Germany), is used to find the optimal configuration by means of shape optimization.

The software CARAT contains a multi-purpose general rotation free element designed for geometrically nonlinear analysis that can be used to model membrane and shell structures [LWB07]. Membrane strains are calculated using isoparametric displacement elements. Bending stiffness can be optionally added where the curvature of the elements is calculated based on the displacements of discrete nodal directors. The bending component uses Kirchhoff theory, avoiding some common locking phenomena associated to Reissner-Mindling bending theory.

The second shell element used in nonlinear analysis (for the sake of comparison) belongs to the Reissner-element group, meaning that the formulation also includes shear deformation. It uses six degrees of freedom per node, namely three nodal displacement of the midplane and three displacements associated to a representative vector. Membrane and shear locking are controlled by using the Enhanced Assumed Strain (EAS) and the Assumed Natural Strain or Discrete Strain Gap (ANS or DSG) methods respectively (see for instance [Kos04]).

The shell finite element used for optimization in LAGRANGE is a simplification to curved shells as a combination of plate bending element stiffness and membrane element stiffness. Thus degrees of freedom of both type of elements do not couple. Shear locking is controlled by means of reduced integration. An additional shell element for optimization is currently being implemented which is similar to the previously described Reissner-element used in CARAT.

1.2.2 Topological Study

A topology optimization study over a defined region of the aircraft that includes the mentioned bulkhead and adjacent components was performed. The aim of the study was to localize the different stiffening components resulting from the optimal distribution of material [Hör04a]. The topology optimization was performed in two steps using the software OptiStruct (Altair, Engineering, Inc.). First, three dimensional elements were used over the whole available space, so that the general structural configuration could be identified (see figure 1.5). Afterwards, shell elements were used over two-dimensional sub-regions in order to define the particular material setup of adjacent components (see figure 1.7). The objective function was the structural compliance,

$$f = \frac{1}{2} \int_{\Omega} \sigma : \epsilon \, d\Omega, \quad (1.1)$$

subjected to volumetric restriction (details of the topological study are found in [Hör04a]).

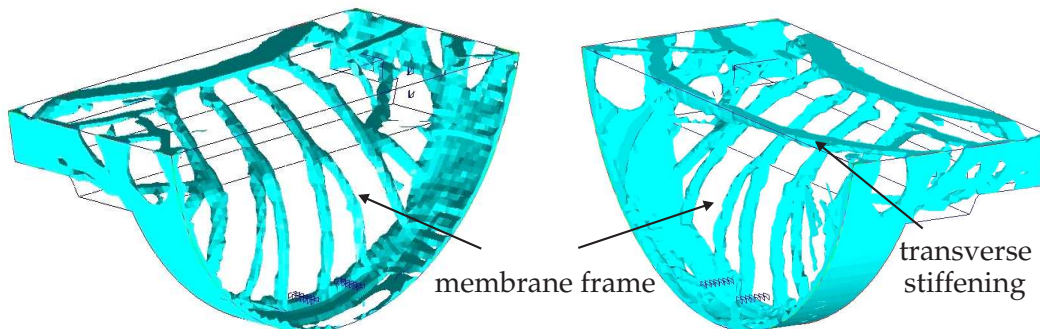


Figure 1.5: Results of topology study. Source [Hör04a].

Figure 1.5 shows two different results as a consequence of considering two different ways for the application of inner pressure due to software restrictions in representing follower forces (see section 5.2.2). Both show more or less the same configuration except for the transverse stiffening, which was translated into an additional component (Spantbrücke) within the second topological optimization step (component c in figure 1.7). Within the stiffening perimeter, the frame of the future bulkhead (membrane frame) can be distinguished. The final interpretation of the results, shown in figure 1.6(a), motivates the search for a doubly-curved thin-walled structure, which would supply an own stabilizing effect when loaded by inner pressure due to generation of tensile (blue color) and compressive (red color) stress trajectories as a response to the applied loads.

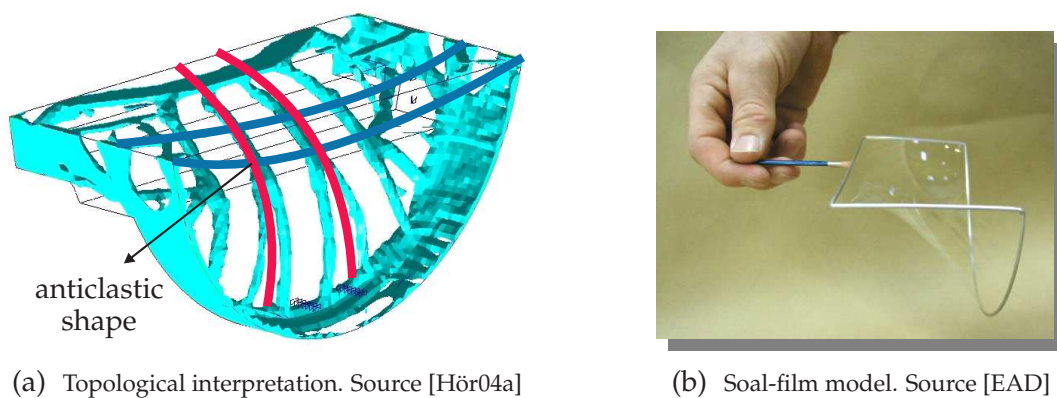


Figure 1.6: Topological interpretation and soap-film model.

Figure 1.7 shows the first layout of the bulkhead, together with additional stiffening components as a result of the topological study. This first bulkhead-design was constructed from an experimental model where a minimal surface was obtained by using soap-film (figure 1.6(b)). The minimal surface among the given boundary provides the required anticlastic shape (see figure 1.6(a)). Details about design of adjacent structures are found in [Her05].

1.2.3 Initial Concepts

In reference [Her05], Martin Herrenück analyses the performance of minimal surfaces and variations of it with respect to stability, strength and geometric evaluations. Variations of minimal surfaces were obtained by modifying the stress field and by adding cable elements as boundary conditions for the form finding computation [Her05]. Modifications to the physical boundary were also included in the analyses (see figure 1.8). One of the problems detected during the study was the flatness of minimal surfaces given the existing boundary (low (high) curvatures along boundaries produces also low (high) curvatures in the resulting minimal surface; see chapter 3). This phenomenon produces excessive displacements when the structure is subjected to real pressure loading, which is finally translated into a

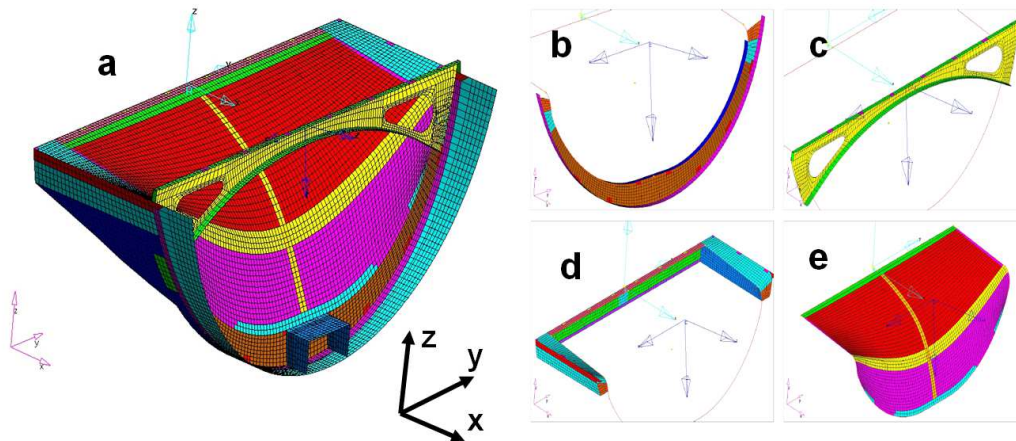


Figure 1.7: Bulkhead and adjacent components. Source [Her05].

higher susceptibility to stability problems.

Results obtained after previously described topological studies, led to a new concept in which several compression arches are now included in the geometrical configuration as shown in figure 1.5. In this way, the total area covered by the first models is subdivided into smaller domains over which minimal surfaces and variations of them are computed. As it could be expected, stability problems are transferred now to the regions of higher compression, represented by the arches between minimal surfaces. Another direct consequence is that the landing gear bay, the space below the compression arches, becomes larger providing also a higher flexibility in geometrical design [Hör05]. The two-arches configuration presented in the study conducted by Martin Herrenbrück (see figure 1.8), was taken as starting point for the present work.

Low critical load factors obtained with the two-arch concept (figure 1.9(a)) motivated the following geometrical improvements: additional stiffeners along the arches, a higher number of arches (figure 1.9(b)) and boundary modifications (figure 1.9(c)) with the aim of improving stability performance. Because of the success of some of these variations, the region covered by the bulkhead could be even extended. Some adjacent components are now integrated into a bigger structure (see figure 1.9(d)). Since the new concept has to be connected to six floor beams (see figure 1.3), a ribbing geometrical pattern consisting of six compression arches was selected as lay out for further improvement [Hör04a].

1.2.4 Loading and support conditions

Among several load cases, inner pressure was the most important one in the generation of solution configurations regarding topological studies [Hör04a]. Therefore, this single load case was selected to be used for the subsequent analyses in order to simplify calculations.

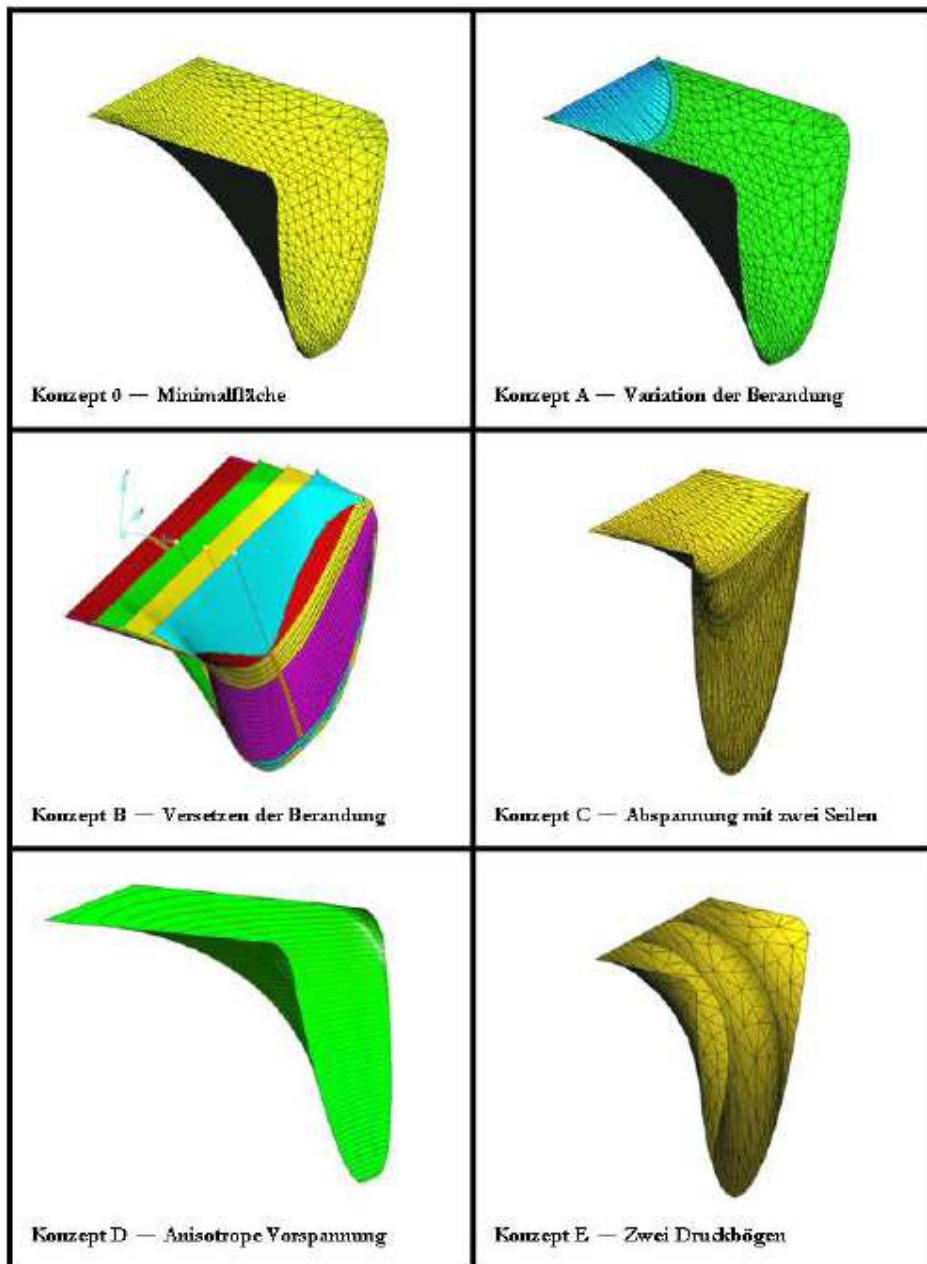


Figure 1.8: First concepts. Source [Her05].

Inner pressure is the resulting pressure difference between the interior of the aircraft and the external environment, which is positive inside of the aircraft. The load case outer pressure (negative inside of the aircraft) was also used to check final designs for security reasons.

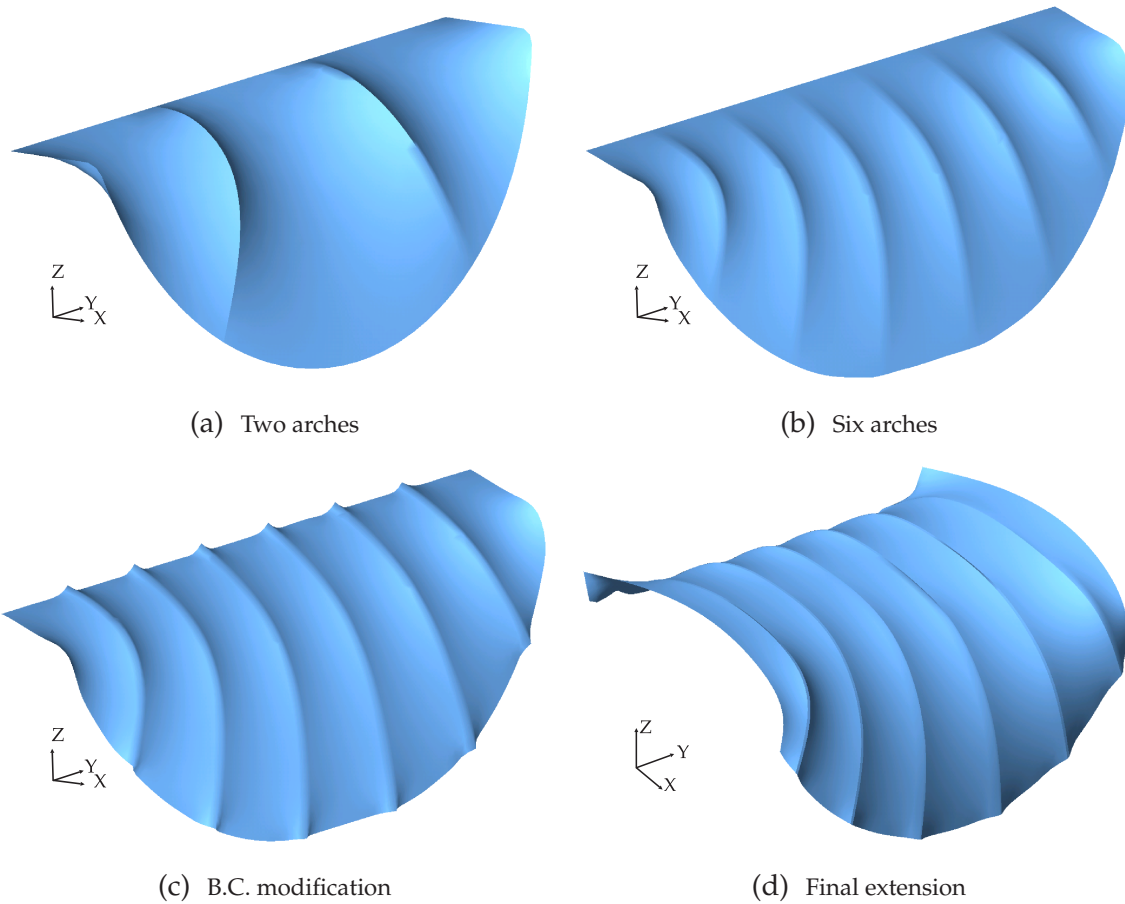


Figure 1.9: Arch concepts. Minimal surfaces.

The value for inner and outer pressure load cases was set to $1.2\text{bar} = 0.12\text{N}/\text{mm}^2$, and $0.6\text{bar} = 0.06\text{N}/\text{mm}^2$ respectively.

1.2.5 Material

Fiber-reinforced materials are being increasingly incorporated in the aerospace and automotive industry due to its inherent advantages. At presence of loads that maintain a certain direction of application, the fibers of a composite can be re-directed in order to optimally withstand them by saving weight at the same time. Reinforced materials give advantages compared to metallic constructions regarding corrosion and fatigue, although their use is still connected to high manufacturing costs [Kör02], due to the high amount of hand-work required for their construction. Delamination is another implicit problem found in the fabrication of fiber-reinforced materials. It can be detected using costly and elaborated procedures of control. Nevertheless, they possess a higher weight saving property compared to metals.

Prepeg, a ready to use reinforced material, has been the usual choice for serial production of structural components. It consists on roles of pre-impregnated fiber reinforcement, where the matrix is already included but its final stiffness is not yet reached. This kind of reinforcement gain its final stiffness after the desired shape is obtained. As an alternative to prepegs, there is also the technique of Resin Transfer Moulding (RTM), which is available since more that 40 years. Several plies of reinforcement are placed on top of each other and kept together with the help of temperature. The injection of the matrix, which bonds layers together and finally transfers the loading to the reinforcement, takes place after draping of the plies. This technique allows a higher flexibility in shape moulding, specially for not developable doubly curved surfaces. Drapability becomes more elaborated by increasing the complexity of the geometry. Another advantage of this second technique is that several plies can be used to model the desired shape before infiltration, which is translated in a reduction of time and manufacturing costs [Kör02]. Figure 1.10 taken from reference [Spe05] shows a multidirectional fiber reinforcement including four fiber directions. Reference [Hör94] presents a detailed description of fabric construction for reinforcement and explanations of different techniques for the production of fiber-reinforced material. Reference [Spe05] includes drapability of multidirectional fiber reinforcement applied to a light-weight shell structure.

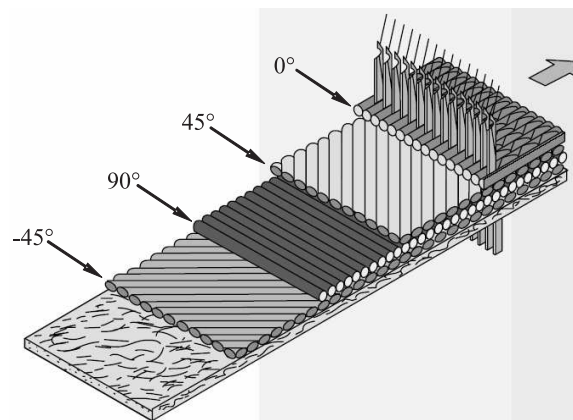


Figure 1.10: Multidirectional reinforcement. Source [Spe05].

Even though the analysed structures throughout this work are designed to be built using carbon composites, it is assumed for the sake of simplicity, that the material consists of several layers of fibers oriented along many different directions, so that its behavior can be considered as quasi-isotropic. Therefore, a linear elastic homogeneous and isotropic material is taken as material model for the different subsequent analyses (see section 2.4).

1.3 Contents of this report

Chapter 2 contains theoretical background of differential geometry of surfaces and nonlinear mechanics towards FE-formulation of membranes and shells.

Chapter 3 describes the basics of the form finding method, which defines the shape of surfaces enclosed by the structural frame, the topological basis of the corresponding design concepts. Examples are given for some of the concepts shown in figure 1.9, including isotropic and anisotropic stress field as boundary condition in form finding analysis as well as normal pressure as additional loading.

Chapter 4 shows selection and construction of the geometrical model used later in shape optimization. It gives a brief overview about non-rational and rational B-splines as the type of free form surface selected for design. It Also contains some examples regarding global surface fitting performed over a set of nodal coordinates selected as scattered data.

Chapter 5 gives some background about stability analysis of structures by presenting common methodologies for tracing load-displacement histories in geometrically non-linear modeling and estimation of critical load by means of direct methods when the stiffness of the system is considered to be independent of displacements. Stability analyses are performed over some design-concepts. Imperfections are used with one of the selected examples in order to evaluate their influence in the structural behavior.

Chapter 6 presents some aspects of shape optimization theory focused basically on discrete sensitivity analysis and variable linking regarding selected structural responses of the geometrical models.

Chapter 7 review all stages in the process chain concerning design of pressurized lightweight structures by taking as example the topological configuration of the final extended concept.

Finally, Chapter 8 contains comments and conclusions derived from the presented work.

Chapter 2

Review of Continuum Mechanics and FE-Formulation

This chapter includes the basic mechanical theory that will be referred to in the next chapters. It contains the necessary formulations to solve quasi-static type of problems included along this report. The chapter begins with fundamental assumptions of continuum mechanics followed by equilibrium equations discretized by means of finite elements. For a closer insight into this topics, refer to related literature. See for instance [Hol00], [KW91], [Wri01], [Wei00] and [BLM00].

2.1 Differential Geometry

The present section is intended to characterize the position of a particle within a body in space, and how its position evolve after a certain period of time.

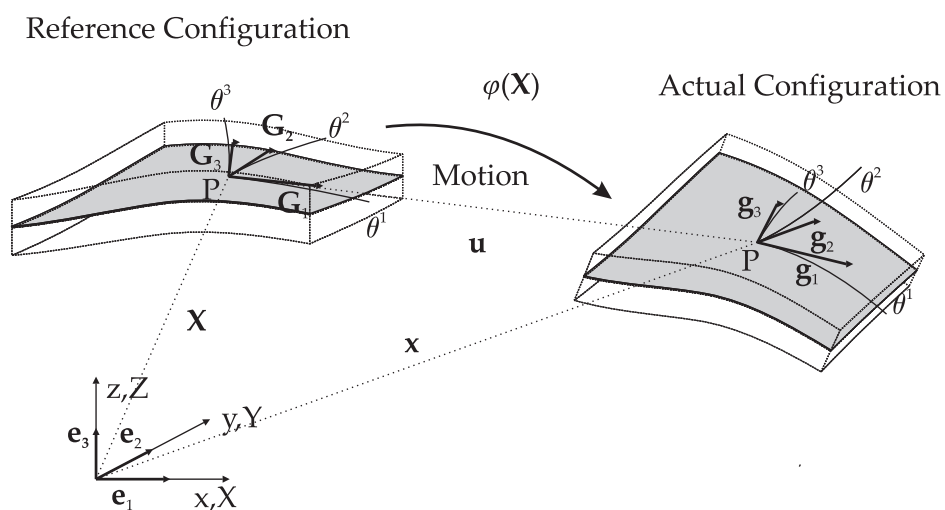


Figure 2.1: Motion of a Section of Surface

The position X of a particle P of a solid before motion has taken place is known as *initial*

configuration (or reference configuration), whereas *current configuration* (also called actual configuration) corresponds to the position \mathbf{x} of the particle after motion $\varphi(X)$. This situation is shown in Figure 2.1 in a three dimensional space defined by the Cartesian base vectors \mathbf{e}_i . The difference of time Δt between undeformed and deformed states, can be also interpreted as a modification in the configuration of the solid after certain boundary conditions have been changed or applied (increments of a certain control parameter like for instance load) as it is the case for quasi-static deformation, so that sequences of several configurations can be established. This type of problems is also known as time-independent formulation which neglects inertia effects. The time is now denominated as pseudo time.

The position vectors of any particle P is given by the following equations,

$$\mathbf{X} = X_i \mathbf{e}_i \quad (2.1)$$

$$\mathbf{x} = x_i \mathbf{e}_i \quad (2.2)$$

The components X_i are the referential coordinates of point P , and the components x_i the current coordinates of point P , both using the same Cartesian basis \mathbf{e}_i .

There is another way to define the position of a point in a continuum, namely using a curvilinear three dimensional coordinate system that is contained within the body. Their components θ^i remain invariant during motion. They are defined with respect to the covariant basis \mathbf{G}_i at the initial configuration, and with respect to the second set of covariant basis \mathbf{g}_i at the current configuration. Thus, the components of a position vector in Cartesian components can be also written as a function of the curvilinear components ($\mathbf{X}(\theta^i)$, $\mathbf{x}(\theta^i)$).

Using the previous concepts and relations, the *covariant* base vectors with respect to the initial and current configurations are computed as the partial derivative of the components of the position vector with respect to the body components θ^i ,

$$\mathbf{G}_i = \frac{\partial \mathbf{X}}{\partial \theta^i}; \quad \mathbf{g}_i = \frac{\partial \mathbf{x}}{\partial \theta^i} \quad (2.3)$$

The inverse operation defines its reciprocal basis called *contravariant* base vectors,

$$\mathbf{G}^i = \frac{\partial \theta^i}{\partial \mathbf{X}}; \quad \mathbf{g}^i = \frac{\partial \theta^i}{\partial \mathbf{x}} \quad (2.4)$$

The dot product between covariant and contravariant base vectors gives as a result the metric coefficients (2.5), which are used in section 2.2 to measure the deformation of a solid.

$$G_{ij} = \mathbf{G}_i \cdot \mathbf{G}_j; \quad G^{ij} = \mathbf{G}^i \cdot \mathbf{G}^j; \quad g_{ij} = \mathbf{g}_i \cdot \mathbf{g}_j; \quad g^{ij} = \mathbf{g}^i \cdot \mathbf{g}^j \quad (2.5)$$

In general, as shown in this section, quantities expressed in terms of initial coordinates will usually be written in small letters and quantities expressed in terms of current coordinates using capital letters.

For surfaces, the position vector of a selected point P is denoted by

$$\mathbf{X}(\theta^1, \theta^1, 0) = \mathbf{X}|_{\theta^3=0} = \mathbf{R}(\theta^1, \theta^2); \quad \mathbf{x}(\theta^1, \theta^1, 0) = \mathbf{x}|_{\theta^3=0} = \mathbf{r}(\theta^1, \theta^2) \quad (2.6)$$

with respect to undeformed and deformed configurations respectively. The third curvilinear component is set equal to zero.

For shells, the location of a point along the midsurface is determined using equation (2.6). The third coordinate θ^3 is used to define regions of the shell away from the midsurface and it is defined to be in the interval

$$\theta^3 \in \left[-\frac{t(\theta^1, \theta^2)}{2}, \frac{t(\theta^1, \theta^2)}{2} \right] \quad (2.7)$$

where $t(\theta^1, \theta^2)$ is the thickness of the shell. The usual definition for the direction of θ^3 is to compute the normal vector to the midsurface, which is also called director vector (see also equation 4.1). With respect to the undeformed configuration, the direction for θ^3 is computed as

$$\mathbf{g}_3 = \mathbf{n} = \frac{\mathbf{g}_1 \times \mathbf{g}_2}{\|\mathbf{g}_1 \times \mathbf{g}_2\|} \quad (2.8)$$

2.2 Kinematics

The displacement \mathbf{u} of a point P in a solid is calculated as the difference between the position vectors as,

$$\mathbf{u} = \mathbf{x}(\theta^i) - \mathbf{X}(\theta^i) \quad (2.9)$$

Using the previous relation, equation (2.3) can be written as

$$\mathbf{G}_i = \frac{\partial \mathbf{X}}{\partial \theta^i} = \mathbf{g}_i - \mathbf{u}_{,i}; \quad \mathbf{g}_i = \frac{\partial \mathbf{x}}{\partial \theta^i} = \mathbf{u}_{,i} + \mathbf{G}_i \quad (2.10)$$

In order to measure the deformation of a solid is necessary to know the new distribution of its particles after deformation. The redistribution of particles (rotation and stretching) is measured by the *deformation gradient*, \mathbf{F} . The deformation gradient is a tensor of second order that relates material and spatial configurations by means of co- and contravariant basis vectors and it is used to transform quantities between undeformed and deformed configurations. \mathbf{F} and its transposed are given by,

$$\mathbf{F} = \frac{\partial \mathbf{x}}{\partial \mathbf{X}} = \frac{\partial \mathbf{x}}{\partial \theta^i} \otimes \frac{\partial \theta^i}{\partial \mathbf{X}} = \mathbf{g}_i \otimes \mathbf{G}^i; \quad \mathbf{F}^T = \left(\frac{\partial \mathbf{x}}{\partial \mathbf{X}} \right)^T = \mathbf{G}^i \otimes \mathbf{g}_i. \quad (2.11)$$

And the inverse tensors \mathbf{F}^{-1} and \mathbf{F}^{-T} by

$$\mathbf{F}^{-1} = \frac{\partial \mathbf{X}}{\partial \mathbf{x}} = \mathbf{G}_i \otimes \mathbf{g}^i; \quad \mathbf{F}^{-T} = \mathbf{g}^i \otimes \mathbf{G}_i. \quad (2.12)$$

In order to transform the components of a tensor from undeformed to deformed configuration (or vice versa) the operation called push-forward (pull-back respectively) is addressed, where basis vectors are transformed using the following expressions ([Lin09]). For covariant base vectors,

$$\mathbf{g}_i = \mathbf{F} \mathbf{G}_i, \quad \mathbf{G}_i = \mathbf{F}^{-1} \mathbf{g}_i; \quad (2.13)$$

and for contravariant base vectors,

$$\mathbf{g}^i = \mathbf{F}^{-T} \mathbf{G}^i, \quad \mathbf{G}^i = \mathbf{F}^T \mathbf{g}^i. \quad (2.14)$$

This expressions are used later to transform the components of the strain tensors.

2.2.1 Strain Measurements

The second order strain measure that will be used along this report is the *Green-Lagrange* strain tensor \mathbf{E} . This strain tensor given in material coordinates, is used frequently in geometrically non-linear formulation assuming large deformations and small strains.

The advantage of using tensor quantities based on the reference configuration in non-linear formulations is that the base vectors \mathbf{G}_i and \mathbf{G}^i (see Figure 2.1) remain unchanged during deformation and are not subjected to derivation in case the formulation has to be perturbed or linearized with respect to the independent parameters (see section 2.5.3).

The Green-Lagrange strain tensor is expressed as,

$$\mathbf{E} = \frac{1}{2}(\mathbf{F}^T \mathbf{F} - \mathbf{I}). \quad (2.15)$$

Using equations (2.11) it can be written in the form,

$$\mathbf{E} = \frac{1}{2} (\mathbf{g}_i \cdot \mathbf{g}_j - \mathbf{G}_i \cdot \mathbf{G}_j) \mathbf{G}^i \otimes \mathbf{G}^j. \quad (2.16)$$

Making use of the push-forward operation for covariant components [Wei00], the coefficients of the Green-Lagrange strain tensor E_{ij} , are transformed into the deformed configuration (e_{ij}). The conversion of the contravariant base vectors is done using equations (2.14),

$$\begin{aligned} \mathbf{e} &= \mathbf{F}^{-T} \mathbf{E} \mathbf{F}^{-1} \\ &= \mathbf{F}^{-T} \left[\frac{1}{2} (\mathbf{g}_i \cdot \mathbf{g}_j - \mathbf{G}_i \cdot \mathbf{G}_j) \mathbf{G}^i \otimes \mathbf{G}^j \right] \mathbf{F}^{-1} \\ &= \frac{1}{2} (\mathbf{g}_i \cdot \mathbf{g}_j - \mathbf{G}_i \cdot \mathbf{G}_j) \mathbf{g}^i \otimes \mathbf{g}^j. \end{aligned} \quad (2.17)$$

The strain tensor \mathbf{e} referred to the deformed configuration is called *Almansi* strain tensor.

From equations (2.16) and (2.17) we have

$$E_{ij} = e_{ij}. \quad (2.18)$$

In equations (2.16) and (2.17) the following expression for the identity tensor \mathbf{I} was adopted,

$$\mathbf{I} = (\mathbf{G}_i \cdot \mathbf{G}_j) \mathbf{G}^i \otimes \mathbf{G}^j = G_{ij} \mathbf{G}^i \otimes \mathbf{G}^j. \quad (2.19)$$

In general, the Identity tensor can be expressed in several forms,

$$\mathbf{I} = G_{ij} \mathbf{G}^i \otimes \mathbf{G}^j = G^{ij} \mathbf{G}_i \otimes \mathbf{G}_j = g_{ij} \mathbf{g}^i \otimes \mathbf{g}^j = g^{ij} \mathbf{g}_i \otimes \mathbf{g}_j, \quad (2.20)$$

and the most convenient of them is chosen for the particular case in tensor algebra.

2.3 Stress Measures

The 2nd Piola-Kirchhoff stress tensor \mathbf{S} , which is the energetic conjugated of the Green strain tensor \mathbf{E} , is given by

$$\mathbf{S} = J \mathbf{F}^{-1} \cdot \boldsymbol{\sigma} \cdot \mathbf{F}^{-T}. \quad (2.21)$$

where J is the determinant of the deformation gradient (also called Jacobian determinant) and represents the ratio of volumes between the deformed and undeformed configurations. It is defined as

$$J = \det(\mathbf{F}) = \frac{dv}{dV} \quad (2.22)$$

The second-order tensor $\boldsymbol{\sigma}$ of Equation (2.21) is the Cauchy stress tensor defined with respect to the current configuration, and therefore it is used as the energetic conjugated of the Almansi stress tensor (see section 2.5). It is a symmetric tensor oriented in the direction of the normal to surface vector \mathbf{n} where a traction vector \mathbf{t} is applied. The equation that relates this three quantities is given by

$$\mathbf{t} = \boldsymbol{\sigma} \mathbf{n} \quad (2.23)$$

The 2nd Piola-Kirchhoff stress tensor \mathbf{S} does not have a physical representation in terms of a traction vector compared to the Cauchy stress tensor. Nevertheless, it is often a very useful strain measurement for the constitutive formulation, since its components are related to the reference configuration.

2.4 Constitutive Equations

The constitutive equations, also called material laws, specify the type of material that is used in the mechanical model, so that the stresses in a solid can be computed at any position in terms of the strains. This relations are approximate, since they are based on experimental observation. Nevertheless, they are formulated under certain mechanical conditions [Wei00]. The material model presented in this section is the Saint Venant-Kirchhoff material, used in nonlinear mechanics when large deformations and small strains are assumed. It belongs to the category of perfectly elastic materials, meaning that no internal dissipation is considered, and consequently it is path independent and fully reversible (the stress field is derived from a elastic strain energy potential [BLM00]). The most general formulation is given by

$$\mathbf{S} = \mathbf{C} : \mathbf{E} \quad (2.24)$$

\mathbf{C} is the fourth-order tensor called tangent modulus. Its elements C_{ijkl} , the tangent moduli, are composed of 81 independent constants, as a result of relating the 9 components of the strain tensor with the 9 components of the stress tensor.

In curvilinear coordinates the material tensor \mathbf{C} is expressed as

$$\mathbf{C} = C^{ijkl} \mathbf{G}_i \otimes \mathbf{G}_j \otimes \mathbf{G}_k \otimes \mathbf{G}_l \quad (2.25)$$

Due to symmetrical conditions the tangent modulus has to fulfill in the scope of the finite element formulation, the independent elastic constants are reduced to 21 [Hol00], [BLM00], which is the case for anisotropic material. In case of material symmetry, the number of independent variables can be further reduced. For orthotropic and isotropic materials, the independent constants decrease to only nine and two respectively.

In the last case, when there is no preferred orientation for the material, equation (2.25) is written in terms of two material coefficients, the Young's modulus E and Poisson's ration ν . Using Lamé constants

$$\lambda = \frac{\nu E}{(1 + \nu)(1 - 2\nu)} \quad \text{and} \quad \mu = \frac{E}{2(1 + \nu)} \quad (2.26)$$

the components of the material tensor in (2.25) are computed as [BLM00]

$$C^{ijkl} = \lambda G^{ij} G^{kl} + \mu (G^{ik} G^{jl} + G^{il} G^{jk}) \quad (2.27)$$

In case the mechanical theory is derived for linear elasticity (small deformation), equation (2.24) is known as Hooke's law. When the material is composed of different layers, the above introduce constitutive law is valid for every single layer (see for instance [GHH99]).

2.5 Governing Equations of Motion

2.5.1 Principle of virtual work

The principle of virtual work is usually selected to derive the governing equations of motion previous to finite element discretization. Its application is not only used in structural analysis, but also in other fields of study, for instace: fluid equations, fluid structure interaction and heat conduction. In the area of structural analysis it does not restrict the type of material and dependency of time. Equation (2.28) describes the general formulation of the principle of virtual work, in which inertial forces are neglected. This expression represents the equality between the virtual external work of a body subject to prescribed boundary conditions and the consequently generated virtual internal work when a virtual displacement $\delta \mathbf{u}$ is induced.

$$\begin{aligned}
\delta W(\mathbf{u}) &= \delta W_{int}(\mathbf{u}) - \delta W_{ext}(\mathbf{u}) \\
&= \int_{\Omega_0} \mathbf{S} : \delta \mathbf{E} dV - \int_{\Omega_0} \mathbf{B} \cdot \delta \mathbf{u} dV - \int_{\partial \Omega_0 \sigma} \hat{\mathbf{T}} \cdot \delta \mathbf{u} dS = 0.
\end{aligned} \tag{2.28}$$

The contribution to the internal virtual work is provided by the 2nd Piola-Kirchhoff stress tensor \mathbf{S} and the variation of the Green-Lagrange strain tensor \mathbf{E} . The external virtual work is produced by the body forces \mathbf{B} and the applied traction vector $\hat{\mathbf{T}}$ together with the variation in the displacement field along the complete domain of the system Ω and its boundary $\partial \Omega_\sigma$.

The essential boundary conditions $\hat{\mathbf{u}} = \mathbf{u}$ applied over the displacement domain $\partial \Omega_u$, in order to suppress rigid body movements, are implicitly included in the equilibrium equations. In the previous formulation, initial values for stresses and strains are considered equal to zero, which means that at the initial configuration neither residual stresses nor residual strains are present.

In spatial coordinates, with respect to the deformed configuration, the principle of virtual work is written as:

$$\begin{aligned}
\delta w(\mathbf{u}) &= \delta w_{int}(\mathbf{u}) - \delta w_{ext}(\mathbf{u}) \\
&= \int_{\Omega} \boldsymbol{\sigma} : \delta \mathbf{e} dv - \int_{\Omega} \mathbf{b} \cdot \delta \mathbf{u} dv - \int_{\partial \Omega_\sigma} \hat{\mathbf{t}} \cdot \delta \mathbf{u} ds = 0
\end{aligned} \tag{2.29}$$

where the internal virtual work is done by the Cauchy stress tensor $\boldsymbol{\sigma}$ and the variation of the Euler-Almansi strain tensor \mathbf{e} .

The previous variational principles depend only on the displacement field. Situation that excludes other finite element formulations in which the mechanical problem has to be solved for more than one unknown. This is the case for instance for some formulations which are derived as a solution to locking effects, where stresses and/or strains are considered as unknowns as well [CB03], [Kos04].

2.5.2 Linearization of Equilibrium Equations

Due to the nonlinear formulation of the strain tensor, both sets of equilibrium equations (2.28) and (2.29) are nonlinear equations with respect to the independent variables \mathbf{u} , the displacement field. The linearization of the differential equilibrium equations, allows the solution of the mechanical problem using iterative approaches, where linear system of equations are solved at each iterative step. The most common iterative approach used to solve a set of linear equations after linearization is the Newton-Raphson method which updates the value of the displacement field at each iteration step, until a certain convergence criteria is met.

In order to illustrate the idea of linearization, an arbitrary C^n -continuous function ψ is

considered as example defined in \mathbb{R} , which depends on the variable x . The value of the function for an increment ($\Delta x = x^{n+1} - x^n$) of the dependent variable is computed using its Taylor expansion at point x^n as

$$\psi(x^n + \Delta x) = \psi(x^n) + \frac{\partial \psi(x^n)}{\partial x} \cdot \Delta x + T \quad (2.30)$$

where T represents higher order derivatives of the function and is considered, for the linearization, negligible for small increments Δx .

The linearization of a function at a certain point x^n is then expressed as the evaluation of the function at that point plus the directional derivative of the function evaluated at the considered point in direction Δx [Wri01]. The directional derivative of ψ is also written using the notation $\Delta \psi(x)$, where

$$\Delta \psi(x, \Delta x) = D_{\Delta x} \psi(x) = \frac{d}{d\epsilon} \psi(x + \epsilon \Delta x) |_{\epsilon=0} = \frac{\partial \psi(x^n)}{\partial x} \cdot \Delta x \quad (2.31)$$

The concept of linearization is similar to variation, since it is also based on directional derivatives. For instance the directional derivative of a function $\psi(x)$ is evaluated at any fixed point x in the direction δx ,

$$\delta \psi(x, \delta x) = D_{\delta x} \psi(x) = \frac{d}{d\epsilon} \psi(x + \epsilon \delta x) |_{\epsilon=0} = \frac{\partial \psi(x^n)}{\partial x} \cdot \delta x \quad (2.32)$$

Linearization $\Delta(\bullet)$ and variation $\delta(\bullet)$ are linear operators based on the same rules of differentiation ([Hol00]).

Nonlinear structural problems are usually formulated with respect to the undeformed configuration, where the geometry is already known. Consequently, the related vector spaces remain constant and do not have to be subjected to differentiation. The linearization of the virtual work equations related to the undeformed configuration (equation 2.28) is done with respect to the free parameters \mathbf{u} and using equation (2.30) without considering higher order terms,

$$\begin{aligned} \delta W(\mathbf{u}^{n+1}) &= \delta W(\mathbf{u}^n) + \Delta \delta W(\mathbf{u}^n) = 0 \\ &= \delta W(\mathbf{u}^n) + \frac{\partial [\delta W(\mathbf{u}^n)]}{\partial \mathbf{u}} \cdot \Delta \mathbf{u} = 0, \text{ together with} \end{aligned} \quad (2.33)$$

$$\Delta \mathbf{u} = \mathbf{u}^{n+1} - \mathbf{u}^n \quad (2.34)$$

The linear model $\Delta \delta W(\mathbf{u}^n)$ represents the tangent to the nonlinear system $\delta W(\mathbf{u})$ at the corresponding value \mathbf{u}^n . The requisite for linearization, is that function $\delta W(\mathbf{u})$ and its first derivative $\partial \delta W(\mathbf{u}) / \partial \mathbf{u}$ must exist and be continuous.

In the following linearization of equilibrium equations (2.28), it is considered only the contribution of the internal work. The contribution of the external virtual work (last two terms in equation (2.28)) to the linear approximation $\Delta \delta W(\mathbf{u})$ vanishes when body forces \mathbf{B} and the applied traction vector $\hat{\mathbf{T}}$ do not depend on the parameters \mathbf{u} . In chapters 3 and 5

it is assumed that a special type of traction vector (pressure loading) is dependent on the displacement field \mathbf{u} and therefore its contribution to the linearization process should be taken into account.

The linearization of the internal work $\delta W_{int}(\mathbf{u})$ in the direction of $\Delta \mathbf{u}$ is then computed, by using the chain rule of derivation, as:

$$\begin{aligned}\Delta \delta W_{int}(\mathbf{u}) &= \int_{\Omega_0} \Delta [\mathbf{S}(\mathbf{E}(\mathbf{u})) : \delta \mathbf{E}(\mathbf{u})] dV \\ &= \int_{\Omega_0} [\delta \mathbf{E} : \Delta \mathbf{S} + \mathbf{S} : \Delta \delta \mathbf{E}] dV,\end{aligned}\tag{2.35}$$

and knowing that for a linear material $\Delta \mathbf{S} = \mathbf{C} : \Delta \mathbf{E}$, finally we have

$$\Delta \delta W_{int}(\mathbf{u}) = \int_{\Omega_0} [\delta \mathbf{E} : \mathbf{C} : \Delta \mathbf{E} + \mathbf{S} : \Delta \delta \mathbf{E}] dV.\tag{2.36}$$

The derivation of the linearization of the internal work with respect to the deformed configuration is more complicated and involves derivatives of base vectors since they are also a function of the displacement field $\delta \mathbf{u}$. More details on this topic are found for instance in [Wri01], and [Hol00].

2.5.3 Variation and Linearization of Strain Tensors

Linearization of the Green-Lagrange strain tensor are computed from equation (2.15), using relations (2.31) and equations (2.11).

$$\begin{aligned}\Delta \mathbf{E} &= \frac{1}{2}(\Delta \mathbf{F}^T \mathbf{F} + \mathbf{F}^T \Delta \mathbf{F}) \\ &= \frac{1}{2}(\Delta \mathbf{g}_i \cdot \mathbf{g}_j + \mathbf{g}_i \cdot \Delta \mathbf{g}_j) \mathbf{G}^i \otimes \mathbf{G}^j.\end{aligned}\tag{2.37}$$

The variation of the Green-Lagrange strain tensor is computed using the same concept (see equation 2.32) as:

$$\delta \mathbf{E} = \frac{1}{2}(\delta \mathbf{g}_i \cdot \mathbf{g}_j + \mathbf{g}_i \cdot \delta \mathbf{g}_j) \mathbf{G}^i \otimes \mathbf{G}^j\tag{2.38}$$

Considering that the displacement field $\delta \mathbf{u}$ is independent of the displacements \mathbf{u} , when computing the linearization of the variation of the Green-Lagrange strain tensor $\Delta \delta \mathbf{E}$, the terms containing the variation $\delta \mathbf{u}$ (in this case $\delta \mathbf{F}$), are not affected by the linearization ([Hol00]). This leads to the following expression by using the rules of differentiation,

$$\begin{aligned}\Delta \delta \mathbf{E} &= \Delta \left[\frac{1}{2}(\delta \mathbf{F}^T \mathbf{F} + \mathbf{F}^T \delta \mathbf{F}) \right] \\ &= \frac{1}{2}(\delta \mathbf{F}^T \Delta \mathbf{F} + \Delta \mathbf{F}^T \delta \mathbf{F}) \\ &= \frac{1}{2}(\delta \mathbf{g}_i \cdot \Delta \mathbf{g}_j + \Delta \mathbf{g}_i \cdot \delta \mathbf{g}_j) \mathbf{G}^i \otimes \mathbf{G}^j.\end{aligned}\tag{2.39}$$

Regarding variation and linearization of the Almansi strain tensor \mathbf{e} , the formulation is obtained by first performing the corresponding operation with the Green-Lagrange strain tensor \mathbf{E} and afterwards using the push-forward operation for contravariant base vectors as explained in section 2.2, by using equations (2.14). Thus, we have for the variation of \mathbf{e}

$$\begin{aligned}\delta \mathbf{e} &= \mathbf{F}^{-T} \delta \mathbf{E} \mathbf{F}^{-1} = \frac{1}{2} (\mathbf{F}^{-T} \delta \mathbf{F}^T + \delta \mathbf{F} \mathbf{F}^{-1}) \\ &= \frac{1}{2} (\delta \mathbf{g}_i \cdot \mathbf{g}_j + \mathbf{g}_i \cdot \delta \mathbf{g}_j) \mathbf{g}^i \otimes \mathbf{g}^j,\end{aligned}\quad (2.40)$$

and for its linearization,

$$\begin{aligned}\Delta \delta \mathbf{e} &= \mathbf{F}^{-T} \Delta \delta \mathbf{E} \mathbf{F}^{-1} \\ &= \frac{1}{2} (\delta \mathbf{g}_i \cdot \Delta \mathbf{g}_j + \Delta \mathbf{g}_i \cdot \delta \mathbf{g}_j) \mathbf{g}^i \otimes \mathbf{g}^j.\end{aligned}\quad (2.41)$$

The internal contribution to the virtual work in equation (2.28) is formulated now using equation (2.38) in coefficients as,

$$\delta W_{int}(\mathbf{u}) = \int_{\Omega_0} S^{ij} (\delta \mathbf{g}_i \cdot \mathbf{g}_j) dV, \quad (2.42)$$

and its linearization, equation (2.36), using (2.38) and (2.39), and taken advantages of the symmetry of the stress tensor \mathbf{S} ([ZT05]),

$$\Delta \delta W_{int}(\mathbf{u}) = \int_{\Omega_0} \left[(\mathbf{g}_i \cdot \delta \mathbf{g}_j) C^{ijkl} (\mathbf{g}_k \cdot \Delta \mathbf{g}_l) + (\delta \mathbf{g}_i \cdot \Delta \mathbf{g}_j) S^{ij} \right] dV. \quad (2.43)$$

2.5.4 Finite Element Discretization

The fundamental advantage of using the finite element method is that the complete domain Ω of the continuum is divided into single elements (elemental domain Ω^e), containing similar properties, so that the problem is simplified by formulating it within every element¹. Subsequently, the contribution of each finite element is assembled in a global system by means of common boundaries, the discrete nodal degrees of freedom, in order to solve the final coupled system,

$$\Omega \approx \bigcup_{e=1}^{n_e} \Omega^e. \quad (2.44)$$

Thus, the accuracy of the final solution depends on the degree of approximation selected at element level for: geometry in deformed and undeformed configurations (\mathbf{x} and \mathbf{X} respectively), and the unknown field of the formulation \mathbf{u} .

$$\mathbf{u} \approx \bigcup_{e=1}^{n_e} \mathbf{u}^e; \quad \mathbf{X} \approx \bigcup_{e=1}^{n_e} \mathbf{X}^e; \quad \mathbf{x} \approx \bigcup_{e=1}^{n_e} \mathbf{x}^e \quad (2.45)$$

¹In the general case, the total domain of the problem is divided into sub-domains, where each one of them is then partitioned into finite elements having the same characteristics related to the corresponding sub-domain.

The approximation is done using interpolation functions between nodal values, where the number of nodal values together with the quality of the shape functions are the variables used to approximate the exact solution.

In the scope of this work, only isoparametric elements are employed. They approximate displacement field and geometry field by means of the same shape functions $N(\boldsymbol{\theta})_k$.

$$\mathbf{u}^e \approx \sum_{k=1}^{n_{nod}} N^k(\boldsymbol{\theta}) \bar{\mathbf{u}}^k; \quad \mathbf{X}^e \approx \sum_{k=1}^{n_{nod}} N^k(\boldsymbol{\theta}) \bar{\mathbf{X}}^k; \quad \mathbf{x}^e \approx \sum_{k=1}^{n_{nod}} N^k(\boldsymbol{\theta}) \bar{\mathbf{x}}^k, \quad (2.46)$$

where n_{nod} is the total number of nodes in one element. The upper bar in the variables are used to represent discrete nodal values. The variables $\boldsymbol{\theta}$ are the same curvilinear coordinates of section 2.1, and now they are considered acting at element level. In the literature these element coordinates are also denoted by $\boldsymbol{\zeta}$. Inside of the element, the curvilinear coordinates can take a value within the interval $[-1; 1]$ in order to facilitate the numerical integration along the elemental domain Ω^e . In the discretization of membranes and shells, where one dimension is very small (in direction of θ^3) compared to the other two (dimension θ^1 and θ^2), two dimensional elements are normally used. The local coordinate system is thus represented by a perfect square, when using quadrilateral elements (isosceles triangles in case of triangular elements), having a side length equal to 2. The shape of this perfect square is then independent of the position of the element in the real geometrical space (nodal position), and therefore independent of the referential configuration. As a direct consequence, there is a unique transformation from the elemental space to the real geometrical space for each finite element, depending on the nodal coordinates (see equations 2.46_{2,3}).

The approximation of the global displacement field and geometry is therefore a contribution of each finite element,

$$\mathbf{u} \approx \bigcup_{e=1}^{n_e} \sum_{k=1}^{n_{nod}} N^k(\boldsymbol{\theta}) \bar{\mathbf{u}}^k; \quad \mathbf{X} \approx \bigcup_{e=1}^{n_e} \sum_{k=1}^{n_{nod}} N^k(\boldsymbol{\theta}) \bar{\mathbf{X}}^k; \quad \mathbf{x} \approx \bigcup_{e=1}^{n_e} \sum_{k=1}^{n_{nod}} N^k(\boldsymbol{\theta}) \bar{\mathbf{x}}^k. \quad (2.47)$$

For the sake of simplification, assemble and sum symbols will be removed from the last equations.

$$\mathbf{u} = N^k(\boldsymbol{\theta}) \bar{\mathbf{u}}^k; \quad \mathbf{X} = N^k(\boldsymbol{\theta}) \bar{\mathbf{X}}^k; \quad \mathbf{x} = N^k(\boldsymbol{\theta}) \bar{\mathbf{x}}^k. \quad (2.48)$$

The covariant base vectors, in the domain of the corresponding element, can be now computed as

$$\mathbf{g}_i = \mathbf{x}_{,i} = \frac{\partial \mathbf{x}}{\partial \theta^i} = N_{,i}^k \bar{\mathbf{x}}^k = N_{,i}^k (\bar{\mathbf{X}}^k + \bar{\mathbf{u}}^k), \quad (2.49)$$

$$\mathbf{G}_i = \mathbf{X}_{,i} = \frac{\partial \mathbf{X}}{\partial \theta^i} = N_{,i}^k \bar{\mathbf{X}}^k. \quad (2.50)$$

Due to the fact that the unknown vector of nodal displacements $\bar{\mathbf{u}}^k$ is composed of the displacement of the individual degrees of freedom u_r , the variation of the displacement field $\delta \mathbf{u}$ can be written as

$$\delta \mathbf{u} = N_k \delta \bar{\mathbf{u}}_k = N_k \frac{\partial \bar{\mathbf{u}}_k}{\partial u_r} \delta u_r = \mathbf{u}_{,r} \delta u_r. \quad (2.51)$$

Finally, the variation of the covariant base vectors \mathbf{g}_i with respect to the independent parameters \mathbf{u} is computed as

$$\delta \mathbf{g}_i = \frac{\partial \mathbf{g}_i}{\partial u_r} \delta u_r = N_{k,i} \frac{\partial \bar{\mathbf{x}}_k}{\partial u_r} \delta u_r = N_{k,i} \frac{\partial \bar{\mathbf{u}}_k}{\partial u_r} \delta u_r = \mathbf{g}_{i,r} \delta u_r. \quad (2.52)$$

Considering that the reference configuration is independent of the displacement field \mathbf{u} , the variation of the related covariant base vector vanishes, $\delta \mathbf{G}_i = \mathbf{0}$.

In the same way, the linearization of the covariant base vectors has the following expression,

$$\Delta \mathbf{g}_i = \frac{\partial \mathbf{g}_i}{\partial u_r} \Delta u_r = N_{k,i} \frac{\partial \bar{\mathbf{x}}_k}{\partial u_r} \Delta u_r = \mathbf{g}_{i,r} \Delta u_r. \quad (2.53)$$

Variation and linearization of the strain tensors in terms of the discretized parameters u_r are computed using the variation and linearization of the covariant base vectors. For the Green-Lagrange strain tensor we have,

$$\delta \mathbf{E} = \frac{\partial \mathbf{E}}{\partial u_r} \delta u_r = \left[\frac{1}{2} (\mathbf{g}_{i,r} \cdot \mathbf{g}_j + \mathbf{g}_i \cdot \mathbf{g}_{j,r}) \mathbf{G}^i \otimes \mathbf{G}^j \right] \delta u_r, \quad (2.54)$$

and its linearization with respect to the degree of freedom u_s is formulated as (see equation 2.39),

$$\begin{aligned} \Delta \delta \mathbf{E} &= \frac{\partial}{\partial u_s} \left(\frac{\partial \mathbf{E}}{\partial u_r} \delta u_r \right) \Delta u_s = \frac{\partial^2 \mathbf{E}}{\partial u_r \partial u_s} \delta u_r \Delta u_s \\ &= \left[\frac{1}{2} (\mathbf{g}_{i,r} \cdot \mathbf{g}_{j,s} + \mathbf{g}_{i,s} \cdot \mathbf{g}_{j,r}) \mathbf{G}^i \otimes \mathbf{G}^j \right] \delta u_r. \end{aligned} \quad (2.55)$$

After discretization, the internal contribution to the principle of virtual work (2.42) and its linearization (2.43) change to the following expressions,

$$\delta W_{int}(\mathbf{u}) = \delta u_r \int_{\Omega_0} S^{ij} (\mathbf{g}_{i,r} \cdot \mathbf{g}_j) dV \quad (2.56)$$

and

$$\Delta \delta W_{int}(\mathbf{u}) = \delta u_r \int_{\Omega_0} \left[(\mathbf{g}_i \cdot \mathbf{g}_{j,r}) C^{ijkl} (\mathbf{g}_k \cdot \mathbf{g}_{l,s}) + (\mathbf{g}_{i,r} \cdot \mathbf{g}_{j,s}) S^{ij} \right] dV \Delta u_s. \quad (2.57)$$

The nodal parameters δu_r are constant nodal values and they are not affected by the integrals, therefore they can be extracted from them.

The contribution to the external virtual work in equation (2.28) gets the following form,

$$\delta W_{ext}(\mathbf{u}) = \delta u_r \int_{\Omega_0} \mathbf{B} \cdot \mathbf{u}_{,r} dV + \delta u_r \int_{\partial \Omega_0 \sigma} \hat{\mathbf{T}} \cdot \mathbf{u}_{,r} dS. \quad (2.58)$$

As already mentioned, pressure loading is considered dependent on the displacement field \mathbf{u} , and therefore its contribution to the linearization of the virtual work has to be include as well in the formulation (see section 5.2.2).

2.5.5 Solution of the Equilibrium Equations

The solution to the nonlinear system of equations in material parameters with respect to the nodal degrees of freedom \mathbf{u} is finally obtained by solving the linear approximation of the equilibrium equations as shown in formulation (2.33). The solution is obtained by iterative methods where a convergence criterion decides whether the solution is accurate enough depending on the requirements of the analyst. In case external loads are displacement independent, the discretized linearization in components by using the last two equations is given as,

$$0 = \left(\int_{\Omega_0} S^{ij} (\mathbf{g}_{i,r} \cdot \mathbf{g}_j) dV - \int_{\Omega_0} \mathbf{B} \cdot \mathbf{u}_r dV - \int_{\partial\Omega_0 \sigma} \hat{\mathbf{T}} \cdot \mathbf{u}_r dS \right) + \left(\int_{\Omega_0} \left[(\mathbf{g}_i \cdot \mathbf{g}_{j,r}) C^{ijkl} (\mathbf{g}_k \cdot \mathbf{g}_{l,s}) + (\mathbf{g}_{i,r} \cdot \mathbf{g}_{j,s}) S^{ij} \right] dV \right) \Delta u_s. \quad (2.59)$$

The first term in parenthesis in the previous system (2.59) contains the r^{th} component of the so called residual force vector R_r , which represents the difference between internal and external forces and whose value vanishes at any equilibrium configuration.

$$R_r = \frac{\partial W}{\partial u_r}. \quad (2.60)$$

The second term, contains the linear approximation of the slope of the residual vector in the direction of the nodal displacement (internal parameter) Δs , and represents the (r, s) component of the tangent stiffness matrix of the linearized system,

$$\frac{\partial R_r}{\partial u_s} = K_{rs}. \quad (2.61)$$

This term is used to equilibrate the residual force vector by iteratively finding a suitable geometry \mathbf{x} through increments in displacements Δu_s ,

$$R_r + K_{rs} \Delta u_s = 0. \quad (2.62)$$

The final geometry will thus at the end generate a system which is in equilibrium with the external applied forces.

In section 5.2 and more specific in section 5.2.1 incremental-iterative methods for the solution of the non-linear system of equations are briefly reviewed, in the context of stability analysis. In this way, the equilibrium path is characterized by discrete points of the solution space.

Chapter 3

Form Finding

The present chapter contains an overview of the form finding method. It shows how the method is applied to the design of membranes, and its contribution to the design of thin-walled shells. Some examples applied to the bulkhead-concepts introduced in section 1.2.3 are calculated.

Detail description of numerical solutions in the field of form finding, can be found for instance in references [Ble98], [Wüc07] and cited literature therein. For reference about structural behavior and analysis of membrane structures see for instance [FM04] and [Koc04].

3.1 Overview of the method

The form finding process is used in the design of structures composed of flexible cables and membranes which possess a negligible resistance under compression. Due to this special property, such structures have to be stabilized by a pre-stress state consisting in tensile stresses. Afterwards they can be exposed to the action of real loads. Form finding is the tool that finds the shape of the structural surface which is in equilibrium with the given pre-stress state.

The most important component in the process is the stress state to be reached, since it is the driving design parameter for the final solution. Displacement restrictions along the border of the membrane and an initial surface used as a starting reference are the additional components. The configuration of the boundary condition, which could be fixed ($\hat{\mathbf{u}} = \mathbf{0}$) or flexible (by adding cable components), is the responsible of generating surfaces with high or low curvatures for a given stress state. The geometry of the initial surface is of less importance in the results, since different initial configurations will end up with the same final shape.

Form finding, compared to the classical structural analysis, is considered as an inverse problem, since the stress state in the deformed configuration is known in advance. This fact presents some numerical problems for which several solutions have been proposed [Wüc07].

The equilibrium equation of the form finding problem for a given in-plane stress state σ , with respect to the deformed configuration, is given by

$$\delta w_{int}(\mathbf{u}) = \int_{\Omega} \sigma : \delta \mathbf{e}(\mathbf{u}) \, dv = 0, \quad (3.1)$$

which was derived from equation (2.29) without considering body forces and applied surface loads. Using equation (2.40) for the variation of the Almansi strain tensor $\delta \mathbf{e}$, the symmetrical properties of the Cauchy stress tensor σ and a constant thickness distribution t , the last equation can be written as [Ble98],

$$\delta w_{int} = t \int_{\Omega} \sigma : (\delta \mathbf{F} \cdot \mathbf{F}^{-1}) \, da = 0. \quad (3.2)$$

The equilibrium equations of motion are formulated with respect to the deformed configuration, where the target stress state σ is given as a direct parameter independent of any material constant. Thus, the stress state which is constant through the thickness, is assumed to be generated no matter which kind of material is used. In order to formulate the problem in the undeformed configuration one has to make use of equation (2.22), which takes the form

$$da = \det(\mathbf{F}) \, dA. \quad (3.3)$$

Finally, equation (3.1) changes to

$$\delta w_{int} = t \int_{\Omega} \sigma : (\delta \mathbf{F} \cdot \mathbf{F}^{-1}) \det(\mathbf{F}) \, dA = 0, \quad (3.4)$$

or in components (again using equation (2.40) and the symmetrical property of the stress tensor):

$$\delta w_{int} = t \int_{\Omega} \sigma^{\alpha\beta} (\delta \mathbf{g}_{\alpha} \cdot \mathbf{g}_{\beta}) \det(\mathbf{F}) \, dA = 0, \quad (3.5)$$

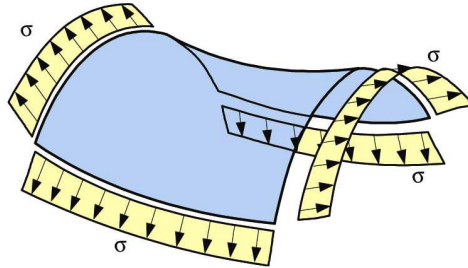


Figure 3.1: In-plane stress. Source [Wüc07].

3.2 Applications of formfinding

Form finding is a method specially developed for the design of membrane structures, where tensile stresses drive the configuration of the equilibrium shape. The large in-plane dimensions compared to the thickness and the absence of bending stiffness results in a vulnerable

structure under compression stresses. Even though compression stresses could appear only at local sections of the surface, undesirable deformations could lead to configurations far deviated from a satisfactory shape. In a less critical scenario, wrinkles would still affect the architecture of the final construction [FM04].

In the design of light weight structures, form finding is used in a preliminary stage, where the target stress field is composed of loads that are mean to induce the final equilibrium shape. Not only the previously stabilizing tensile stress field might be considered, but also long-lasting external loads that will influence the geometry as well. One well known example of this kind of problems are some inflatable structures under the influence of pressure load, where pressure is commonly combined with in-plane tensile stresses [Koc04]. Short term loads (for instance wind and snow) are then considered in a second stage, where classical structural analysis is addressed [BW04]. In reference [Wüc07] form finding is integrated into a fluid-structure interaction process, where the coupling between structural analysis and form finding is achieved through the equilibrium configuration.

On the other hand, thin-walled shell structures are commonly designed to carry external loads mainly by means of tensile and compressive stresses. Even though shells are able to balance applied loads by means of bending stresses, they are avoided as much as possible, in order to make optimal use of the material [BWDC05]. Thin-walled shells tend to generate large deformations when an important fraction of the applied load is compensated by bending stresses. These deformations could go over pre-established limits and involve the functionality of adjacent structures, and could even endanger the overall structural stability of the system (see chapter 5).

3.2.1 Form finding in the design of pressurized thin-walled shell structures

As already mentioned in the first chapter, form finding is used along this work for the purpose of defining an suitable geometry in the design of pressurized bulkheads. The generated geometry is then considered for a structural analysis stage where real loads are applied in a two-stage design process similar to the previously mentioned design of membranes. A very important difference compared to the design of membranes, is that shell do not need the stabilizing effect of the in-plane stress state. Therefore, in-plane stress is only considered for the shape generation and disappears in the later structural analysis. For this reason, the stress state does not need anymore to be called pre-stress, but rather stress state, since it is not a real load acting on the structure.

3.2.1.1 Computation of Equilibrium Shapes

The stress state to be reached in the computation consists of fictitious loads whose magnitudes have no relation with the real physical loading, even though the type of load might be the same, as it is the case of pressure. This fact is explained in more detail in table 3.1 of

section 3.2.1.2.

Figure 3.2 shows three different equilibrium configurations for the surfaces of the extended concept. All of them were obtained by means of form finding. The difference lies on the value of the target stress state and the presence of pressure as additional load. Boundary and arches of the bulkhead are kept fixed during form finding as it is also the case for all other concepts.

Minimal Surfaces Surfaces of minimal area are usually suitable for design due to architectural reasons. They are the obvious alternative for problems where structural weight is the principal response to be considered. This kind of surfaces are experimentally generated using soap-film models, method that was successfully exploited in the past for the design of membrane structures, when numerical models were not yet developed (see figure 1.6(b)). Minimal surfaces are obtained when the membrane is subjected to an homogeneous and isotropic stress state, where principal stresses have the same value at every point on the surface and in all directions. One of their principal characteristics is that the mean curvature H at every point on the surface is equal to zero,

$$H = \frac{1}{2} \left(\frac{1}{R_1} + \frac{1}{R_2} \right) = 0, \quad (3.6)$$

where R_1 and R_2 are the principal radii of curvature. In other words, the principal curvatures, κ_1 and κ_2 , have the same magnitude and opposite directions. As a direct consequence, in the general case, the Gaussian curvature is less than zero

$$K = \frac{1}{R_1} \frac{1}{R_2} < 0, \quad (3.7)$$

one essential characteristic of anticlastic surfaces. The particular case for which $H = 0$ and also $K = 0$, appears when the prescribed boundary lies in one plane. The minimal area is nothing else than a flat shape. Furthermore, when the Gaussian curvature of a surface is equal to zero ($K = 0$) at every point on it, it is classified as a developable surface.

The governing equations of form finding for the case of homogeneous and isotropic stress state is obtained from equation (3.4), where the stress tensor is replaced by the identity tensor (see equation 2.20) multiplied by a constant value $\sigma = \bar{\sigma} \mathbf{I} = \bar{\sigma} g^{\alpha\beta} (\mathbf{g}_\alpha \otimes \mathbf{g}_\beta)$,

$$\delta w_{int} = t \bar{\sigma} \int_{\Omega} g^{\alpha\beta} (\mathbf{g}_\alpha \otimes \mathbf{g}_\beta) : (\delta \mathbf{F} \cdot \mathbf{F}^{-1}) \det(\mathbf{F}) dA = 0, \quad (3.8)$$

and in components,

$$\delta w_{int} = t \bar{\sigma} \int_{\Omega} (\delta \mathbf{g}_\alpha \cdot \mathbf{g}^\alpha) \det(\mathbf{F}) dA = 0, \quad (3.9)$$

Figure 3.2(a) shows an example of minimal surfaces calculated on the extended concept by means of form finding.

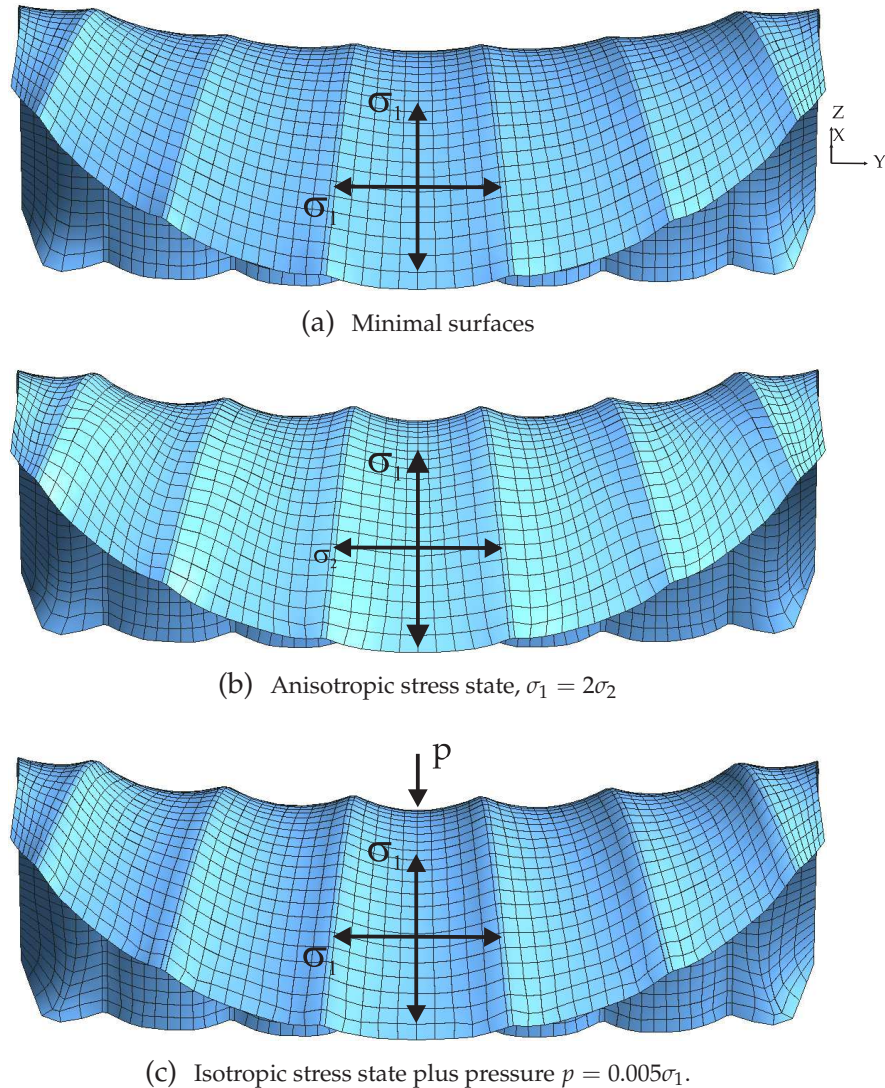


Figure 3.2: Form finding on extended concept.

Anisotropic stress state An anisotropic stress state is usually addressed in case minimal surfaces generate flat shapes with low curvatures, and rather higher curvatures are needed without modifications in the boundary configuration. This is the case when boundary modifications are too restrictive. Nevertheless, an increment in the surface area and the consequent increment in structural weight will occur when deviating from minimal surfaces. The increment in curvature and volume of the structure, will depend on the ratio of the principal stresses, σ^1/σ^2 . The use of anisotropic stresses is obligatory in some cases where a minimal surface is physically not possible to obtain [Lin09].

It has been demonstrated [Lin09] that the angle α on the surface between principal stresses must be $\alpha = 90^\circ$, in order to reach a mechanically feasible state. The outcome of this fact, is that only orthotropic stress states should be used to solve the form finding problem.

Figure 3.2(b) contains an example of anisotropic stress state in form finding. The FE-

mesh of this example is slightly distorted due to convergence problems which arise when a constant anisotropic stress field has to be reached. A constant anisotropic field cannot be exactly computed when the generated surfaces are not developable [Lin09]. In these cases, a solution which is very close to the constant anisotropic stress field is calculated.

Pressure Load In addition to the in-plane stresses, other type of external loads could also be included. Due to the normal-to-surface direction of pressure loads, two important facts arise as direct consequence. The first one is that pressure is the only additional external load that can lead to a final homogeneous stress state, since it does not modify the in-plane (tangent to the surface) stress at the point of application. It rather requires a geometrical modification around the point of application in order to balance the load in normal direction ([Lin09]). For an isotropic and homogeneous stress state, the addition of pressure difference produces a mean curvature different from zero $H \neq 0$, compared to minimal surfaces. The value of the mean curvature is proportional to the additional pressure difference, as it can be derived from the Young-Laplace equation,

$$p = n \left(\frac{1}{R_1} + \frac{1}{R_2} \right), \quad (3.10)$$

where n is the value of the isotropic stress per unit length. R_1 and R_2 are the principal radii of curvature. Equation (3.10) describes the equilibrium of forces normal to the surface at a selected point.

The other important characteristic of pressure loads is that in a nonlinear analysis, at each incremental step (see section 5.2), the direction of application depends on the current normal-to-surface direction. This type of load are called follower forces. The external virtual work contributed by this kind of load is shown in section 5.2.2 equation (5.22) and reproduced as follows,

$$\begin{aligned} \delta W_{ext}(\mathbf{u}) &= \int_{\partial\Omega_\sigma} \hat{\mathbf{t}} \cdot \delta \mathbf{u} da = \int_{\partial\Omega_\sigma} \hat{p} \mathbf{n} \cdot \delta \mathbf{u} da \\ &= \hat{p} \int_{\partial\Omega^\theta} (\mathbf{g}_1 \times \mathbf{g}_2) \cdot \delta \mathbf{u} d\theta^1 d\theta^2, \end{aligned} \quad (3.11)$$

which is written with respect to the convective coordinates θ^1 and θ^2 and using equations (5.23) for the formulation of the surface area da . The normal-to-surface vector is equal to $\mathbf{n} = \mathbf{g}_3$ as in equation (2.8).

Pressure load is used to find the undeformed configuration of inflatable structures, and it is a good alternative in the generation of doubly curved surfaces with sinclastic properties, where the Gaussian curvature is greater than zero, $K > 0$. In case of isotropic stress state and circumferential boundary conditions lying in one plane, different sections of a sphere are the outcome. The magnitude of these spheres will depend on the proportion between applied pressure and in-planes stress.

Figure 3.2(c) shows the equilibrium surfaces of the extended concept calculated using pressure load equal to 0.5% of the in-plane applied stress ($p = 0.005\sigma_1$).

3.2.1.2 Structural Analysis

The second step in the design of pressurized bulkheads after form finding, is structural analysis. It does not mean that this stage is restricted to only one structural analysis itself, but it rather refers to any process where structural analysis is involved. As already mentioned in the first chapter, form finding is also connected to a shape optimization process, where the shape obtained by means of form finding is used as starting design in the optimization loop.

Between form finding and the subsequent structural analysis there are remarkable differences regarding: loading, boundary conditions, element formulation, and initial configuration, that need to be distinguished. Table 3.1 contains a detail comparison between both design stages.

Description	<i>Form Finding</i>	<i>Structural Analysis</i>
Goal	finding a suitable shape	real structural study
Element Theory	membrane	shell
Loading	loads which generate shape	true load cases
In-Plane Stress	arbitrary ratio for principal stresses	NOT PRESENT
Pressure Load (+ Load Cases)	ONLY IF REQUIRED (magnitude depends on in-plane stress)	real magnitude
Boundary Cond.	fixed along all boundaries of surface(s)	real boundary conditions
Initial Config.	any surface enclosed by the boundary (within reasonable limits)	shape after form finding

Table 3.1: Comparison between form finding and structural analysis.

3.3 Numerical Solution - Update Reference Strategy

Since in form finding the final stress state is already known before the final shape is calculated, some difficulties arise which are not found in standard structural analysis. A direct solution to the formulation presents numerical problems in case all three displacements of the free nodes of the FE-mesh are considered as unknown. The degrees of freedom tangential to the equilibrium shape could take any position along the optimal surface without modifications of the equilibrium equations. This situation leads to more than one solution for the formulation (3.1). As a consequence, the system stiffness matrix is singular with respect to tangential shape variations. Nevertheless, nodal movements tangential to the equilibrium surface cannot be discarded as variables, since the equilibrium shape is not known in advanced. The second reason is because such directions are fundamental when including cable elements in the design of membrane structures [BR99]. Thus, a regularization method

has to be considered to solve the problem. Several methodologies have been developed by many authors since the seventies of the last century. Wüchner describes in [Wüc07] the basic ideas of several methods to approach the singular problem. In this report, only one of these methodologies is mentioned. The method is called Update Reference Strategy [Ble98], [BR99], which is used to solve a modification of the original problem by the use of an homotopy method. Homotopy methods approach the solution of a singular problem by solving a modified one. The solution of the modified problem reaches the original solution as the modified problem is progressively converted into the original one through the parameter λ , which is incremented at each iteration step. The modified problem $f_\lambda(x)$ is then constructed as a linear interpolation between the original singular problem $f(x)$, and the related one $\bar{f}(x)$. Since the related problem is not singular, its solution is assured to be found. The linear interpolation between original and related problem is given by:

$$f_\lambda = \lambda f(x) + (1 - \lambda) \bar{f}(x), \quad (3.12)$$

whose solution approaches the original one x^* as the parameter λ goes from 0 to 1.

The chosen related problem $\bar{f}(x)$ that conforms with the linear interpolation (3.12) is also the equilibrium equation of motion, but formulated with respect to the reference configuration. The 2^nd Piola-Kirchhoff stress tensor \mathbf{S} , is now assumed to be given instead of the Cauchy stress tensor σ . The related function is then taken from equation (2.28) excluding the contribution of the external forces to the virtual work,

$$\delta W_{int}(\mathbf{u}) = \int_{\Omega_0} \mathbf{S} : \delta \mathbf{E}(\mathbf{u}) dV = 0. \quad (3.13)$$

The modification of the form finding problem is consequently written as,

$$\begin{aligned} \delta W_\lambda &= \lambda \delta W_\sigma + (1 - \lambda) \delta W_S \\ &= \lambda \left[t \int_{\Omega} \det \mathbf{F} \sigma : \delta \mathbf{e} dA \right] + (1 - \lambda) \left[t \int_{\Omega_0} \mathbf{S} : \delta \mathbf{E} dA \right]. \end{aligned} \quad (3.14)$$

In equation (3.14) it is considered that the thickness t remains constant during deformation. The Cauchy stress tensor σ of the original problem as well as the 2^nd Piola-Kirchhoff stress tensor \mathbf{S} of the related problem take the value of the given stress state, σ^* , the target stress to be reached. This means that in the related formulation δW_S , the real stress state σ^* referred to the actual configuration, is now given with respect to the known reference configuration ($\mathbf{S} \equiv \sigma^*$). Therefore, after solving the related problem,

$$\delta W_S = t \int_{\Omega_0} \mathbf{S} : \delta \mathbf{E} dA \quad (3.15)$$

the final stress state in (3.15) will differ from the given one (σ^*) due to large deformations the structure experiences.

The URS formulation solves the modified problem (3.14) for a suitable choice of the parameter λ . The Cauchy and the 2^nd Piola-Kirchhoff stress tensors are defined as the target

stress state at the beginning of every form finding iteration, and the actual configuration \mathbf{x} of the previous step is used as reference configuration \mathbf{X} for the next step. Thus, at each form finding iteration ($i + 1$) we have:

$$\begin{aligned}\sigma^{\alpha\beta (i+1)} &= \sigma^{\alpha\beta *} \\ \mathcal{S}^{\alpha\beta (i+1)} &= \sigma^{\alpha\beta *} \\ \mathbf{X}^{(i+1)} &= \mathbf{X}^{(i)} + \mathbf{u}^{(i)} = \mathbf{x}^{(i)}.\end{aligned}\tag{3.16}$$

3.3.1 Discretization and Linearization

The set of equilibrium equations in the modified problem (3.14) are nonlinear formulations with respect to the unknown parameters \mathbf{u} . The linearization of the equilibrium equations is, at this point, a prerequisite for the solution of the problem by means of numerical approximations as the Newton-Raphson method.

After discretizing the equilibrium equations using finite elements, the linear approximation of the equilibrium equations can be expressed in terms of the residual force vector and the tangent stiffness matrix as shown in section 2.5.5.

For the original problem δw_σ , the residual force vector (from equation 3.5) for a degree of freedom u_r is calculated as,

$$R_r^\sigma = t \int_{\Omega} \det(\mathbf{F}) \sigma^{\alpha\beta} (\mathbf{g}_{\alpha,r} \cdot \mathbf{g}_\beta) dA = 0.\tag{3.17}$$

The component K_{rs} of the tangent stiffness matrix is obtained by linearizing the residual force vector in direction Δu_s ,

$$K_{rs}^\sigma = t \int_{\Omega} \left[\left(\det(\mathbf{F}) \sigma^{\alpha\beta} \right)_{,s} (\mathbf{g}_{\alpha,r} \cdot \mathbf{g}_\beta) + \det(\mathbf{F}) \sigma^{\alpha\beta} (\mathbf{g}_{\alpha,r} \cdot \mathbf{g}_{\beta,s}) \right] dA = 0.\tag{3.18}$$

The derivative of the base vectors with respect to the first considered degree of freedom in equation (3.17) is not affected by linearization along direction Δu_s due to the fact that they are already affected by the variation δu_r . On the other hand, in the first term of equation (3.18), the covariant base vectors that belongs to the Cauchy stress tensor σ are dependent on the nodal parameters and therefore have to be considered in the linearization process [Ble98].

For the related problem δW_S , residual force vector and related tangent stiffness matrix were already derived in section 2.5.5. The base vectors of the 2nd Piola-Kirchhoff stress tensor \mathbf{S} are independent of the displacement field. Therefore, its gradients with respect to the free parameters in the linearization process vanish, so that the first term in equation (2.57) is canceled out. Thus, residual force vector and tangent stiffness matrix of the related problem are finally computed as,

$$R_r^S = \int_{\Omega_0} S^{ij} (\mathbf{g}_{\alpha,r} \cdot \mathbf{g}_\beta) dA\tag{3.19}$$

and

$$K_{rs}^S = \int_{\Omega_0} (\mathbf{g}_{\alpha,r} \cdot \mathbf{g}_{\beta,s}) S^{ij} dA. \quad (3.20)$$

For the given tensile stress σ^* , equation (3.20) is positive definite if λ is small enough. This ensures the necessary regularization of the modified problem δW_λ . If the parameter λ is set to zero, the modified problem is converted into the robust related one, which is even linear with respect to the nodal displacements, and is solved within one iteration step. In this case, the form finding iterations have to be increased in order to achieve a good convergence.

Linearization of Pressure Load The linearization of the contribution of the pressure load for fixed boundary conditions is given by

$$\Delta \delta W_{ext}(\mathbf{u}) = \frac{\hat{p}}{2} \int_{\partial\Omega^\theta} [\Delta(\mathbf{g}_1 \times \mathbf{g}_2) \cdot \delta \mathbf{u} + \delta(\mathbf{g}_1 \times \mathbf{g}_2) \cdot \Delta \mathbf{u}] d\theta^1 d\theta^2. \quad (3.21)$$

as shown in section 5.2.2.

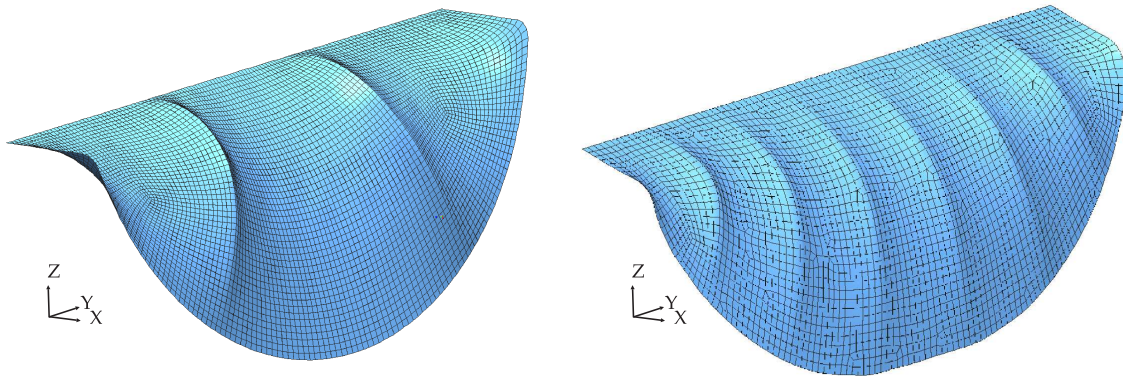
3.3.2 Regularization Due to Incompatible Stress Field

There are some cases in which the URS cannot generate a final geometry and the process fails numerically showing an increasingly distorted mesh after each update of the stress field. This effect appears commonly in cases where the combination of the target stress state and the configuration of the boundary do not allow a real solution to be found. Another disadvantageous situation occurs when different target stresses are imposed to different sub-domains of the surface, translated into incompatible stress states at domain-boundaries. Wüchner proposes in [Wüc07] a solution for incompatible stresses, which modifies the target stress fields based on allowable stretch limits. The method is able to control element distortion giving feasible solutions.

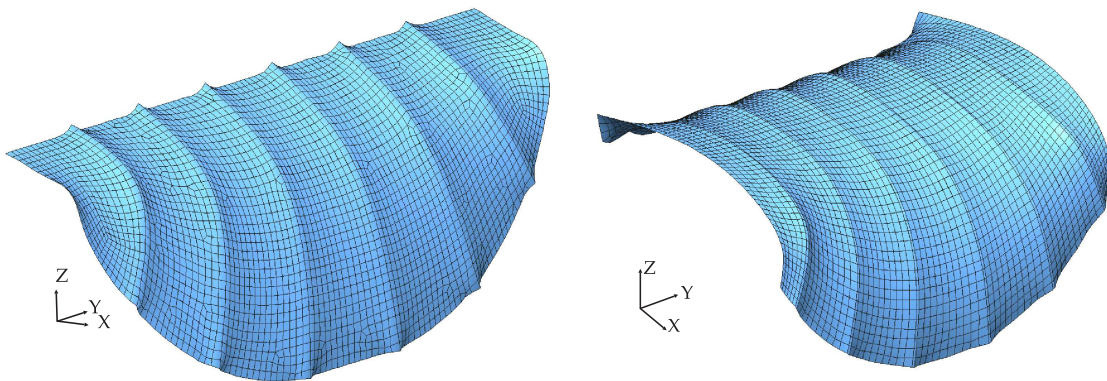
3.4 Generation of Surfaces for Different Concepts

As already mentioned in chapter 1 the new different concepts including arches as the principal structural topology, as shown in figure 1.9, consist basically on a geometric frame including the arches and surfaces connecting the frame. This frame includes the outer boundary as well as the curves defining the fixed arches. In all following examples the surfaces between arches are computed as the equilibrium configuration for the given stress state using form finding. These configurations will be named as Concepts using letters from A to D in the same order as they appear in figure 1.9. For all examples, the directions of the principal stresses were set along the global directions x and y . The plane xy containing the principal directions was later projected onto the finite element mesh to calculate the principal directions at element level [Wüc07].

Figure 3.3 contains the finite-element meshes of the four Concepts. They represent the equilibrium configuration for an homogeneous and isotropic target stress leading to minimal surfaces.



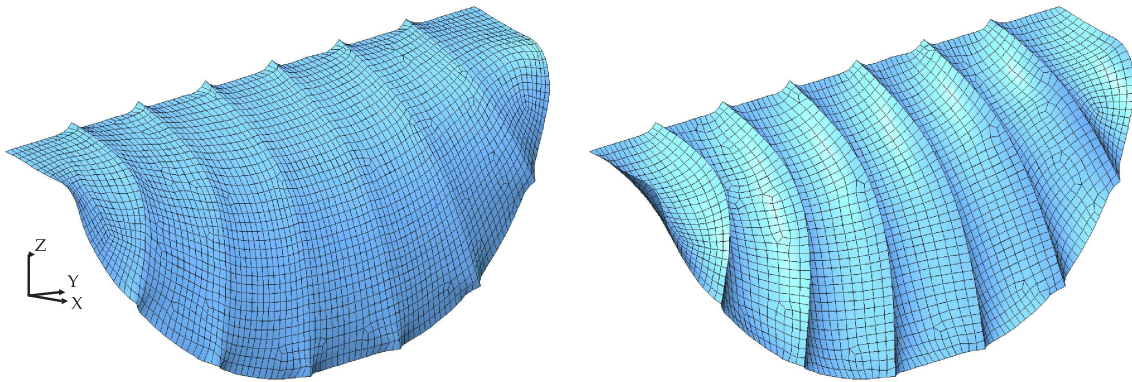
(a) Two arches. 17130 d.o.f. & 5570 elements. Concept A. (b) Six arches. 8913 d.o.f. & 2862 elements. Concept B.



(c) B.C. modification. 9444 d.o.f. & 3031 elements. Concept C. (d) Final extension. 10557 d.o.f. & 3400 elements. Concept D.

Figure 3.3: Arch concepts. Minimal surfaces, equilibrium configuration.

Figure 3.4 shows two extreme variations of minimal surface for Concept C with the purpose of comparison and showing how geometries can be shaped using form finding. Compare with figure 3.3(c).



(a) Concept C, $\sigma_1 = 3\sigma_2$

(b) Concept C, isotropic stress & $p = 0.02\sigma_1$

Figure 3.4: Concept C. Variation of minimal surfaces.

Chapter 4

Free Form Surfaces in CAGD-Based Shape Optimization using B-Splines

The focus of this chapter is to characterize the geometrical model for shape optimization of pressurized thin-walled shell structures, and how it is obtained. As explained in chapter 3, form finding has been used previously to compute a suitable starting design for the subsequent shape optimization step of the design process. The generation of a good initial configuration in shape optimization gives a certain warranty that the optimal shape will not deviate dramatically from it. In this context the designer has somehow already decided about the general topology of the shell for the final optimum. Furthermore, it is known that the optimal design of a nonlinear optimization problem found with the help of a gradient-based optimizer will end up in the next local minimum, and it is strongly influenced by the initial guess.

The equilibrium configuration after form finding offers in advance a reduced volume when employing minimal surfaces, as well as suitable doubly-curved shapes when deviating from minimal surfaces for an adequate resistance to the external loads by increasing curvatures. Now the geometry has to be adjusted to the real loads and boundary conditions during optimization.

The selection of the design model and number of variables for shape optimization also depends on the degree of freedom the designer wants to give to the shape in order to deviate from the initial design. Another important aspect to be considered is the quality of the final geometry in terms of manufacturing requirements. Even though the complete structure is modeled using a quasi-isotropic material to simplify calculations, the final design has to be fabricated according to specifications for composite material. Thus, physical characteristics like smoothness avoiding sharp changes in curvature become important.

In the following sections, free form surfaces for shape optimization are characterized. Afterwards, a short description of non-rational and rational B-splines is given, which is the type of free form surface selected as geometrical model. Finally, it is explained how this geometrical model is obtained from a set of nodal coordinates by means of surface fitting.

4.1 Introduction

The need for flexible geometrical models was first coming from the ship industry and later from aircraft and automotive industries, as a requirement for the construction of shaping tools used for design. The first designing tools were constructed using flexible materials as a result of several physical experiments.

The appearance of computer languages allowed the implementation of mathematical algorithms for geometrical modeling, situation that gave birth to the CAGD discipline among others. Computer Aided Geometrical Design deals with the study of mathematical algorithms which are meant to be implemented in an arbitrary computer language, so that they can be employed together with visualization tools (rendering) in interactive analysis and design of geometrical models representing real shapes.

Throughout several mathematical investigations, Bézier curves and surfaces became the most important instrument to this aim, which was later combined with B-splines and rational B-splines (NURBS) due to additional flexibility in geometrical representation.

4.2 Free Form Surfaces - Parametrical Representation

Free form surfaces are characterized for having the flexibility of modeling a wide variety of 3D-shapes as it can be found in computer graphic developments. The usual way of describing this kind of surfaces is using a parametrical description where geometric coefficients \mathbf{P}_i (also known as control points, CP) defined in the real Euclidean space \mathbb{R}^3 are interpolated with the help of basis functions as shown by equation (4.2). They are a set of linearly independent functions Φ defined in the parametrical space \mathbb{R}^2 , also known as blending or shape functions.

Figure 4.1 shows the mapping of each point (u, v) of the two-dimensional parametrical space into the three-dimensional Euclidean space, $\mathbf{x}(u, v) = (x(u, v), y(u, v), z(u, v))$, by using the surface representation $\mathbf{S}(u, v)$. Parameters u and v are real numbers within the closed interval $[a, b]$. The boundaries of the interval a and b , may take any positive value which is usually normalized to 0 and 1 respectively.

The projection of the two-dimensional plane uv onto the real surface generates the curvilinear coordinates u and v of the real structure (see Figure 4.1), which correspond to the curvilinear parameters θ^1 and θ^2 from previous chapters (see Figure 2.1). The new notation introduced in this chapter for the curvilinear coordinates u and v , is related to a single surface patch representing only the section to be optimized. It could be a specific region of a structural member, the complete member itself or even a combination of sections corresponding to adjacent components. In the same way, different regions to be optimized, could be modeled using different surface representations $\mathbf{S}^k(u, v)$. In the last case, common edges

should be modeled in such a way, so that required continuities can be maintained between representations.

The surface representation $\mathbf{S}(u, v)$ corresponds to the geometrical model of the midsurface of the analysed shell (Figure 4.1). The spacial location of upper and lower layers of the shell will be subjected to the value of the thickness of the corresponding finite element. In case the thickness distribution of the shell is given by a parameter-dependent function $t(u, v)$, upper and lower layer of the shell could be derived by adding (or subtracting) to the middle surface representation $\mathbf{S}(u, v)$ the half of the thickness distribution function $t(u, v)$ in normal direction \mathbf{n} at the corresponding selected point (u^*, v^*) [Ble90],

$$\mathbf{S}_{u/l}(u, v) = \mathbf{S}(u, v) \pm \frac{1}{2} t(u, v) \mathbf{n}(u, v). \quad (4.1)$$

In reference [Sch95], the thickness distribution of thin-walled structures is also obtained from a parametrical free form surface, which is used as design model in a sizing optimization problem. Some control points are selected as design variables and linked to the optimization variables in order to compute the optimal thickness distribution. Thus, the area of the different plies of fibers along the thickness, in the context of composite material, can be calculated.

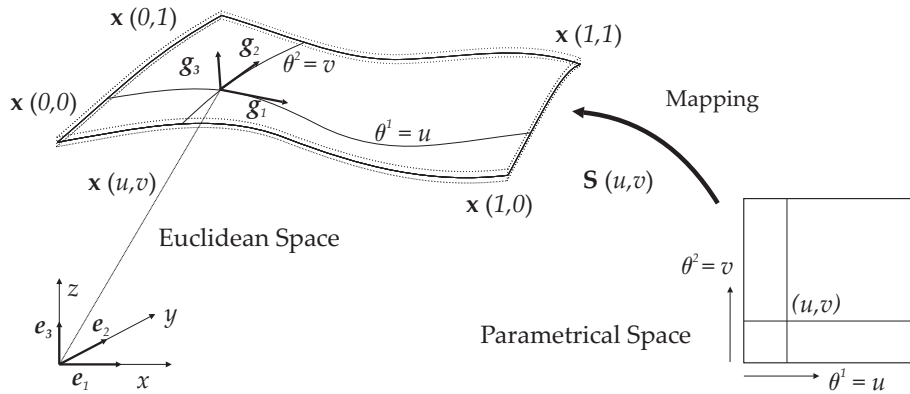


Figure 4.1: Parametrical representation of a surface.

4.3 Shape Modification

The formulation of the parametrical representation has the general form,

$$\mathbf{S}(u, v) = \sum_{i=1}^n \Phi_i(u, v) \mathbf{P}_i. \quad (4.2)$$

The shape is thus defined by the linear combination of the control points \mathbf{P}_i and the corresponding bases Φ . Control points are distributed over the real space, and represent the free

parameters for the shape control (see figure 4.2). The polynomial degree of the basis functions is another factor that affects shape control and implies different degrees of accuracy in modeling the surface.

In the literature, a single entity $\mathbf{S}(u, v)$ is known as *design element*, also called super element or macro element due to the fact that from these elements sub-elements for structural purposes are generated, the finite elements.

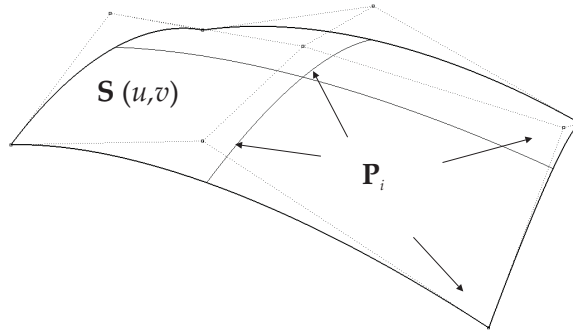


Figure 4.2: Control points P_i of surface $\mathbf{S}(u, v)$.

In fact, the parametrical representation of design elements employs the same principle as finite elements in the sense that they use shape functions and nodal coefficients in order to characterize the geometry. Actually, the geometrical model used to find the equilibrium shape in form finding is based on the isoparametric concept (see section 2.5.4) where displacement field and geometry are approximated using the same shape functions and nodal positions.

4.3.1 Geometrical Model and its Parameterization

Besides from the standard geometrical parameterization based on design elements (CAD-parameterization), the FE-parameterization of the geometrical model arises as an alternative (among others [Cam04]). It uses the degrees of freedom of the FE-mesh as design parameters as in form finding (see section 3.3). The same geometrical model for the isoparametric concept in finite elements is taken for the definition of the design model. Consequently, no additional geometrical description is needed and structural variables are directly used as design variables (see section 6.1.2).

A detailed comparison between FE- and CAD-parameterization is given by Camprubí in reference [Cam04] and Daoud in reference [Dao05]. The major advantage of the FE-parameterization is the higher freedom of possible shapes that can be achieved due to the big number of design parameter. At the same time, this higher freedom of shape can lead to undesired configurations characterized by mesh-dependent waviness, which affects the shape of finite elements [Dao05]. Inadequate mesh distortions might generate problems in structural analysis and influence the outcome of the optimization process. Stabilization

methods and filter techniques are used for out-of- and in-plane regularization of shape or sensitivities [DCB05], [FWB07], [FWB09]. References [BFLW08] and [Cam04] mention some of these methods and supply general literature about this topic. Using adequate controlling techniques shape optimization using FE-parameterization can successfully produce suitable shape modifications over small regions in order to manipulate the local stiffness.

FE-based optimization is a good alternative for generating preliminary designs due to the higher freedom in shape. For instance when the structural topology of the model is not predefined. As already mentioned at the beginning of this chapter, the presence of an initial design for optimization as a result of form finding, assumes that the final optimum should not deviate dramatically from its configuration. In this case, the CAD-parameterization appears to be a good alternative, since it allows a mesh independent selection of design parameters. Thus, a reduction of local minima is possible by restricting the space of potential undesired shapes. Another big advantage of CAD parameterization is the smoothness of the final design, which is a valuable property for manufacturing purposes. The optimal geometry of design elements could be used without modifications for construction techniques. For instance determination of the path for fiber reinforcement or layout of different plies when using composite materials ([Sch95]). Another very important criteria for deciding about which kind of parameterization is to be implemented is the characteristic of the data organization of the software to be used, which can be more or less suitable for one or other parameterization.

The quality of the finite element mesh is not locally affected when modifying design variables in CAD-based optimization, as compared to FE-based optimization. Nevertheless, FE-distortions are also expected. The change of the coordinates of a design variable along a preselected direction causes the modification of the design element over a certain region that usually contains several finite elements. Therefore, a distortion of a design element would finally lead to a distortion at finite element level. This problem can be treated by generating a new non-distorted FE-mesh after a certain number of optimization iterations. There exists also the possibility of restarting the optimization with a new mesh configuration.

A closer relationship between CAD-based geometrical model and finite element formulations is presented by Huges et al. in reference [HCB05]. An isogeometric approach using NURBS is presented, meaning that the same geometrical model is to be used for finite element interpolation. For instance, in reference [KBW09] an isogeometric rotation-free shell element is proposed for geometric nonlinear analysis based on the Kirchhoff-Love formulation. Isogeometric shape optimization is a relative new field of research ([WFC08], [CH09]).

The quantity and quality of distribution of control points when using design elements is given by the compromise of two fundamental requirements: as much geometrical freedom as possible in order to generate a higher number of feasible configurations, and as less design parameters as possible in order to decrease the probability of numerical drawbacks in mathematical optimization [Ble90].

The Free form representation used along this work, is the B-spline surface. It was chosen

because of its high flexibility in representing geometry. Complex shapes can be represented by using only a single patch. The rational variation of B-Splines, NURBS (Non-Uniform Rational B-Splines), enlarges the flexibility of surface description, since conical sections can also be modeled. The mathematical formulation of B-splines and other types of free form surfaces are found in CGAD-related textbooks. For instance in references [PT97], [Far99], [Far02], [CRE01] and [Rog01].

4.3.2 B-Splines

The mathematical formulation of a B-spline curve $C(u) : \mathbb{R} \rightarrow \mathbb{R}^3$ of polynomial degree p (order $p+1$) is given by

$$\mathbf{C}(u) = \sum_{i=1}^n N_{i,p}(u) \mathbf{P}_i; \quad a \leq u \leq b. \quad (4.3)$$

The piecewise property of a B-spline curve is a consequence of its knot vector

$$\mathbf{U} = \{a, u_2, \dots, u_i, \dots, u_{r-1}, b\}, \quad (4.4)$$

whose knot spans define regions on the domain $[a, b]$ influenced by a certain function $N_{i,p}$ and control point \mathbf{P}_i .

Since geometrical models usually interpolate first and last control points, the knot values u_i take the general *open* distribution

$$\mathbf{U} = \{\underbrace{a, \dots, a}_{p+1}, u_{p+2}, \dots, u_i, \dots, u_{r-p-1}, \underbrace{b, \dots, b}_{p+1}\}, \quad (4.5)$$

where the number of knots r is computed as $r = n + p + 1$. First and last knots have multiplicity equal to $p + 1$.

In the same manner, a B-spline surface representation $S(u, v) : \mathbb{R} \rightarrow \mathbb{R}^3$ is written as a tensor product

$$\mathbf{S}(u, v) = \sum_{i=1}^n \sum_{j=1}^m N_{i,p}(u) N_{j,q}(v) \mathbf{P}_{i,j}; \quad a \leq u, v \leq b. \quad (4.6)$$

The polynomial function assigned to a control point $\mathbf{P}_{i,j}$ is constructed as the product of basis functions defined in each parametrical direction. Basis function can take a different polynomial degree p or q depending on the parametrical direction to which they belong. The basis functions are now defined along the knot vectors

$$\begin{aligned} \mathbf{U} &= \underbrace{\{a, \dots, a\}}_{p+1}, u_{p+2}, \dots, u_i, \dots, u_{r-p-1}, \underbrace{\{b, \dots, b\}}_{p+1} \\ \mathbf{V} &= \underbrace{\{a, \dots, a\}}_{q+1}, u_{q+2}, \dots, u_i, \dots, u_{s-q-1}, \underbrace{\{b, \dots, b\}}_{q+1}. \end{aligned} \quad (4.7)$$

The range and boundary of the parametrical domain $[a, b]$ can take distinct values depending on each parametrical direction. For the sake of simplification the same interval is assigned to both parametrical directions, and it is usually normalized to $[0, 1]$.

4.3.2.1 Basis Functions

The standard method for computing B-spline basis functions $N_{i,p}(u)$ along a predefined knot vector \mathbf{U} is using the numerical stable Cox-de Boor recurrence formula [dB78],

$$\begin{aligned} N_{i,0}(u) &= \begin{cases} 1 & \text{if } u_i \leq u < u_{i+1} \\ 0 & \text{otherwise} \end{cases} \\ N_{i,p}(u) &= \frac{u - u_i}{u_{i+p} - u_i} N_{i,p-1}(u) + \frac{u_{i+p+1} - u}{u_{i+p+1} - u_{i+1}} N_{i+1,p-1}(u). \end{aligned} \quad (4.8)$$

Figure 4.3 shows the first two B-spline basis functions of polynomial degrees 0, 1, 2 and 3 for a uniform knot vector containing equal intervals of size 1. It can be observed that a basis function of polynomial degree p affects the curve over $p + 1$ knot spans.

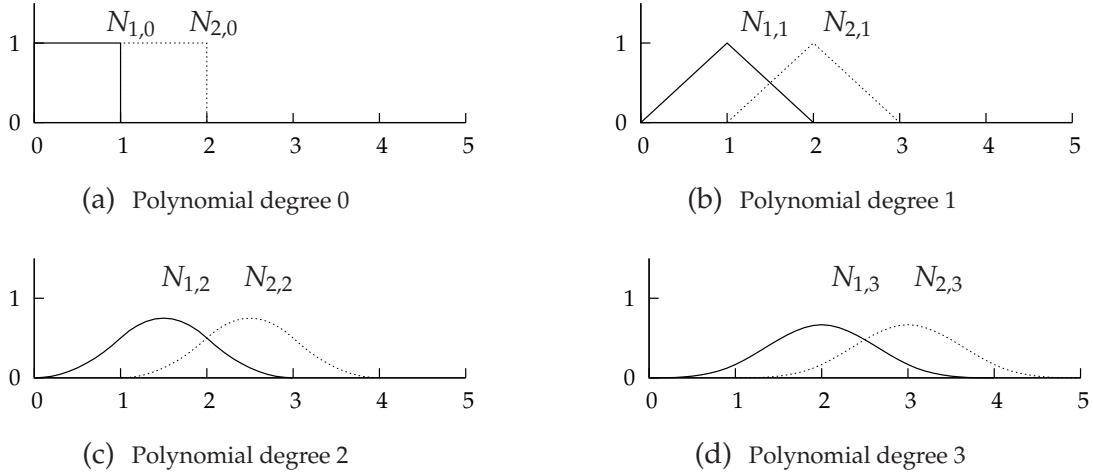


Figure 4.3: B-spline basis functions $N_{i,p}(u)$ of polynomial degree $p = 0, 1, 2$ and 3 .

The nonnegativity and partition of unity properties ($\sum_{i=1}^n N_{i,p}(u^*) = 1$ for a fixed u^*) of the basis functions, make them suitable to be used in FE-formulations ([HCB05]).

The B-splines denomination stand for Basis splines, since the functions $N_{i,p}(u)$ form a basis for the vector space of all piecewise polynomial functions of a certain degree and continuity along the parametric interval $a \leq u \leq b$ [Far02].

4.3.2.2 Knot Vector

The fixed parametric values u_i of the knot vector \mathbf{U} are called knot values or simply knots. They delimit knot spans $[u_i, u_{i+1})$ on which a certain number of basis function are defined to be different from zero. For example, the basis function $N_{i,p}(u)$ is valid only in the interval $[u_i, u_{i+p+1})$. This property of B-splines is one of the most relevant in shape modification, since it provides a local control over the curve. Thus, when the coordinates of the control point P_i related to the function $N_{i,p}(u)$ is altered, only the section of the curve $[u_i, u_{i+p+1})$ is influenced. For surface and solid representations in a two- and three dimensional space, the affected section is extended to an area and a volume respectively. From this very important property of B-splines, it can be noticed that the polynomial degree also affects the local control in the related parametrical direction.

Knots might take arbitrary real values along the the interval $[a, b]$ with the condition that the subsequent knot should never be smaller that the current one ($u_{i+1} \geq u_i$). In case that all knot spans have the same parametric distance, the knot is said to be uniform as it is shown in figure 4.3 for all examples. Knot spans can also be different in size, so that control points affect larger or smaller regions of the geometry. The knot vector is thus named as nonuniform. When fitting a B-Spline entity to existing data, knots have to take values according to the data-distribution, resulting usually in nonuniform distributions (see section 4.4). The related basis functions undergo modifications that differ from standard shapes (4.3). As an example of nonuniform knot vector, figure 4.4 shows B-spline basis functions of polynomial degree 2 defined by a typically open knot vector (also called nonperiodic or clamped) along the interval $[0, 1]$, where inner knot spans are uniform. First and last basis functions have the value equal to one at the beginning and end of the interval $[0, 1]$, meaning that first and last control points are interpolated and have therefore total influence on the curve at those locations. The higher the value of the function, the higher the influence of the corresponding control point on the shape at an arbitrary location u^* .

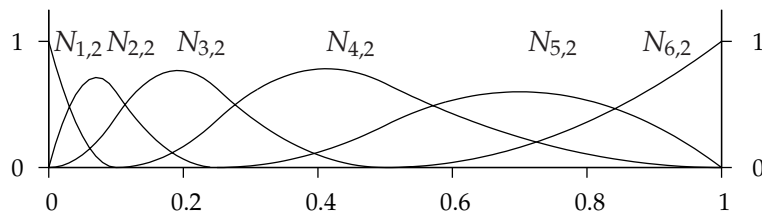


Figure 4.4: Basis functions of polynomial degree 2, $\mathbf{U} = \{0, 0, 0, 0.1, 0.3, 0.5, 1, 1, 1\}$.

4.3.3 Continuity Conditions

When combining several patches $\mathbf{S}^k(u, v)$ of a free form surface in order to cover an extended region, usually only C^0 continuity is assured between adjacent boundaries when

Cartesian coordinates of common control points coincide. This is the case of surface representations that contain a limited number of control points restricted by the desired polynomial order. In order to supply higher order of continuity, the number of control points of adjacent patches that have to satisfy certain mathematical conditions increases. For instance reference [Sch95] explains the different relations that adjacent control points of different patches have to fulfill in order to reach C^2 continuity for bicubic Bézier patches.

B-splines do not have the limitation in the number of control points by preserving the same polynomial degree. The number of CP might be increased by adding knots without affecting the geometrical shape, due to the piecewise property of the basis functions. The continuity of the basis functions and consequently of the geometrical representation, is modified by the multiplicity of the knots. At a knot value of multiplicity k , the curve (or surface in the corresponding parametric direction) is C^{p-k} continuous. In the interior of knot spans the geometrical representation remains C^{p-1} continuous.

Figure 4.5 shows how the continuity of a surface is affected by increasing the multiplicity of a knot. Figure 4.5(a) contains a surface representation, which uses the basis functions given in figure 4.4 for both parametrical directions u and v . The control point network was chosen to be regular. Figure 4.5(b) contains exactly the same surface, but now the basis functions in both parametrical direction are taken from figure 4.7. This new set of basis functions was obtained by increasing by one the multiplicity of the knot equal to 0.5 in both knot vectors \mathbf{U} and \mathbf{V} . The continuity of function $N_{5,2}$ in each knot vector was also decreased by one at 0.5 (see figure 4.7). The consequence is that the new generated control point at the intersection of the parameters 0.5 interpolates the surface. The surface now poses a discontinuity at the parameter 0.5 in both parametrical directions, dividing the surface into four C^1 continuous sections. This fact can be observed by modifying two control points of two different sections of the surface as shown in figures 4.5(c) and 4.5(d).

4.3.4 NURBS

A general rational B-spline surface (Non-Uniform Rational B-Spline, NURBS) is given by

$$\mathbf{S}(u, v) = \frac{\sum_{i=1}^n \sum_{j=1}^m N_{i,p}(u) N_{j,q}(v) w_{i,j} \mathbf{P}_{i,j}}{\sum_{i=1}^n \sum_{j=1}^m N_{i,p}(u) N_{j,q}(v) w_{i,j}}; \quad a \leq u, v \leq b; \quad w_{i,j} > 0. \quad (4.9)$$

Rational basis functions $R_{i,j}(u, v)$ are computed using B-splines basis functions, and are defined along the same knot vectors of equation (4.7). The expression of rational basis functions is

$$R_{i,j}(u, v) = \frac{N_{i,p}(u) N_{j,q}(v) w_{i,j}}{\sum_{k=1}^n \sum_{l=1}^m N_{k,p}(u) N_{l,q}(v) w_{k,l}}. \quad (4.10)$$

The extra scalar values $w_{i,j}$ are known as the weights of the control points.

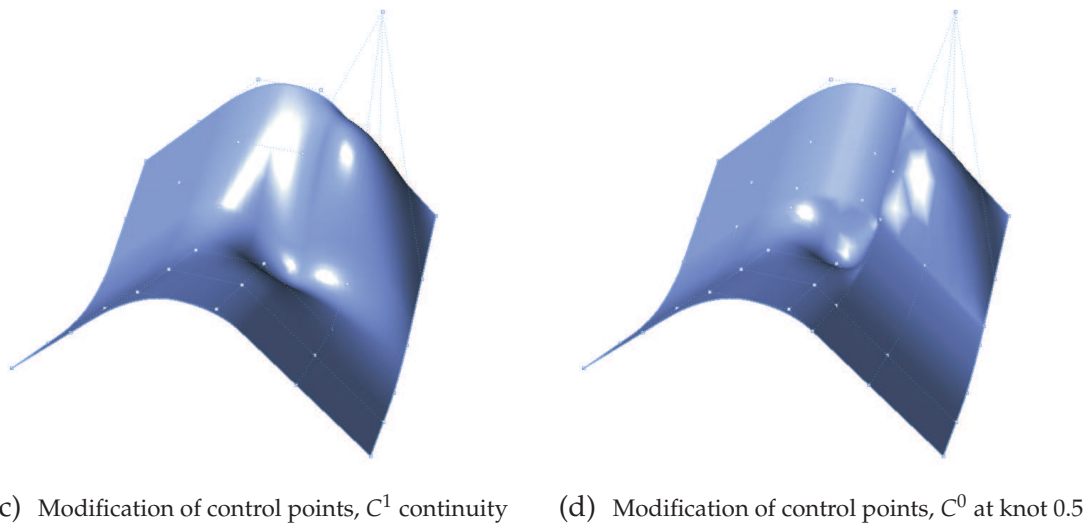
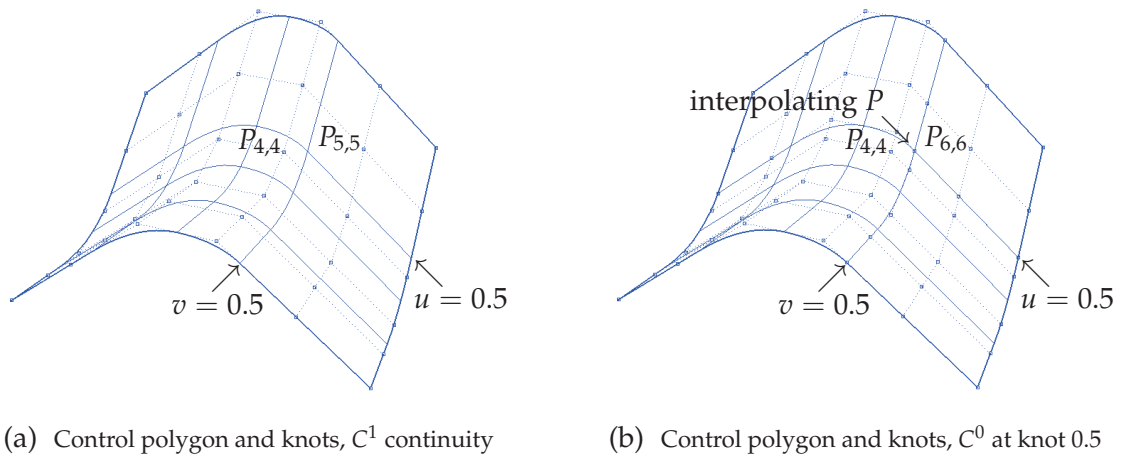


Figure 4.5: Decreasing continuity by increasing knot multiplicity.

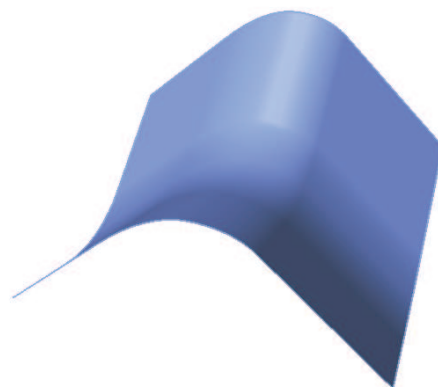


Figure 4.6: Rendered surface for unaltered knot vector

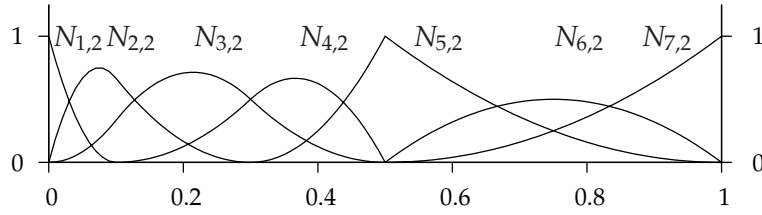


Figure 4.7: Basis functions of polynomial degree 2, $\mathbf{U} = \{0, 0, 0, 0.1, 0.3, 0.5, 0.5, 1, 1, 1\}$.

Every rational function has the same polynomial

$$W(u, v) = \sum_{i=1}^n \sum_{j=1}^m N_{i,p}(u) N_{j,q}(v) w_{i,j} \quad (4.11)$$

as denominator, whose evaluation at fixed parameters u^* and v^* gives the equivalent weight for the selected position. The equivalent weight depends on the distribution of the B-spline basis functions¹.

4.3.4.1 Homogeneous Representation

Since weights are mathematically considered as the fourth dimension of the control point, a rational B-spline surface can be also represented in *homogeneous coordinates*, whose formulation is similar to the tensor product of nonrational B-splines in equation (4.6),

$$\mathbf{S}^w(u, v) = \sum_{i=1}^n \sum_{j=1}^m N_{i,p}(u) N_{j,q}(v) \mathbf{P}_{i,j}^w; \quad a \leq u, v \leq b. \quad (4.12)$$

The components of the 4-dimensional control points $\mathbf{P}_{i,j}^w$ are defined as,

$$\mathbf{P}_{i,j}^w = \{xw, yw, zw, w\}. \quad (4.13)$$

As it can be deduced from equation (4.13), control points $\mathbf{P}_{i,j}$ in Cartesian coordinates are obtained by dividing the first three components of $\mathbf{P}_{i,j}^w$ by the fourth coordinate, w . In the same way, a fixed point on the surface $\mathbf{S}^w(u^*, v^*)$ is transformed into the three-dimensional Euclidean space by dividing its first three components by the fourth coordinate, its equivalent weight $W(u^*, v^*)$ (see equation 4.11).

Usually the homogeneous representation of NURBS is chosen for implementation purposes, since it is more efficient in terms of simplicity and data storage.

¹Same principle when computing the Cartesian coordinates in a nonrational B-spline as a contribution of every control point of the control point network (equation 4.6)

4.3.4.2 Weights

Weights supply additional control over the shape of the geometrical representation, and are essential for describing conics. The following references review conics sections and their representation using rational B-splines: [Far92], [BS96], [PT97] and [CRE01].

Figure 4.8 shows how a NURBS surface is modified by changing the value of different weights. The surface has a control network of 5×5 control points which are regularly distributed in the xy -plane, and uses an open knot vector with uniformly distributed interior knots for both parametrical directions, $\mathbf{U} = \mathbf{V} = \{0, 0, 0, 0.333, 0.667, 1, 1, 1\}$. The polynomial degree is equal to two in both directions. As shown in figure 4.8(b), the surface was divided into 14 equal spaces in the parametrical direction (a small distortion of regularity in element size in the Euclidean space is due to the arrangement of the control points). Basically when a weight is modified, the surface is pulled towards the related control point if the weight is increased, and it is pushed away from the control point if the weight gets closer to zero (negatives weights produce discontinuities and unexpected shapes). These effects influence the basis functions and act over every point of the parametrical space included in the region $[u_i, u_{i+p+1}) \times [v_j, v_{j+q+1})$. The elements of figure 4.8(b) are then deformed due to pulling or pushing as previously explained. Furthermore, the surface is always contained within the convex hull defined by the control points when $w_{i,j} > 0$.

It is important to notice that when all weights $w_{i,j}$ are equal to one a rational representation becomes nonrational. A B-spline representation where the knot vector does not include interior knots (for instance $U = \{0, 0, 0, 0, 1, 1, 1, 1\}$ for a polynomial degree equal to three), is equivalent to a nonrational Bézier representation.

The following list identifies the general advantages of rational B-splines.

- ◇ NURBS are a generalization of Bézier entities and B-Splines.
- ◇ They present a high flexibility for modeling any surface.
- ◇ The non-rational property allows the description of conic sections (circular and parabolic sections like circles, cylinders, spherical sections, etc.).
- ◇ The presence of weights at each control point gives more freedom for design and optimization.
- ◇ Allows the inclusion of many control points while the polynomial degree remains unchanged.
- ◇ Local control of geometry. The modification of coordinates or weight of a control point, modifies the geometry only over a restricted region.
- ◇ One patch can be used to model a broad area in detail avoiding continuity problems, in case of using more restricted representations.

- ◇ The polynomial approximation is independent between parametric directions, allowing a lower degree of representation in directions where otherwise higher degrees are useless.
- ◇ It has become a standard representation of geometry for data exchange in industries.

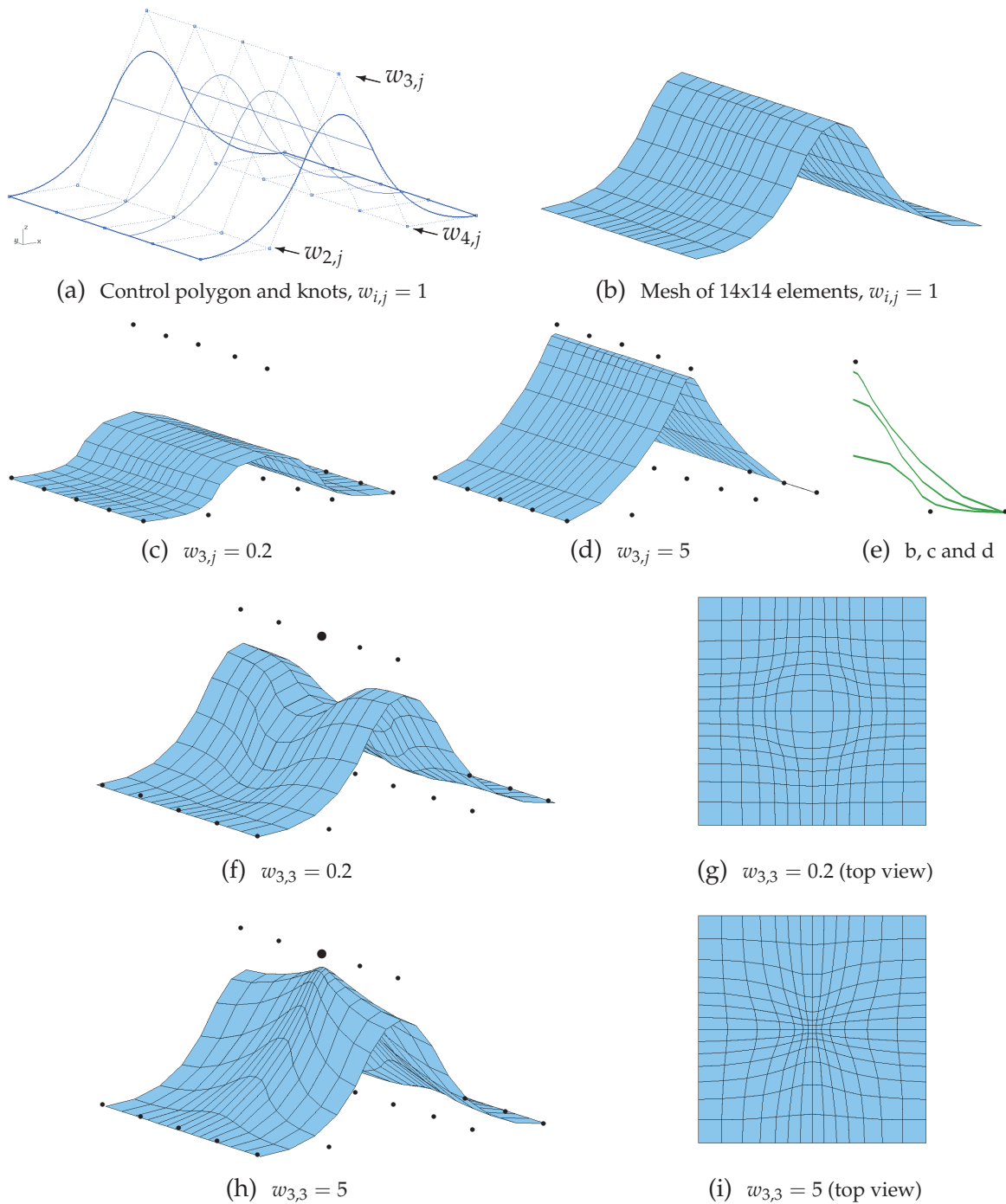


Figure 4.8: Modification in shape by modification of weights.

4.4 Surface Fitting - Surface Construction

The problem of generating smooth surfaces from scattered data can be found in several fields of applications. Reverse engineering for instance uses geometrical coordinates measured from real objects to construct mathematical models that can be studied later using adequate simulations. Geometrical values resulting from numerical solutions are used as scattered data as well for the generation of geometrical models, as it is the case of the examples analysed along this work.

Surface fitting methods appear as the suitable alternative to generate a free form surface from the equilibrium shape found by means of form finding (see figure 1.1). The geometry of the resulting surface is described by nodal coordinates, the free parameters in form finding. All or some of these nodes might be selected to be interpolated or approximated towards surface construction.

When the given scattered data is gridded-distributed, arranged in columns and rows of points, the problem is conveniently directed to a bidirectional curve fitting. First, the data along every column is fit to generate a family of curves. Finally, the computed control points of these curves are fit row-wise so that the new computed control points become the ones for the final surface [PT97]. The parameters associated to each data point needed in surface fitting have a fundamental influence in the quality of the approximated entity. In curve fitting the usual methodologies to compute them are the uniform, chord length and centripetal parameterization [MK95] (more details in section 4.4.1).

In case the number of data points between columns differs from each other, surface skinning would be a better alternative. Skinning is one of the most widely used tools for shape design when cross sectional curves are the source of information to perform fitting [Tok00]. This method consists basically on taking a family of curves, making them compatible, which means that all of them should have the same polynomial degree p and knot vector U , and fitting control points across them. The same principle can be applied to fit a cloud of points distributed in a column-wise manner. After fitting curves along columns of data, the classical skinning method makes these curves compatible by merging all knot vectors into a common one so that a second sequence of curve fitting is done along the previously generated control points [Woo88], [PT97]. Nevertheless, two problems arise when using the classic skinning method. The first one is the well known explosion of control points due to the merging of the resulting knot vectors. The second problem arises when using NURBS for the fitting process, where weights are also considered as variables. The first problem is solved by the authors in [PT02], [PT00d] and [PT00c] by passing a pre-defined knot vector U for the compatibility process. The merged knot values have the highest priority to be considered in the first fitting sequence. In reference [SAS06] the technique of knot removal is employed to reduce the number of knots from the merged knot vector which is then used in the compatibility operation. The second problem is avoided by some authors like Piegl and Tiller [PT02] who keep the solution of the problem in three-dimensions and consider only B-spline fitting, giving up the fourth free parameter. A good parameterization of the data

becomes more important. Other authors make sure that the resulting weights are greater than zero, as in reference [MK98], where a two step linear approach for NURBS fitting is presented. The method solves first for the weights applying eigenvalue decomposition techniques to avoid negative weights, and subsequently the position of the control points is calculated.

There are also more general approaches to fit unstructured distribution of scattered data. The effort of these methods focuses on finding a good parameterization for the given data. Hormann for instance, proposes in [Hor00] a variational approach. In [Hor03] the same author presents a three step indirect approach consisting on triangulation, remeshing and surface fitting, where after a global parameterization of the unstructured data the remeshing step is performed in the parametrical space to reorganize the distribution of data into a regular structured mesh ([HG00]) so that for instance a B-spline surface fitting could be applied afterwards. A similar approach is presented in reference [SF00]. Ma and Kruth propose in [MK95] a method that improves B-spline fitting of randomly distributed data by re-computing parameters using a predefined base surface where the measured points are projected.

Within the scope of this work, global B-spline surface approximation of scattered data is employed for fitting nodal information. Data-parameters are computed adopting the idea of using a base surface [MK95]. The base surface is constructed by means of bilinear curve interpolation, where only a portion of the data is selected. The selected data should represent the particular shape. The degree of approximation of the fitted surface will depend on basically two aspects:

- ◇ The different methods involved in the fitting process: parameter calculation of data, computation of suitable knot vectors, and how the final system of equation is set in order to find the geometric coefficients where some constraints could be additionally considered.
- ◇ The number of geometric coefficients that are to be found at the end of the fitting process. Again, the number of control points is obtained from a compromise between the freedom of the geometrical model to generate different shapes and a suitable number of optimization variables to avoid numerical drawbacks.

The following sections explain the sequence of methods included in the surface fitting approach employed in the following examples: parameterization of data, knot vector computation, global interpolation and approximation. Afterwards, knot removal and knot insertion are presented as an alternative to modify the number of geometrical coefficients in the geometrical model for shape optimization.

4.4.1 Parameterization of data

Each data point Q_k ($k = 1, \dots, d$) is assigned a parameter value \bar{u}_k , which indicates its position in the parametrical domain and therefore of high importance for fitting purposes. That

means the location in the three dimensional space of each Q_k is now approximated through the curve formulation $C(\bar{u}_k)$ by having an accurate enough value for the parameter \bar{u}_k . As a consequence, the performance of the generated surface will depend on the quality of the parameterization. The most used parameterization in B-spline curve and surface fitting of gridded data are the uniform, chord length and centripetal methods [SAS06], [PT00a]. The first method computes equally spaced parameters, while the last two methods take into consideration the distribution of the data along the fitting direction. The chord length method is given by the following formulation when the parameters are contained in the interval $[0, 1]$ [PT97]

$$\begin{aligned} \bar{u}_1 &= 0; \quad \bar{u}_d = 1; \quad D = \sum_{k=2}^d |Q_k - Q_{k-1}| \\ \bar{u}_k &= \bar{u}_{k-1} + \frac{|Q_k - Q_{k-1}|}{D}; \quad k = 2, \dots, d-1, \end{aligned} \quad (4.14)$$

where D is the total straight distance between data. The centripetal method computes parameters as [Lee89]

$$\begin{aligned} \bar{u}_1 &= 0; \quad \bar{u}_d = 1; \quad D = \sum_{k=2}^d \sqrt{|Q_k - Q_{k-1}|} \\ \bar{u}_k &= \bar{u}_{k-1} + \frac{\sqrt{|Q_k - Q_{k-1}|}}{D}; \quad k = 2, \dots, d-1, \end{aligned} \quad (4.15)$$

In case of surface fitting, the surface parameters are computed by projecting the data onto a base surface (see figure 4.9). The corresponding parametrical point (\bar{u}_k, \bar{v}_k) is computed by solving an unconstrained minimization problem where the objective function $f(u, v)$ is given by the distance between the current data Q_k and the related point to be found on the surface $S(u, v)$ [Sch95],

$$\text{Min} : \quad f(u, v) = \frac{1}{2} |\mathbf{S}(u, v) - \mathbf{Q}_k|^2 \quad (4.16)$$

The minimum of the function f is obtained by taking its partial derivatives w. r. t the free parameters u^* and v^* and making these expressions equal to zero.

$$\begin{aligned} f(u, v)_{,u} &= (\mathbf{S}(u, v) - \mathbf{Q}_k) \cdot \mathbf{S}(u, v)_{,u} = 0 \\ f(u, v)_{,v} &= (\mathbf{S}(u, v) - \mathbf{Q}_k) \cdot \mathbf{S}(u, v)_{,v} = 0 \end{aligned} \quad (4.17)$$

The previous nonlinear partial differential equations are linearized by considering until the first derivative term of their Taylor expansion (equation 2.30), so that the linear system of equation with two unknowns can be solved at each iteration step using for instance the common Newton-Raphson method

$$\mathbf{A}^n(u, v) \Delta^n = \mathbf{b}^n(u, v), \quad (4.18)$$

where the matrix \mathbf{A} is the Hessian or Jacobian matrix of f ,

$$A_{\alpha\beta}^n(u, v) = \mathbf{S}(u^n, v^n)_{,\alpha\beta} \cdot (\mathbf{S}(u^n, v^n) - \mathbf{Q}_k) + \mathbf{S}(u^n, v^n)_{,\alpha} \cdot \mathbf{S}(u^n, v^n)_{,\beta}. \quad (4.19)$$

Vector \mathbf{b} and the incremental vector Δ are given by

$$\mathbf{b}^n(u, v) = \begin{bmatrix} -f(u^n, v^n)_{,u} \\ -f(u^n, v^n)_{,v} \end{bmatrix}; \quad \Delta^n = \begin{bmatrix} \Delta u \\ \Delta v \end{bmatrix}. \quad (4.20)$$

The value of the parameters for the next iteration step are then computed as $u^{n+1} = u^n + \Delta u$ and $v^{n+1} = v^n + \Delta v$. The Newton-Raphson iteration is stopped after a certain convergence criteria is met [Sch95],

$$\left. \begin{array}{l} |\Delta u, \Delta v| \leq \varepsilon_1 \\ |\mathbf{S}(u^n, v^n) - \mathbf{Q}_k| \leq \varepsilon_2 l_a \end{array} \right\} = (\bar{u}_k, \bar{v}_k), \quad (4.21)$$

where l_a is a measure for the size of the surface that averages the longest distance between control points in each Cartesian coordinate

$$l_a = \sqrt{(\max(x) - \min(x))^2 + (\max(y) - \min(y))^2 + (\max(z) - \min(z))^2}. \quad (4.22)$$

The second tolerance ε_2 in equation (4.21) controls how far the current point on the surface $\mathbf{S}(u^n, v^n)$ is separated from the data \mathbf{Q}_k . In case a control point is to be projected on the surface using the same technique, ε_2 has to be relaxed.

Since the initial value of the parameters for the iteration procedure is crucial for convergence to the right solution, it should be ensured that it is set close enough to the current data point. Particularly in case of highly oscillating shapes the optimum of equation (4.16) could be caught in a wrong valley. This problem can be controlled by dividing knot spans into i equally spaces and using this new computed parameters (sub-knots) to compute points on the surface [PT97]. Afterwards, distances are computed from these points to the current node. The pair of parameters that gives the minimal distance to the current nodal value are finally used as starting parameters for the Newton-Raphson iteration.

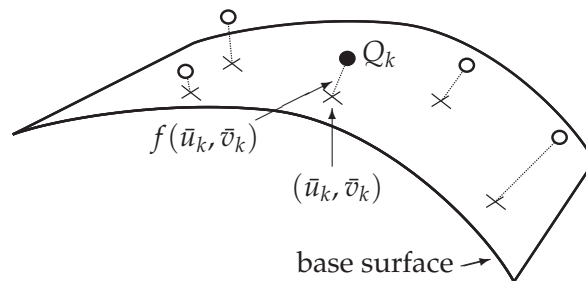


Figure 4.9: Data projection on base surface.

4.4.2 Knot vector

In order to calculate the set of basis functions needed in the fitting process it is necessary to have a suitable knot vector besides the selection of a polynomial degree. The knot vector plays an important role in the quality of the generated geometry as well as in the stability of the system of equations that has to be solved to get the location of the geometrical coefficients of the approximated surface. The fulfillment of the Schönberg-Whitney condition² for the knot vector [CRE01], ensures that the Matrix of basis functions, coefficients N for B-spline fitting (eqs. 4.27 and 4.32), is invertible, so that the system of equations to be solved has unique solution. The most common method to compute a suitable knot vector used for interpolation of gridded data is the technique of *averaging* suggested in [dB78], which gives good practical results [PT97], [Tok00]. As in equation (4.5) the first and the last $p + 1$ knots of an open knot vector take the value zero and one respectively,

$$u_1 = \dots = u_{p+1} = 0; \quad u_{r-p} = \dots = u_r = 1. \quad (4.23)$$

The rest of the $r - 2p - 2$ knots are computed as,

$$u_{j+p} = \frac{1}{p} \sum_{i=j}^{j+p-1} \bar{u}_i; \quad j = 2, \dots, n - p + 1. \quad (4.24)$$

For approximation to gridded data the authors in [PT00b] propose a generalization of the averaging technique whose solution gets closer to the knot obtained by averaging when the number of required control points approaches the number of data points. For details of the algorithm refer to the mentioned literature.

In general, for fitting purposes knot values have higher freedom to be selected compared to parameter values, so that they can be perturbed without causing numerical problems [PT00d]. Nevertheless they also have influence in the final computed shape. One common technique to calculate knots is to compute equally spans for interior knots, leading to an open uniform knot vector:

$$\begin{aligned} u_1 = \dots = u_{p+1} = 0; \quad u_{r-p} = \dots = u_r = 1 \\ u_{i+p+1} = \frac{i}{n-p}; \quad i = 1, \dots, n-p. \end{aligned} \quad (4.25)$$

4.4.3 B-spline Global Interpolation

Given a set of data points \mathbf{Q}_k ($k = 1, \dots, d$), the problem is to find a set of control points \mathbf{P}_l ($l = 1, \dots, n'$), which belong to a curve (surface) of degree p (and q) having a knot vector \mathbf{U} (and \mathbf{V}) which interpolates every data point \mathbf{Q}_k with the point on the curve (surface) obtained by using the previously calculated parameters \bar{u}_k . The system of equations to be

²specifies a minimum number of parameters between two consecutive knots

solved is given by

$$\sum_{l=1}^{n'} N_l(\bar{u}_k) \mathbf{P}_l = \mathbf{Q}_k; \quad k = 1, \dots, d; \quad n' = d. \quad (4.26)$$

For curves, the basis functions are $N_l = N_{i,p}(\bar{u}_k)$. For surfaces $N_l = N_{i,p}(\bar{u}_k) N_{j,q}(\bar{v}_k)$. Equation (4.26) is written in matrix notation as $\mathbf{N} \cdot \mathbf{P} = \mathbf{Q}$,

$$\begin{bmatrix} N_1(\bar{u}_1) & \cdots & N_{n'}(\bar{u}_1) \\ \vdots & \ddots & \vdots \\ N_1(\bar{u}_d) & \cdots & N_{n'}(\bar{u}_d) \end{bmatrix}_{[n' \times n']} \cdot \begin{bmatrix} \mathbf{P}_1 \\ \vdots \\ \mathbf{P}_{n'} \end{bmatrix}_{[n' \times 1]} = \begin{bmatrix} \mathbf{Q}_1 \\ \vdots \\ \mathbf{Q}_d \end{bmatrix}_{[n' \times 1]}; \quad n' = d. \quad (4.27)$$

The value of n' is equal to n or $n \cdot m$ for curves or surfaces respectively.

Additional constraints which can be added to this formulation are found for instance in [PT97], [PT00a].

4.4.4 B-spline Global Approximation

The problem of approximating a curve (surface) to a set of nodal data arises when the number of data is strictly larger than the number of geometrical coefficients ($d > n'$). The solution in this case is not directly found as in the case of data interpolation, since there are now more equations than unknowns. The least-squares technique [dB78] is the usual answer to the question of how to find the geometrical representation that approximate the given data set \mathbf{Q}_k ($k = 1, \dots, d$). Thus, the geometrical coefficients \mathbf{P}_l ($l = 1, \dots, n'$) are found by solving the unconstrained minimization problem

$$\text{Min} : \quad f(\mathbf{P}_l) = \left| \mathbf{Q}_k - \sum_{l=1}^{n'} N_l(\bar{u}_k) \mathbf{P}_l \right|^2; \quad k = 1, \dots, d. \quad (4.28)$$

For a better mathematical manipulation, the previous function f can be also written as

$$f = \left(\mathbf{Q}_k - \sum_{l=1}^{n'} N_l(\bar{u}_k) \mathbf{P}_l \right) \left(\mathbf{Q}_k - \sum_{l=1}^{n'} N_l(\bar{u}_k) \mathbf{P}_l \right); \quad k = 1, \dots, d. \quad (4.29)$$

The solution of equation (4.28) is obtained by taking partial derivatives of f with respect to the unknown geometrical coefficients \mathbf{P}_l and making these results equal to zero

$$\frac{\partial f}{\partial \mathbf{P}_a} = 2 \left(\mathbf{Q}_k - \sum_{l=1}^{n'} N_l(\bar{u}_k) \mathbf{P}_l \right) N_a(\bar{u}_k) = \mathbf{0}; \quad k = 1, \dots, d; \quad a = 1, \dots, n'. \quad (4.30)$$

After reordering terms, the system of equation is written as

$$\sum_{l=1}^{n'} N_l(\bar{u}_k) N_a(\bar{u}_k) \mathbf{P}_l = N_a(\bar{u}_k) \mathbf{Q}_k; \quad k = 1, \dots, d; \quad a = 1, \dots, n' \quad \text{or} \quad (4.31)$$

$$\sum_{k=1}^d \left(\sum_{l=1}^{n'} N_l(\bar{u}_k) \sum_{a=1}^{n'} N_a(\bar{u}_k) \mathbf{P}_l = \sum_{a=1}^{n'} N_a(\bar{u}_k) \mathbf{Q}_k \right)$$

and in matrix form $(\mathbf{N}^T \cdot \mathbf{N}) \cdot \mathbf{P} = \mathbf{N}^T \cdot \mathbf{Q}$,

$$\left(\begin{bmatrix} N_1(\bar{u}_1) & \cdots & N_1(\bar{u}_d) \\ \vdots & \ddots & \vdots \\ N_{n'}(\bar{u}_1) & \cdots & N_{n'}(\bar{u}_d) \end{bmatrix} \cdot \begin{bmatrix} N_1(\bar{u}_1) & \cdots & N_{n'}(\bar{u}_1) \\ \vdots & \ddots & \vdots \\ N_1(\bar{u}_d) & \cdots & N_{n'}(\bar{u}_d) \end{bmatrix} \right)_{[n' \times n']} \cdot \begin{bmatrix} \mathbf{P}_1 \\ \vdots \\ \mathbf{P}_{n'} \end{bmatrix}_{[n' \times 1]} =$$

$$\left(\begin{bmatrix} N_1(\bar{u}_1) & \cdots & N_1(\bar{u}_d) \\ \vdots & \ddots & \vdots \\ N_{n'}(\bar{u}_1) & \cdots & N_{n'}(\bar{u}_d) \end{bmatrix} \cdot \begin{bmatrix} \mathbf{Q}_1 \\ \vdots \\ \mathbf{Q}_d \end{bmatrix} \right)_{[n' \times 1]} \quad (4.32)$$

As for the case of global interpolation, n' is equal to n for curves and $n \cdot m$ for surfaces.

Additional constraints to the formulation are found for instance in [PT97], [PT00b]. In case it is needed that some data points interpolate the fitted surface, the method might be improved considering additional interpolating equations where only constrained data are involved. In this way, the unknowns coefficients $\mathbf{P}_{i,j}$ are found by solving a constrained minimization problem as explained in [PT97] for weighted and constrained least squares curve fitting. Reference [Yan05] presents some numerical algorithms for estimating least squares problems.

4.4.5 Surface Fitting Examples

Figure 4.10 shows an example of surface fitting. It considers a highly oscillating shape in y direction, in order to check the performance of the algorithm. The FE-mesh represents the equilibrium shape of a pressurized bulkhead obtained by means of form finding, when applying an isotropic pre-stress state ($\sigma = \bar{\sigma} \mathbf{I}$) together with pressure load equal to two percent of the in-plane pre-stress ($p = 0.02\bar{\sigma}$). It is the same equilibrium configuration shown in figure 3.4(b) for concept C. Figures 4.11(a) and 4.11(b) show the construction of two different base surfaces obtained by bilinear curve interpolation. A number of 3×15 and 5×22 nodes respectively were selected from the mesh towards base surface construction. The rather regular nodal distribution facilitated a gridded selection of data for bilinear interpolation. Parametric data was computed using the chord length method and knot vectors using the averaging approach. Figures 4.12(a) and 4.12(b) contain final fitted surfaces achieved with the previously described base surfaces. Knot vectors of approximated surfaces were calculated as open uniform vectors. For each approximation it is indicated

the number of control points (CP) together with the relative error with respect to the nodal data of the FE-mesh. The mean error stands for the sum of all nodal errors divided by the total number of nodes ($\sum_{i=1}^{nnodes} \frac{error_i}{nnodes}$), while the maximum error represents the maximum nodal deviation from the final fitted surface. It can be observed that the selection of the base surface influences the quality of the final approximated surface. Another observation from these results is that the closer the number of geometrical coefficients of the base surface to the number of coefficients of the final surface, the better the quality of the approximation.

The maximum error of the approximated surfaces is due to the sharp geometrical change at some regions.

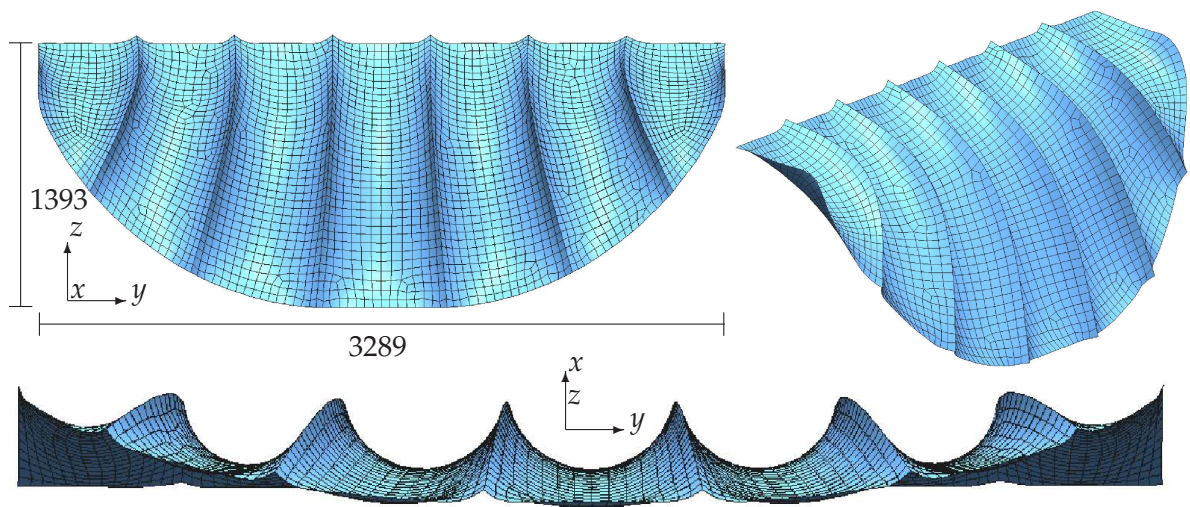
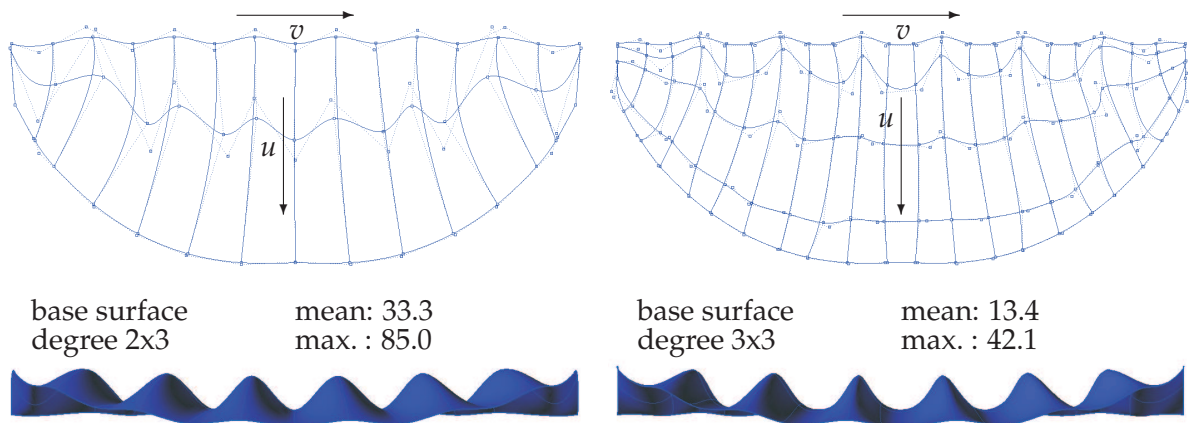


Figure 4.10: FE-mesh of a pressurized bulkhead, 3148 nodes. Units in [mm].



(a) Bilinear curve interpolation of 3x15 CP

(b) Bilinear curve interpolation of 5x22 CP

Figure 4.11: Base surfaces to approximate FE-mesh of figure 4.10. Units in [mm].

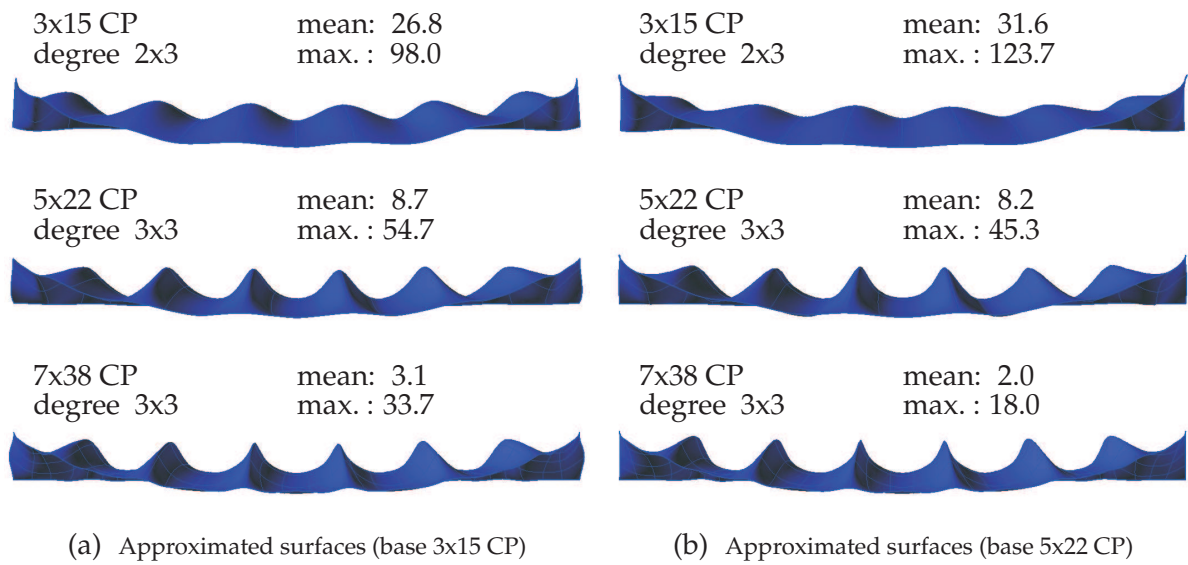


Figure 4.12: Approximated surfaces of example in fig. 4.10. Units in $[mm]$.

The next example shown in figure 4.13 contains an unstructured free FE-mesh created over one of the fitted surfaces of the previous example. It corresponds to the surface with a network of 7x38 CP drawn in figure 4.12(b). This example shows the application of the method in case the FE-mesh is highly irregular. Due to this irregularity in nodal distribution, a gridded selection of data for the construction of the base surface might present some difficulties. This situation can be recognized in the irregularity of some of the cross-sectional curves in bilinear curve interpolation exposed in figure 4.14. Nevertheless, the method gives satisfactory results in computing both final and base surfaces. See generated geometries, and error measurements in figures 4.14 and 4.15.

Figures 4.16(a) and 4.16(b) give an idea of the distortion of the computed base and approximated surfaces of figures 4.14 and 4.15 concerning the parametrical domain due to the fitting algorithm. The parametrical domain was divided into equal spaces of 20x70 in u and v directions respectively. However, the particular shape of the example produces additional optical distortion.

The improved approximated surface of figure 4.15 was obtained by using as base surface the first approximated surface that appears in the same figure. In other words, the nodal parameters were re-computed using the first approximated surface. The slightly better accuracy of the improvement is observed when comparing the values of the standard deviation σ of the nodal values with respect to each approximated surface. The final result (accuracy of approximation) is practically the same in both cases, even though the difference between base surfaces is significant. This is a very important insight that will be very useful for the collection of supporting data in future surface fitting.

In order to construct any base surface, special care should be taken at the boundaries of the domain. Even though the parameters are always kept within the square domain during

the projection algorithm (section 4.4.1), the quality of the parameterization and consequently of the final surface will be affected in case the boundaries of the base surface compared to the boundaries of the cloud of data differ.

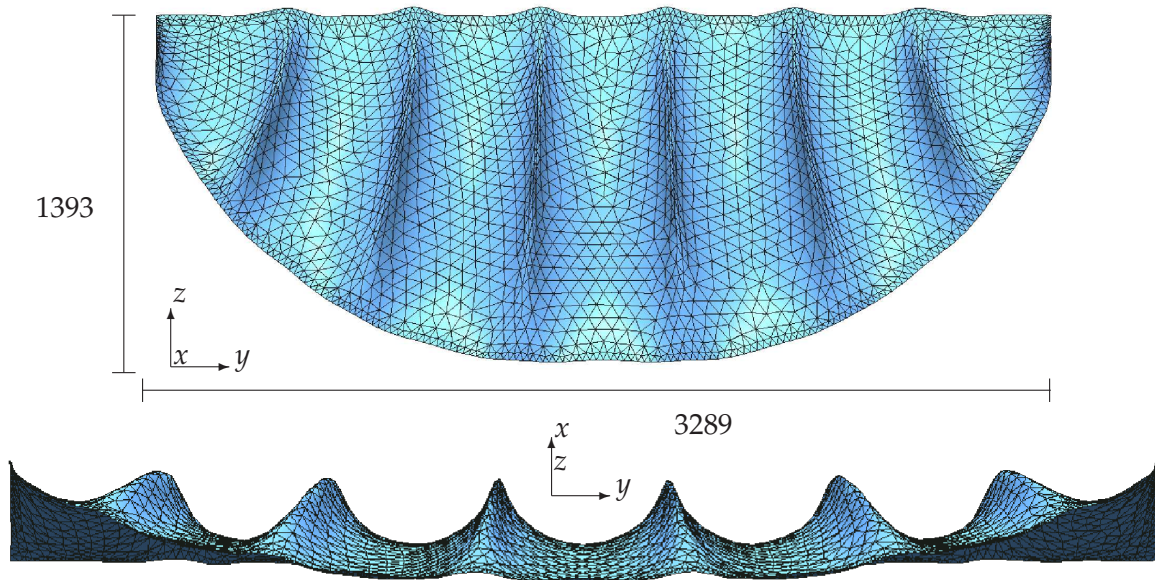


Figure 4.13: Free FE-mesh of 2309 nodes. Units in $[mm]$.

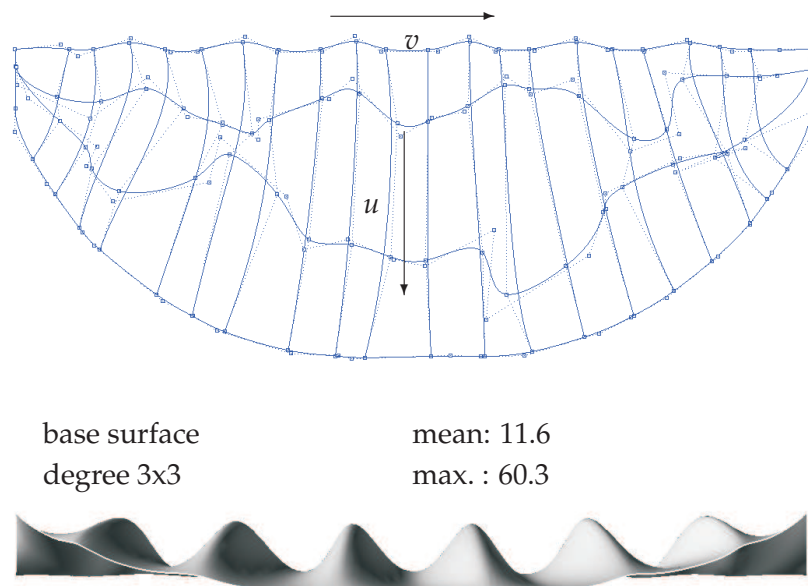


Figure 4.14: Base surface (4x22 CP) to approximate FE-mesh of figure 4.13. Units in $[mm]$.

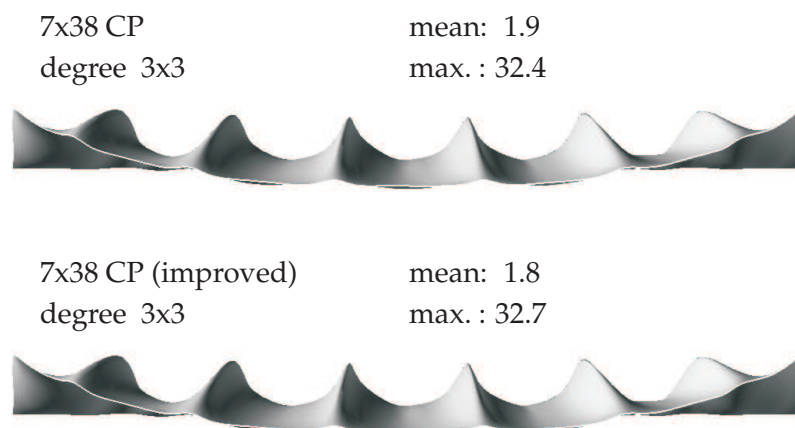
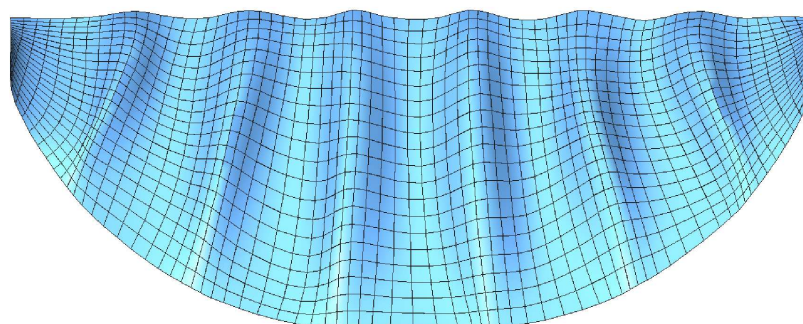
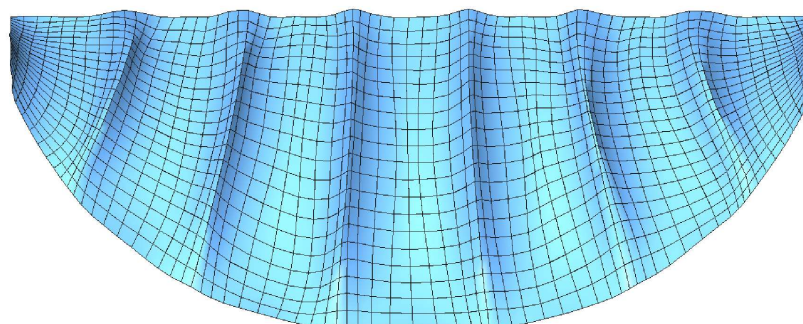


Figure 4.15: Approximated surfaces of example in fig. 4.13 (base 4x22 CP). Units in $[mm]$.

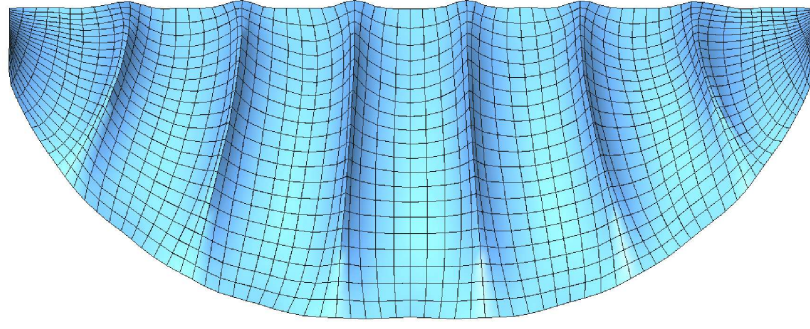


(a) Base surface of 4x22 CP from fig. 4.14



(b) Approximated surface of 7x38 CP from fig. 4.15

Figure 4.16: Girdded meshes. Parametric domain divided into 20x70 equal spaces.



(c) Approximated surface of 7x38 CP from fig. 4.12(b)

Figure 4.16: Girded meshes of approximated surfaces by dividing the parametrical domain into 20x70 equal spaces (cont).

4.4.6 Modification in the Number of Design Parameters

After the geometrical model is obtained by surface fitting approaches, it might be necessary to modify the number of design parameters $\mathbf{P}_{i,j}$. In this way, the number of design variables over certain regions of the surface could be increased or decreased, giving a higher or lower flexibility for shape control in the optimization process. This modification is possible when knots are added or removed from the initial knot vectors. The basic concept of knot insertion and removal are briefly described in the next subsections.

4.4.6.1 Knot Insertion

Knot insertion is basically adding a new knot \bar{u} into an existing knot vector \mathbf{U} without modifying the geometry or the parameterization of the analysed entity. It is just a change of vector space basis. The new knot can also have the value of an already existing knot. In this case the initial knot multiplicity s is increased by one. Since the number of control points is directly related to the number of knots, adding the knot \bar{u}_i t times increases the number of control points (and related B-spline functions) in t as well.

In case of working with curves, the system of equation to be solved is given by equating initial and final representations $C(u)^w = \bar{C}(u)^w$,

$$\sum_{i=1}^n N_{i,p}(u) \mathbf{P}_i^w = \sum_{i=1}^{n+t} \bar{N}_{i,p}(u) \bar{\mathbf{P}}_i^w, \quad (4.33)$$

where the final curve is defined over the knot vector $\bar{\mathbf{U}}$, which is equal to \mathbf{U} including now the new knot \bar{u}_i t times. However, not all control points of the new representation must be

computed.

Due to the piecewise property of B-splines, knot insertion (as well as knot removal) is a local operation that involves the neighborhood of the control points near the new added knot. Thus, the new control points that have to be computed in the t^{th} insertion step are given by [PT97]

$$\begin{aligned} \bar{\mathbf{P}}_{i,t}^w &= \alpha_{i,t} \bar{\mathbf{P}}_{i,t-1}^w + (1 - \alpha_{i,t}) \bar{\mathbf{P}}_{i-1,t-1}^w \\ \bar{\mathbf{P}}_{i,0}^w &= \mathbf{P}_i^w \\ \alpha_{i,t} &= \begin{cases} 1 & i \leq k - p + t - 1 \\ \frac{\bar{u} - u_i}{u_{i+p-t+1} - u_i} & k - p + t \leq i \leq k - s \\ 0 & i \geq k - s + 1 \end{cases} \end{aligned} \quad (4.34)$$

where k is the knot span of the inserted knot \bar{u} . $p - s - 1$ control points \mathbf{P} are replaced by $p - s + t - 1$ new control points $\bar{\mathbf{P}}$, where each new control point is computed from two old ones. Notice that even though the geometry does not change after knot insertion, the control polygon does. For surfaces, equation (4.34) has to be solved for each row and column of control points.

Besides increasing flexibility in shape control, knot insertion is also used to decrease continuity when increasing the multiplicity of a knot. If the inserted knot reaches multiplicity equal to the polynomial degree $s = p$ the entity is split as shown in figure 4.7.

Algorithms created for Knot refinement work basically as knot insertion does with the additional option that several knots can be inserted at once. Details regarding algorithms and their derivations can be found in [PT97] and [Lyc93].

As suggested by equation (4.34), new control points lie on the control polygon between two consecutive old ones. This fact leads to what is called inverse knot insertion [Pie89], where the knot \bar{u} to be inserted is calculated out of the position the new control point will take. This is, for $t = 1$:

$$\begin{aligned} \bar{u} &= u_i + \alpha(u_{i+p} - u_i) \\ \alpha &= \frac{w_{i-1} |\mathbf{P}_{i,1} - \mathbf{P}_{i-1,0}|}{w_{i-1} |\mathbf{P}_{i,1} - \mathbf{P}_{i-1,0}| + w_i |\mathbf{P}_{i,0} - \mathbf{P}_{i,1}|} \end{aligned} \quad (4.35)$$

Figure 4.17(a) shows the insertion of knot $\bar{v} = 0.3$ ($t = 1$) in the knot vector $\bar{\mathbf{V}}$ (corresponding to the parametrical direction v) of the surface shown in figure 4.5(a) by placing a line of control points along the parametrical direction u exactly between control points $\mathbf{P}_{(i,4),0}$ and $\mathbf{P}_{(i,5),0}$ ($\alpha = 0.5$). No control points are modified since the inserted knot had already multiplicity s equal to 1 and the polynomial degree p is equal to 2. Furthermore, the continuity of the surface is reduced from C^1 to C^0 along the parameter v equal to the inserted knot value.

4.4.6.2 Knot Removal

Knot removal deletes a knot \bar{u} from an existing knot vector \mathbf{U} . Since practically all interior knots could be removed from a knot vector, if no care is given to shape deviations, the modification of the initial geometry is usually restricted to a user defined tolerance. In this way, whether a knot can be removed producing important geometrical modifications or not is based on this tolerance that measures geometrical deviations on the entire parametrical domain. Generalizing to rational B-spline curves, the problem of finding a new representation $\bar{C}(u)^w$ of the initial curve $C(u)^w$ is solved by the following equation

$$\sum_{i=1}^n N_{i,p}(u) \mathbf{P}_i^w = \sum_{i=1}^{n-t} \bar{N}_{i,p}(u) \bar{\mathbf{P}}_i^w. \quad (4.36)$$

Every new geometrical coefficient does not need to be again calculated due to the local control property of B-splines as it is also the case for knot insertion. Thus, the reduced set of $p - s + 1$ equations containing $p - s$ unknown control points for each iteration t , is given by [PT97]:

$$\begin{aligned} \bar{\mathbf{P}}_{i,t}^w &= \frac{\bar{\mathbf{P}}_{i,t-1}^w - (1 - \alpha_{i,t}) \bar{\mathbf{P}}_{i-1,t}^w}{\alpha_{i,t}} & k - p - t + 1 \leq i \leq \frac{1}{2}(-p - s - t) + k \\ \bar{\mathbf{P}}_{j,t}^w &= \frac{\bar{\mathbf{P}}_{j,t-1}^w - \alpha_{j,t} \bar{\mathbf{P}}_{j+1,t}^w}{(1 - \alpha_{j,t})} & \frac{1}{2}(-p - s + t + 1) + k \leq j \leq k - s + t - 1 \\ \bar{\mathbf{P}}_{i,0}^w &= \mathbf{P}_i^w \\ \alpha_{i,t} &= \frac{\bar{u} - u_i}{u_{i+p+t} - u_i} & \alpha_{j,t} = \frac{\bar{u} - u_{j-t+1}}{u_{j+p+1} - u_{j-t+1}} \end{aligned} \quad (4.37)$$

$p - s + 1$ control points are replaced by $p - s$ new control points. k is the knot span index of the inserted knot \bar{u} .

The tolerance is used to either check the distance between two computed values of a new control point or the difference between an existing control point and its equivalent, resulting from the equation system (4.37). For details regarding the algorithm and its derivation refer to [PT97]. Other knot removal algorithms can be found for instance in [Lyc93].

Figure 4.17(b) shows the surface of figure 4.5(a), after removing all interior knots from both knot vectors without considering any restrictive tolerance. As said before, knot removal might involve geometrical changes which is not the case for knot insertion operations.

One of the advantages of using knot removal as already explained is that previously added knots, by using knot insertion, can be removed from a geometrical model without geometrical modifications. On the other hand, trying to decrease the number of control points from an approximated surface using knot removal could drastically deviate the geometry from the original one. A better solution could be to perform a new surface fitting using the new number of control points, since the complete geometry adjusts itself globally to approximate the given data.

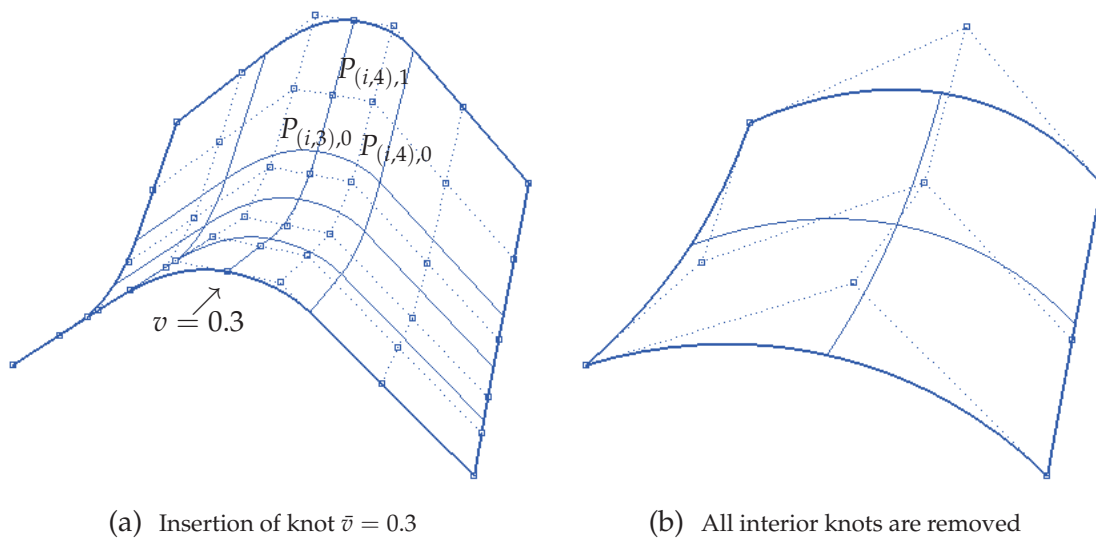


Figure 4.17: Knot insertion and removal. Compare with example shown in fig. 4.5(a) .

4.5 Final Remarks

The exactness of B-spline approximation to nodal coordinates loses some significance when the design space of possible shapes has to be reduced for shape optimization. This is the case when the designer reduces the number of control points, so that the geometrical model do not deviate considerably from the initial shape, and at the same time only smooth changes in curvature can take place. Thus, the fitting algorithm has to compute the best possible geometry out of a reduce number of control points, which increases the error of the final surface with respect to the given data.

Regarding shape control, it is important to have in mind that the increment in polynomial degree is another way to increases the area of influence of each control point.

If the accuracy of the presented solution for surface fitting need to be improved, additional constraints could be included in the approximation algorithm as explained in [PT97] for weighted and constrained curve approximation. In general, NURBS fitting is more accurate than B-spline fitting, since weights give an additional degree of freedom to the process. Nevertheless, negative weight could be generated in the fitting calculation, and would produce as a consequence discontinuities in the surface representation [PT02]. Reference [MK98] proposes a two step linear approach for NURBS fitting. The method solves first for weights applying eigenvalue decomposition techniques to avoid negative weights, and subsequently the location of control points is obtained.

Weights were excluded as variables from the fitting algorithms in the subsequent examples, due to the unnecessary (for the kind of examples analysed in this work) higher complexity resulting in the fitting process. One has to also keep in mind, that weight modification produces distortions in the parametric domain (and in the FE-mesh obtained thereof), and additional mesh-regularization methods are needed.

Chapter 5

Stability Analysis

This chapter begins with an introduction to the concept of structural stability and its relevance in structural analysis of slender structures. General geometrically nonlinear formulations, including non-linear force boundary condition, and second order approaches used to estimate the critical load are briefly described. Material nonlinearities are not considered in the mathematical model for structural analysis as it was explained in section 2.4.

Finally, some examples of pressurized bulkheads are presented in order to compare geometrically nonlinear and linearized prebuckling results. The differences obtained between both methods can be used as an indicator for how accurate the design after optimization would be regarding stability. All structural responses during shape optimization are obtained from linear structural theory where the critical load is approximated by linearized prebuckling.

5.1 Introduction

Slender structures or structural components, might be susceptible to instability when an important fraction of the applied load is compensated by internal compressible stress. The particular characteristic of this kind of structures is that either one or two of its physical dimensions are very large compare to the other(s), as it is the case of thin-walled shells studied along this report.

Bushnell in reference [Bus89] analyses the buckling behavior of thin shells from a practical perspective using an important number of real and computer-simulated examples. He explains very well the predisposition of thin shells to buckling phenomena using the following paragraph: *“The membrane stiffness is in general several orders of magnitude greater than the bending stiffness. A thin shell can absorb a great deal of membrane strain energy without deforming too much. It must deform much more in order to absorb an equivalent amount of bending strain energy. If the shell is loaded in such a way that most of its strain energy is in the form of membrane compression, and if there is a way that this stored-up membrane energy can be converted into bending energy, the shell may fail rather dramatically in a process called “buckling”, as it exchanges its membrane energy for bending energy. Very large deflections are generally required to convert a*

given amount of membrane energy into bending energy.”. Buckling is consequently associated to structural collapse after the shell reaches a point of instability. There exist two types of instability failure or buckling modes.

Buckling modes The same author [Bus89] classifies buckling of thin shells in two different modes: non-linear collapse (figure 5.1(a)) and bifurcation buckling (figure 5.1(b)). Other authors like Riks [Rik84] call them snapping and buckling phenomena. The first mode is characterized by a reduction of the structural stiffness (the slope of a representative load-deflection diagram) with increasing load. The critical load is reached when the total stiffness becomes zero. Since the load is maintained, large displacement take place in a sudden movement and the structures snaps through to a new position of equilibrium where the load can be again supported. In the second buckling mode, the sudden increment of displacements develops along a different path, so that the post-buckling pattern of deformation differs from the prebuckling one. Failure occurs if the post-buckling path has a negative slope and the load is independent of the deformation amplitude.

True bifurcation buckling, whose critical load can be estimated analytically in certain cases, does not occur in real structures due to the existence of unavoidable imperfections. The dotted path of figure 5.1(b) shows the non-linear collapse of an imperfect structure displaying a limit-point behavior.

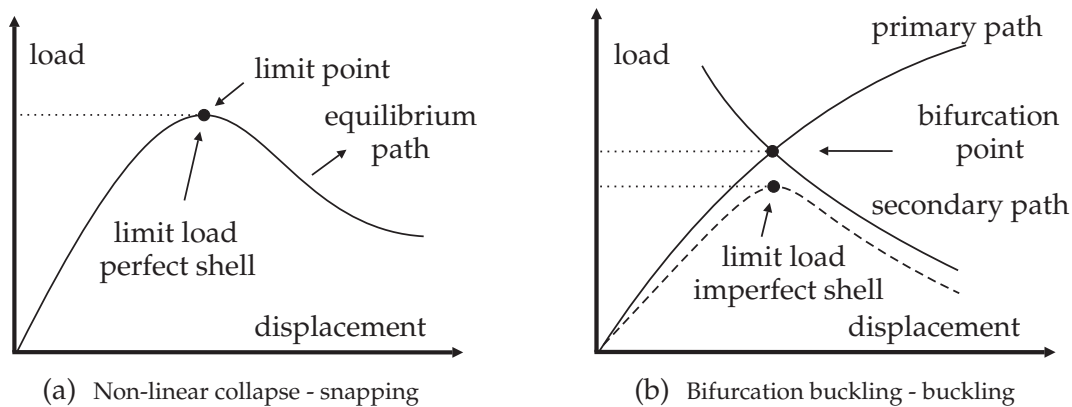


Figure 5.1: Buckling modes. Load-deflection response diagrams.

Equilibrium path Another important concept in structural stability is the load-deflection history of a non-linear system. The load-deflection (or load-displacement) history represents a curve in a $(N + 1)$ -dimensional space, where N stands for the number of degrees of freedom of the system and the dimension of the magnitude of the reference load represents the additional parameter. Such a curve is usually referred to as equilibrium path or deformation path and represents configurations of static equilibrium. Graphical representations of this concept is done by means of response diagrams. The most widely used is the

load-deflection (load-displacement) response diagram, which is a two-dimensional representation of the $(N + 1)$ -dimensional load-deflection history. One dimension corresponds to a fraction of the representative load, and the second dimension to the representative deflection associated to the selected degree of freedom u_i (see for instance figure 5.1). For simple structures the selection of the degree of freedom for the two-dimensional representation is often direct and evident. For more complex structures the candidate to be selected may not be that obvious. In the examples shown along this report, the representative load in the load-deflection diagrams is the applied pressure load.

Within the frame of computational modeling of structures using finite elements, the equilibrium path is found using incremental-iterative methods which are briefly described later. These numerical methods compute discrete points of structural equilibrium, so that the load-deflection history is constructed out of them.

Critical points The definition of critical points (singular or non-regular points) is implicitly used in the definition of buckling modes. The point at which the critical load has been localized on a load-deflection response diagram, where either a snapping or buckling problem develops, is called a critical point. They are also called limit and bifurcation points respectively as indicated in figure 5.1 and represent locations in the load-displacement history where the tangent stiffness matrix \mathbf{K} becomes singular. Reference [Fel01] identifies other special equilibrium points such as turning and failure points, which are of less interest to the present research.

5.2 Non-Linear Stability Analysis

Non-linear stability analysis is related to the location of critical points (limit points or bifurcation points), at which the structure still remains within operational range.

Since the constraint which prevents stability problems during optimization is the limit or critical load found by means of linearized prebuckling (see sections 5.3 and 6.5.2), non-linear stability analysis is the tool which contributes to verify the performance of the optimal design. This more realistic mathematical model includes geometrical and force boundary condition nonlinearities. For this reason, the stability analysis on the different examples shown along this report focuses basically on the location of the first critical point whose load factor is a reference value to be compared with the approximation given by linearized pre-buckling.

Geometric non-linearity appears in the kinematic equations due to the nonlinear nature of the Green-Lagrange strain tensor shown in equation (2.16) (written using covariant base vectors),

$$\mathbf{E} = \frac{1}{2} (\mathbf{g}_i \cdot \mathbf{g}_j - \mathbf{G}_i \cdot \mathbf{G}_j) \mathbf{G}^i \otimes \mathbf{G}^j. \quad (5.1)$$

The principle of virtual work with respect to the initial configuration is given by (see equation 2.28)

$$\delta W(\mathbf{u}) = \int_{\Omega_0} \mathbf{S} : \delta \mathbf{E} dV - \int_{\Omega_0} \mathbf{B} \cdot \delta \mathbf{u} dV - \int_{\partial\Omega_0 \sigma} \hat{\mathbf{T}} \cdot \delta \mathbf{u} dS = 0. \quad (5.2)$$

After discretization and taking the gradient with respect to one of the degrees of freedom u_r (see equation 2.59), the r^{th} component of the resulting vector of equilibrium \mathbf{R} is

$$\frac{\partial W(\mathbf{u})}{\partial u_r} = \int_{\Omega_0} S^{ij} (\mathbf{g}_{i,r} \cdot \mathbf{g}_j) dV - \int_{\Omega_0} \mathbf{B} \cdot \mathbf{u}_{,r} dV - \int_{\partial\Omega_0 \sigma} \hat{\mathbf{T}} \cdot \mathbf{u}_{,r} dS = R_r = 0. \quad (5.3)$$

Now written in vector form,

$$\frac{\partial W(\mathbf{u})}{\partial \mathbf{u}} = \mathbf{R}_{int}(\mathbf{u}) - \mathbf{R}_{ext}(\mathbf{u}) = \mathbf{R}(\mathbf{u}) = \mathbf{0}. \quad (5.4)$$

This algebraic system, which represents equilibrium of forces at nodal level, is known as residual equations, and the resulting vector \mathbf{R} corresponds to the out-of-balance nodal forces, also called residual vector.

When the nonlinear problem is conservative, it is possible to develop a variational principle. Stresses and external loads can be obtained from potentials, since in a conservative problem constitutive equations and loads are path independent. Therefore, equation (5.4) can be also derived by taking the gradient of the total potential energy Π of the system, where internal and external energy components (strain energy and external work function respectively) are balanced [Fel01].

Force boundary condition included in the analysis is characterized in section 5.2.2, where the specific nonlinearity is known as follower force. In general, external loads are conservative if they return to the original position and their value remains after the structure goes back to this original configuration.

The solution of the non-linear equilibrium equations, where residual between internal and external forces vanishes, produces as a result the equilibrium path. Iterative-incremental methods [Wri01] which consider numerical algorithms for computational implementation, have been developed in the last years in order to obtain discrete points along the equilibrium path as accurate as possible. Some of them are briefly commented in the next section.

5.2.1 Following the History Path, Incremental-Iterative Methods

In order to obtain discrete approximations to equilibrium states along the history path, where critical points have to be localized, incremental-iterative methods have been developed as a solution strategy for non-linear formulations discretized by finite elements. They consist basically on two nested approaches also called predictor-corrector method. The first one, incremental analysis, defines how close (or far) from each other discrete configurations are calculated, how smooth the history path is going to be characterized. In the second approach iterative algorithms are used to improve the accuracy and correct the value of the incremental prediction. Both methods are briefly mentioned in the following sections.

There exist one more solution method located outside incrementation as a third nested solution method for non-linear problems called stages [Fel01]. It is related to the order of application in which several load cases are considered to be acting over the structure. Since only one load case is affecting the outcome of results in the presented examples, there will be no further mention to this particular solution method.

5.2.1.1 Continuation Methods, Incremental Analysis

The general strategy of an incremental method is to find solutions at every incremental step which correspond to a continuous deformation of the structure from the undeformed state. Each equilibrium state obtained in the process is then used to construct the starting configuration for the next iteration. The accuracy of the initial state can be controlled by keeping the distance between the known and unknown points relative small. This distance is called incremental step. All equilibrium states resulting from every incrementation are taken as discrete configurations along the history path, with which load-displacement diagrams are constructed.

As it was mention in the first chapter, in the following examples it is assumed that only one load case is acting on the structure, namely uniform distributed pressure p . This load is multiplied by the factor λ , which gives the load the incremental nature. After one incremental step, both load and displacement increments are solved together to obtain the load history of the system. Equation (5.4) is rewritten in its incremental form

$$\mathbf{R}(\mathbf{u}, \lambda) = \mathbf{R}_{int}(\mathbf{u}) + \lambda \mathbf{R}_{ext}(\mathbf{u}) = \mathbf{0}. \quad (5.5)$$

Equation (5.5) is denominated one-parameter residual equation, since only one load condition is present and subject to variation. λ is usually called the control parameter representing load levels, and displacements are known as state variables, since they give information about the state of the structure. During each incremental step the control parameter λ and the state parameters \mathbf{u} undergo finite modifications denoted by $\Delta\lambda$ and $\Delta\mathbf{u}$ respectively. Incremental step are usually identified by the subscript n . For instance, after incremental step n , control and state parameters are denoted by λ_n and $\Delta\mathbf{u}_n$ respectively.

The size of the incrementation plays a very important role in structural stability. There are problems in which the detection of critical points (especially bifurcation points) can be missed when the incremental step is large enough.

Due to the inclusion of the control parameter λ as an additional unknown to the displacement field \mathbf{u} in the set of equilibrium equations (5.5), one more equation is needed

$$g(\mathbf{u}, \lambda) = 0, \quad (5.6)$$

so that the mathematical problem is set to be determinate by having the same number of equations an unknowns. This additional constraint can be used to control the increment

size $(\Delta \mathbf{u}_n, \Delta \lambda_n)$ directly or indirectly to enhance robustness and convergence. The series of discrete solutions $(\mathbf{u}_n, \lambda_n)$ follow and approximate the equilibrium path with a certain accuracy. This accuracy is set by one or several termination criteria included in the correction solution method.

If incrementation is assumed to be driven by a parametric variable t called pseudo time which at each incremental step defines the values of $\Delta \mathbf{u}_n(t)$ and $\Delta \lambda_n(t)$, the rate of change of equation (5.5) (incremental path equation) can be calculated as

$$\frac{d\mathbf{R}(\mathbf{u}, \lambda)}{dt} = \frac{\partial \mathbf{R}}{\partial \mathbf{u}} \frac{d\mathbf{u}}{dt} - \frac{\partial \mathbf{R}}{\partial \lambda} \frac{d\lambda}{dt} = \mathbf{0}, \quad (5.7)$$

which is the fundamental equation of purely incremental methods [Fel01]. The expression $\partial \mathbf{R} / \partial \mathbf{u} = \mathbf{K}$ is the tangent stiffness matrix (see equation (2.61) and section 5.2.1.4) of the system, and $\partial \mathbf{R} / \partial \lambda$ the incremental load vector. Solving for $d\mathbf{u} / dt$ and assuming symmetry of \mathbf{K} we obtain

$$\frac{d\mathbf{u}}{dt} = \mathbf{K}^{-1} \frac{\partial \mathbf{R}}{\partial \lambda} \frac{d\lambda}{dt}. \quad (5.8)$$

As an example, equation (5.6) is considered to be

$$g(\mathbf{u}, \lambda) = g(\lambda) = \Delta \lambda_n - l_n = 0, \quad (5.9)$$

which prescribes the load increment to be $\Delta \lambda_n = l_n$. This is the simplest increment control strategy called load control where λ becomes the independent variable. Using for instance the Euler method as a first order method to approximate the solution of differential equations, the value of the next incrementation for the displacement vector can be computed as

$$\mathbf{u}_{n+1} = \mathbf{u}_n + \Delta \lambda \frac{d\mathbf{u}}{dt}. \quad (5.10)$$

The value of $d\mathbf{u} / dt$ is taken from equation (5.8), where dt is now replaced by $d\lambda$, since λ is the independent variable which defines the size of the increments. Thus $d\lambda / dt$ in (5.8) becomes $d\lambda / d\lambda = 1$. Finally incremental steps are computed using

$$\begin{aligned} \lambda_{n+1} &= \lambda_n + l_n, \\ \mathbf{u}_{n+1} &= \mathbf{u}_n + l_n \mathbf{K}^{-1} \frac{\partial \mathbf{R}}{\partial \lambda}, \end{aligned} \quad (5.11)$$

given the initial condition

$$\begin{aligned} \mathbf{u}_0 &= \bar{\mathbf{u}}, \\ \lambda_0 &= 0. \end{aligned} \quad (5.12)$$

When only incremental methods are used without improving the approximation by means of iterative methods the so called drifting error appears. There will generally be a residual vector different from zero ($\mathbf{R} \neq \mathbf{0}$: out-of-balance residual vector) when discrete solutions are replaced in the equilibrium equation (5.5). This error is not only given by the local approximation of the original nonlinear function (either linear or using higher order methods), but also depends on the size of the increment.

5.2.1.2 Corrective Phase, Iterative Methods

Corrective methods based on iterative procedures are used within every increment, so that the residual force vector can be balanced and the total stiffness of the system is more accurately calculated. Here is when the most common solution approach for nonlinear system of equations, the Newton-Raphson method and variations of it are addressed. A consistent linearization of the equilibrium equations is a pre-requisite. At this level of the approximation the selected incremental step is not only important for a more continuous outline of the history path, but it also provides a good initial guess for the iteration-correction algorithm. Small enough size of incrementation are preferred particularly for highly nonlinear formulations. The reason is that Newton methods increase their rate of convergence as they get closer to the solution.

Newton-Raphson and Newton-like methods are not only important for the solution of non-linear structural problems, but also a fundamental tool in the solution of non-linear optimization problems. There is a large list of references regarding numerical solutions and their computational implementation for nonlinear system of equations. See for instance [Kel03] [DS96] [SW03] [NW06].

Within incrementation, iteration steps are usually identified by the superscript k . For instance, at incremental step n and iteration k control and state parameters are denoted by λ_n^k and $\Delta \mathbf{u}_n^k$ respectively.

Again the problem is to find the next incremental solution \mathbf{u}_{n+1} , λ_{n+1} after increment $(\mathbf{u}_n, \lambda_n)$ using

$$\begin{aligned}\mathbf{u}_{n+1} &= \mathbf{u}_n + \Delta \mathbf{u}_n, \\ \lambda_{n+1} &= \lambda_n + \Delta \lambda_n.\end{aligned}\tag{5.13}$$

The previous increments $(\Delta \mathbf{u}_n, \Delta \lambda_n)$ will be calculated by iterative techniques, so that the residual differential equation (5.5) is fulfilled within a given tolerance for the new discrete point $(\mathbf{u}_{n+1}, \lambda_{n+1})$. The equation system to be solve now is

$$\begin{aligned}\mathbf{R}(\mathbf{u}_{n+1}, \lambda_{n+1}) &= \mathbf{0}, \\ g(\mathbf{u}_n, \lambda_n) &= 0.\end{aligned}\tag{5.14}$$

The additional equation $g = 0$ gives again the implicit or explicit relation between variable increments $(\Delta \mathbf{u}_n, \Delta \lambda_n)$. Section 5.2.1.3 shows some well-known examples for the additional constraint $g = 0$.

Considering the linear terms of the Taylor expansion at point $(\mathbf{u}_n^k, \lambda_n^k)$ for equations (5.14),

$$\begin{aligned}\mathbf{R}^{k+1} &= \mathbf{R}^k + \frac{\partial \mathbf{R}^k}{\partial \mathbf{u}} \Delta \mathbf{u}_n^k + \frac{\partial \mathbf{R}^k}{\partial \lambda} \Delta \lambda_n^k = \mathbf{0}, \\ \mathbf{g}^{k+1} &= \mathbf{g}^k + \frac{\partial \mathbf{g}^k}{\partial \mathbf{u}} \Delta \mathbf{u}_n^k + \frac{\partial \mathbf{g}^k}{\partial \lambda} \Delta \lambda_n^k = 0,\end{aligned}\tag{5.15}$$

where $\partial \mathbf{R}^k / \partial \mathbf{u}$ is the tangent stiffness matrix (see equation (2.61) and section 5.2.1.4) and $\partial \mathbf{R}^k / \partial \lambda$ the incremental load vector which is equal to the applied load \mathbf{R}_{ext} if load increments depend linearly on λ , both expressions evaluated at point $(\mathbf{u}_n^k, \lambda_n^k)$. The following relations are added to the previous system of equations in order to find the next iteration step,

$$\begin{aligned} \mathbf{u}_n^{k+1} &= \Delta \mathbf{u}_n^k + \mathbf{u}_n^k, \\ \lambda_n^{k+1} &= \Delta \lambda_n^k + \lambda_n^k. \end{aligned} \quad (5.16)$$

Newton-like methods offer the possibility of approximating either the tangent stiffness matrix \mathbf{K} or its inverse \mathbf{K}^{-1} , so that computational time for calculating their analytical values can be saved in case the system of equations is very large. Line search Techniques also help to increase the effectiveness of Newton methods when convergence is slow due to substantial deviations from the solution.

The matrix form of the linearized incremental equations excluding sub- and superscripts (n^k) is written as,

$$\begin{bmatrix} \mathbf{K} & \frac{\partial \mathbf{R}}{\partial \lambda} \\ \frac{\partial \mathbf{g}}{\partial \mathbf{u}} & \frac{\partial \mathbf{g}}{\partial \lambda} \end{bmatrix} \begin{bmatrix} \Delta \mathbf{u} \\ \Delta \lambda \end{bmatrix} = - \begin{bmatrix} \mathbf{R} \\ \mathbf{g} \end{bmatrix} \quad (5.17)$$

The coefficient matrix of the linear system (5.17) is called augmented stiffness matrix. It is generally non-symmetric, although the tangent stiffness matrix \mathbf{K} is generally symmetric. The augmented stiffness matrix is however symmetric at bifurcation points. The techniques to solve the previous system of equations which takes advantage of this attributes is called partitioning. It makes use of auxiliary system of equations which depends on whether the tangent stiffness matrix \mathbf{K} is non-singular or singular. Stabilization approaches might be needed near critical points in order to avoid numerical instabilities.

These techniques as well as a complete review of different numerical approaches aiming to find approximations to solutions of nonlinear differential equations coming from structural formulations, are found, for instance in references [Wri01] and [Fel01]. The presented overview was extracted mainly from these two sources.

Detection of critical points while following the equilibrium path is done by using certain indicators which monitor the solution. One of these indicators is the smallest eigenvalue ω_i of the problem $(\mathbf{K} - \omega \mathbf{I})\boldsymbol{\phi} = \mathbf{0}$ ¹. Another possibility is to track the sign change of the determinant of the tangent stiffness, which indicates a transition from stability to instability². A more accurate indicator would be to consider the change of sign of every single element along the diagonal of \mathbf{D} ; if at least one of them shows this behavior, an unstable configuration has been found. At bifurcation points, the number of zero eigenvalues is an indicator for the number of paths the structure can follow. The corresponding eigenvector indicates

¹expensive to compute but the minimum eigenvalue can be also monitored by considering the coefficient with minimum real value in the diagonal matrix \mathbf{D} in the alternative Cholesky decomposition $\mathbf{K} = \mathbf{L}^T \mathbf{D} \mathbf{L}$

²This indicator fails when the zero eigenvalue has even multiplicity

the type of deformation that take place.

There exist algorithms which allow a direct localization of critical points once a path following strategy has reached their vicinity. To this methods belongs the bisection approach [Wri01] which has only linear rate of convergence. Incremental-iterative methods which directly compute critical points have a quadratic rate of convergence. They are based on the non-linear equation system (5.5) extended with additional equations which are satisfied at critical points. For instance, equations $\det(\mathbf{K}) = 0$ and $\mathbf{K}\boldsymbol{\phi} = \mathbf{0}$ which include an additional unknown $\boldsymbol{\phi}$. Again, a consistent linearization of the system of equations is a requisite, so that iterative solution methods can be used. details about these techniques can be found for instance in references [Rei94] [Wri01].

5.2.1.3 Solution Strategies

The following table was extracted from reference [Wri01]. It contains a list of additional constraints, in order of ascending complexity. The first constraint correspond to the classical load control where the load parameter λ is used as the prescribed variable. Each approximated solution is the result of the intersection of a plane of constant parameter $\bar{\lambda}$ with the equilibrium path. After the increment $\Delta\lambda_n$ has been fixed as $\Delta\lambda_n = \bar{\lambda} - \lambda_{n-1}$ at each iteration step the value of λ does not change and $\Delta\lambda_n^k = 0$. The second equation is the constraint for the displacement control approach. It is a special case of state control methods, where a norm of \mathbf{u} is specified. This special case defines only one degree of freedom of \mathbf{u} which is set to be fixed during iterations. Thus, a representative degree of freedom should be selected. The selection is not always evident and generally requires a previous knowledge of the structural behavior³. Load control and displacement control techniques may show numerical problems and fail at limit and turning points respectively [Cri81].

The third equation defines the arch-length control which specifies a distance Δs along the tangent to the path from the last solution on the equilibrium path $(\mathbf{u}_n^k, \lambda_n^k)$. This distance defines a plane normal to the tangent vector whose intersection with the equilibrium path is approached during corrective iteration. This equation is linear in \mathbf{u} and λ . Equation four defines the hyper-spherical control which is considered to be a variation of the arch-length method as it is the case for other nonlinear constraints [RCC08]. Geometrically, this constraint defines the surface of a sphere with center at $(\mathbf{u}_n^k, \lambda_n^k)$. It is a special case of the hyper-elliptic control [Fel01].

For instance references [Rik84] and [RCC08] present a review of the arc-length method and variations of it. They allow the computation of load history diagrams to go beyond singular points. Arc-length methods usually require one more constraint which decides the direction of the path to be followed, so that at some locations the problem of reversing the path can

³after analysing the structural behavior using load-control a suitable degree of freedom can be usually localized

Nr.	Name	Constraint
1.	Load-control	$g = \lambda - \bar{\lambda}$
2.	Displacement-control Batoz, Dhatt (1979)	$g = u_A - \bar{u}$
3.	Arch-length method Riks (1972)	$g = (\mathbf{u}_n - \bar{\mathbf{u}})^T (\mathbf{u} - \mathbf{u}_n) + (\lambda_n - \bar{\lambda})(\lambda - \lambda_n)$
4.	Arch-length method Criesfield (1981)	$g = \sqrt{(\mathbf{u} - \bar{\mathbf{u}})^T (\mathbf{u} - \bar{\mathbf{u}})} + (\lambda - \bar{\lambda})^2 - \Delta s$

Table 5.1: Examples for additional constraint $g(\mathbf{u}, \lambda)$. Source [Wri01].

be avoided.

5.2.1.4 Tangent Stiffness Matrix

The tangent stiffness matrix (also called Jacobian or Hessian matrix) is obtained by differentiating the residual vector \mathbf{R} with respect to the components of the displacement vector \mathbf{u} while keeping λ fixed.

$$\mathbf{K} = \frac{\partial \mathbf{R}}{\partial \mathbf{u}}. \quad (5.18)$$

The partial derivative of the residual vector in (5.18) generates several terms which constitute the tangent stiffness matrix. These terms are listed in the next paragraphs.

Material stiffness Its name comes from its dependency on the material properties included in the material matrix \mathbf{C} . At the reference configuration when the displacement field \mathbf{u} is equal to zero, this matrix takes the value of the linear elastic matrix \mathbf{K}_e obtained from linear theory of small deformation and small strains [Hug00]. The material stiffness matrix is some times split into two components $\mathbf{K}_m = \mathbf{K}_e + \mathbf{K}_u$ for some applications (see equation 5.26). The first component \mathbf{K}_e is independent of the displacement field, as opposed to the second component \mathbf{K}_u . The last term is called initial displacement matrix. It is equal to zero at the reference configuration.

$$\mathbf{K}_m = \mathbf{K}_e + \mathbf{K}_u = \int_{\Omega_0} \frac{\partial \mathbf{E}}{\partial \mathbf{u}} : \mathbf{C} : \frac{\partial \mathbf{E}}{\partial \mathbf{u}} dV. \quad (5.19)$$

Geometric stiffness or initial stress stiffness, appears from the non-linear term of the strain tensor. It does not depend on any material properties, but only on the stress state at the current configuration. It is invariant to rotations.

$$\mathbf{K}_g = \int_{\Omega_0} \mathbf{S} : \frac{\partial^2 \mathbf{E}}{\partial \mathbf{u}^2} dV. \quad (5.20)$$

External load stiffness External loads might be dependent on the displacement field \mathbf{u} as well. The pressure load \mathbf{p} (see section 5.2.2) is a good example of this type. Since it should maintain always a normal direction with respect to the loaded surface, its magnitude changes as the structure undergoes geometrical modifications.

$$\mathbf{K}_l = \int_{\partial\Omega_0} \frac{\partial \mathbf{p}}{\partial \mathbf{u}} dS. \quad (5.21)$$

5.2.2 Follower Forces

Some structural loads will depend on the deformation of the solid. In certain cases when the body is under the influence of a fluid, which produces different pressure magnitudes depending on the relative position in space of the body with respect to the free surface, the magnitude and direction of the load are position dependent. They belong to the group of space attached loads.

Pressure loads produced by a pressure difference between two environments (e.g a closed chamber where the value of inner- and outer pressure differ) remain always normal to the surface at every application point, and its magnitude is independent on the position in space. This kind of loads belong to the category called body attached loads. Their conservativeness depends on the kind of boundary condition and it is reflected in the symmetry of their contribution to the total Hessian matrix [SR84].

The displacement dependent equation (from equation 2.29) for the surface applied pressure load $\mathbf{p} = p\mathbf{n}$ is expressed in the following form using again convective coordinates (as explained in section 2.1), and given with respect to the deformed configuration, where the normal vector is modified depending on the current nodal coordinates).

$$\delta W_{ext}(\mathbf{u}) = \int_{\partial\Omega_\sigma} \hat{\mathbf{t}} \cdot \delta \mathbf{u} da = \int_{\partial\Omega_\sigma} \hat{p} \mathbf{n} \cdot \delta \mathbf{u} da = \hat{p} \int_{\partial\Omega^\theta} (\mathbf{g}_1 \times \mathbf{g}_2) \cdot \delta \mathbf{u} d\theta^1 d\theta^2 \quad (5.22)$$

Normal vector n and differential area da at element level are substituted by the following expressions:

$$\mathbf{n} = \mathbf{g}_3 = \frac{\mathbf{g}_1 \times \mathbf{g}_2}{\|\mathbf{g}_1 \times \mathbf{g}_2\|}; \quad da = \|\mathbf{g}_1 \times \mathbf{g}_2\| d\theta^1 d\theta^2. \quad (5.23)$$

Linearization of equation (5.22),

$$\Delta \delta W_{ext}(\mathbf{u}) = \hat{p} \int_{\partial\Omega^\theta} \Delta [(\mathbf{g}_1 \times \mathbf{g}_2) \cdot \delta \mathbf{u}] d\theta^1 d\theta^2 \quad (5.24)$$

leads later to the contribution of the external load to the total stiffness matrix [Ble98], [Jar09],

$$\begin{aligned} \Delta \delta W_{ext}(\mathbf{u}) &= \frac{\hat{p}}{2} \int_{\partial\Omega^\theta} [\Delta (\mathbf{g}_1 \times \mathbf{g}_2) \cdot \delta \mathbf{u} + \delta (\mathbf{g}_1 \times \mathbf{g}_2) \cdot \Delta \mathbf{u}] d\theta^1 d\theta^2 \\ &+ \frac{\hat{p}}{2} \int_{\theta^1} (\mathbf{g}_1 \times \Delta \mathbf{u}) \cdot \delta \mathbf{u} d\theta^1 \Big|_{\theta^2=0}^1 + \frac{\hat{p}}{2} \int_{\theta^2} (\Delta \mathbf{u} \times \mathbf{g}_2) \cdot \delta \mathbf{u} d\theta^2 \Big|_{\theta^1=0}^1 \end{aligned} \quad (5.25)$$

The first two components of equation (5.25) add a symmetric contribution (stiffness of external loading) to the total stiffness matrix. The last two components are boundary integrals that cancel each other at element interfaces. Nevertheless, they could imply the addition of a non-symmetric load stiffness under certain boundary conditions. The special cases in which they can be completely removed from the formulation are given in [Jar09] and [SR84]. The most intuitive condition is when displacements are fixed ($\delta \mathbf{u} = 0$) making the total additional load stiffness symmetric, which means that the problem is conservative ([SR84]).

5.2.3 Stability Analysis of Design-Concepts

For all following examples, the corresponding critical load was estimated by load and displacement control strategies (see section 5.2.1.3). Load-displacement diagrams which display post-buckling behavior were constructed using data from displacement control approaches⁴.

The follower force method (see section 5.2.2) is only included in the particular load control approach used in this study. Nevertheless, the difference between critical loads resulting from both solution strategies were found to be negligible. This fact is depicted in figure 5.5. It displays the load-displacement diagrams resulting from load and displacement control strategies for the instability behavior of Concept D2. The same degree of freedom was selected to draw both load-displacement diagrams.

Table 5.2 contains material and loading properties which are the same for all examples along this chapter. Properties which differ from these values are explicitly indicated.

Material model	Isotropic
Elasticity Modulus	45000 N/mm ²
Poisson ratio	0.3
Thickness	6 mm
Density	1.6x10 ⁻⁶ kg/mm ³
Pressure load	0.12 N/mm ²

Table 5.2: Material properties and load of stability-examples.

⁴presence of turning points might lead to convergence problems in a displacement control strategy

5.2.3.1 Evolution of Shape

Figure 5.2(a) displays all four load-displacement diagrams of the design concepts shown in figures 1.9 and 3.3. They represent minimal surfaces calculated between arches by applying a final isotropic stress state in the form finding calculation. The location and direction of movement of the selected degree of freedom to display diagrams for every model is indicated by an arrow in figures 5.3, 5.4 and 5.6.

These four Concepts stand for the most representative shape evolution the bulkhead was subjected to. Some of these Concepts were slightly modified in order to study the effects of these modifications on the stability behavior. Some of these analysis are shown in figures 5.3, 5.4 and 5.6. Main characteristics and critical load of every design Concept are summarized in table 5.3.

Figure 5.2(b) contains two load displacement diagrams of Concept D. The degree of freedom which moves along the z axis (fig. 5.6(b)) shows initial softening of the structure at that location. The direct consequence is a large increase in displacement for a small increment in load, compared to other Concepts. Additionally, the bending stresses at that location go beyond the limit of material linearity set up for the analysis (see figure 5.7). At this point a non-linear material model would produce more realistic results. This is the reason why Concept D2 was chosen as starting design for optimization (see chapter 7) instead of Concept D. Concept D2 shows a stiffer prebuckling behavior, a higher critical load and stresses within the linear range (see figure 5.8 and 5.9 for comparison, using linear kinematics). Concept D3 which has an even higher critical load (see figure 5.6 and table 5.3), would also be an alternative to be selected as starting design for shape optimization.

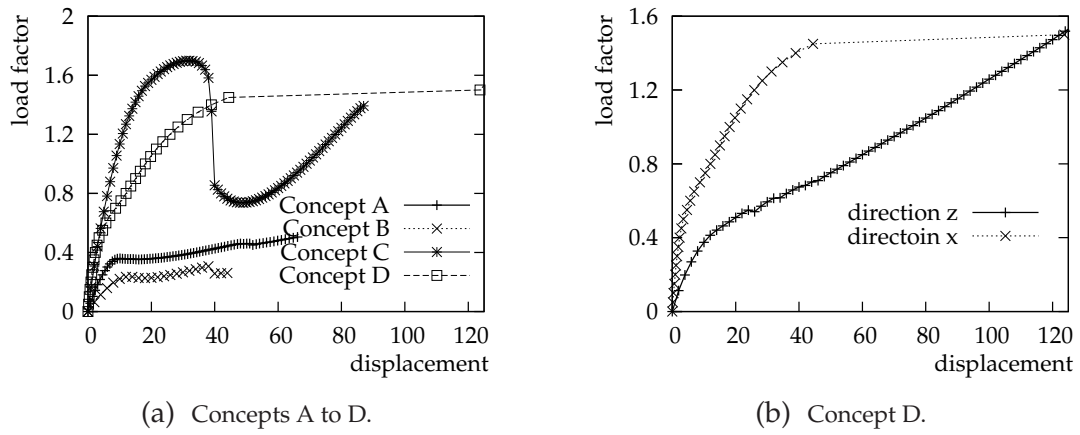


Figure 5.2: Stability analysis of concept A to D.

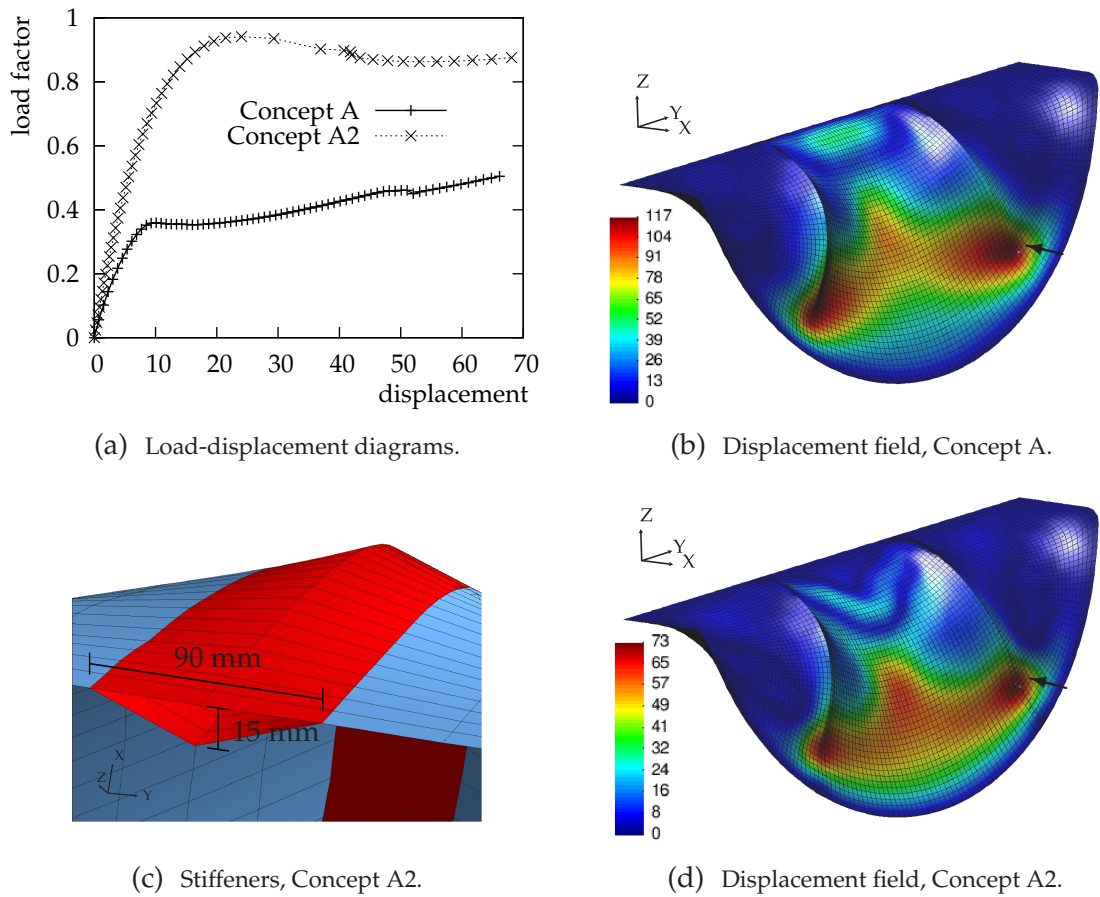


Figure 5.3: Stability analysis of Concepts A. Displacement field.

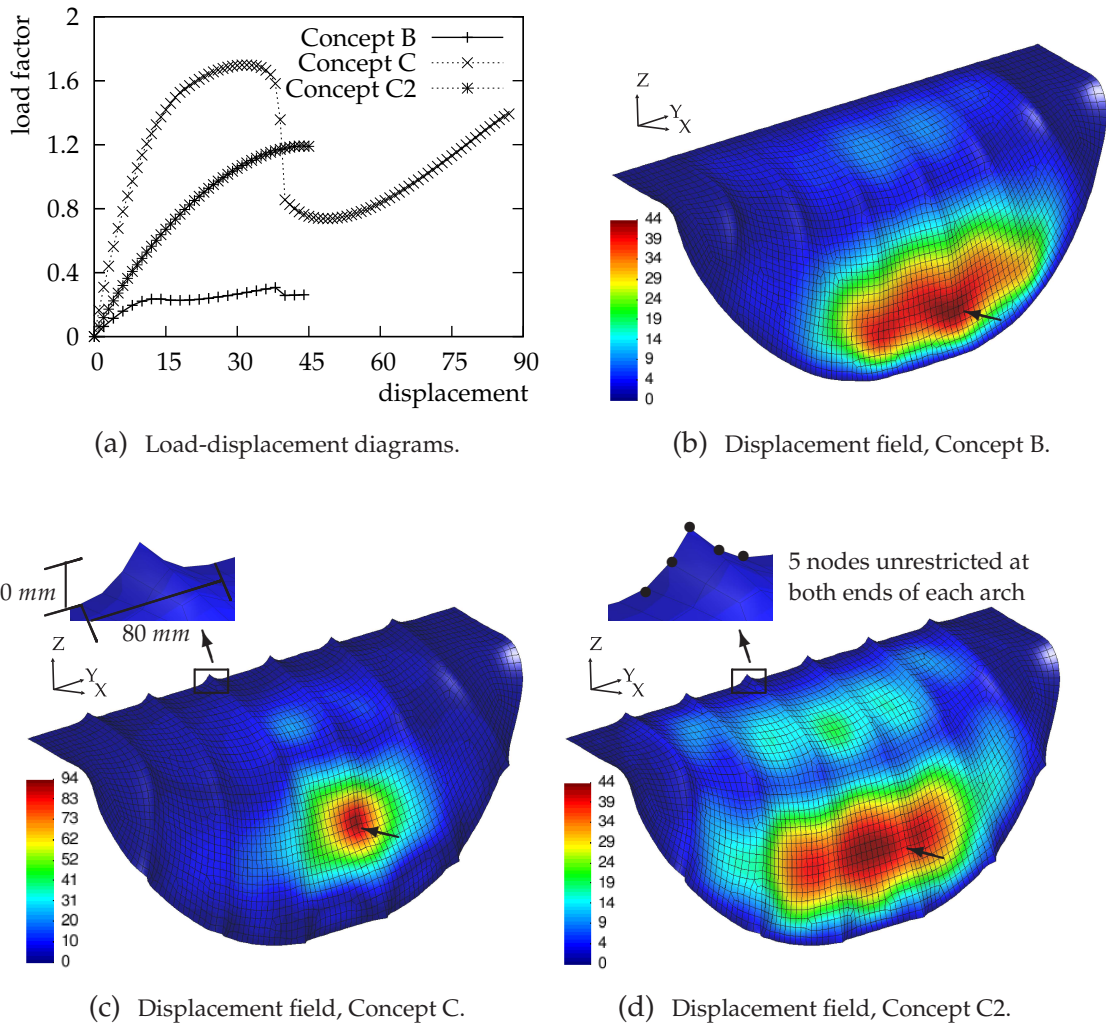


Figure 5.4: Stability analysis of Concepts B & C. Displacement field.

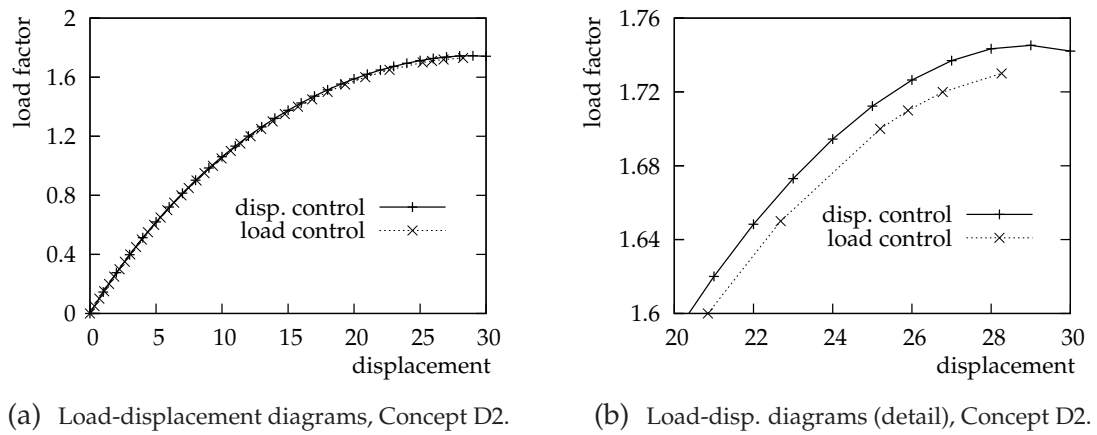


Figure 5.5: Comparison between load and displacement control strategies, Concept D2.

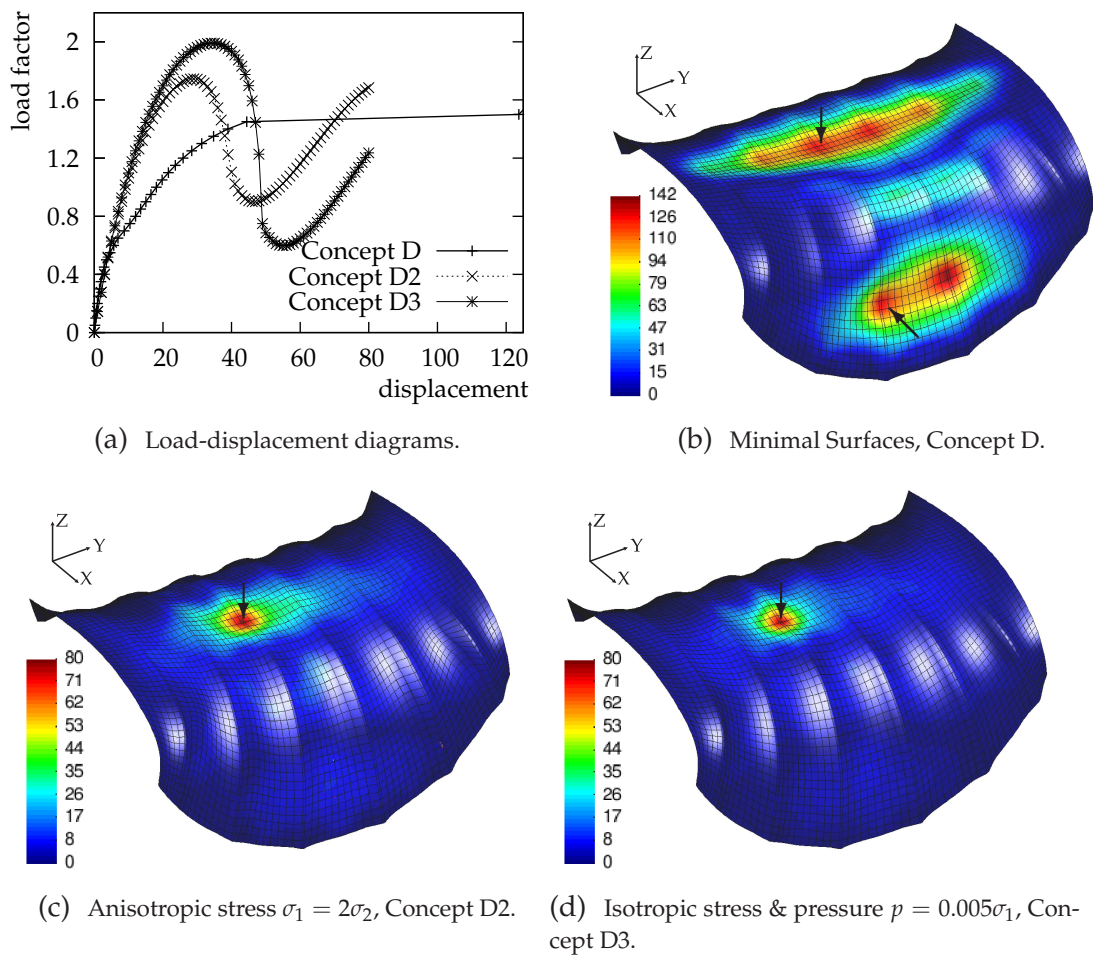


Figure 5.6: Stability analysis of Concepts D. Displacement field.

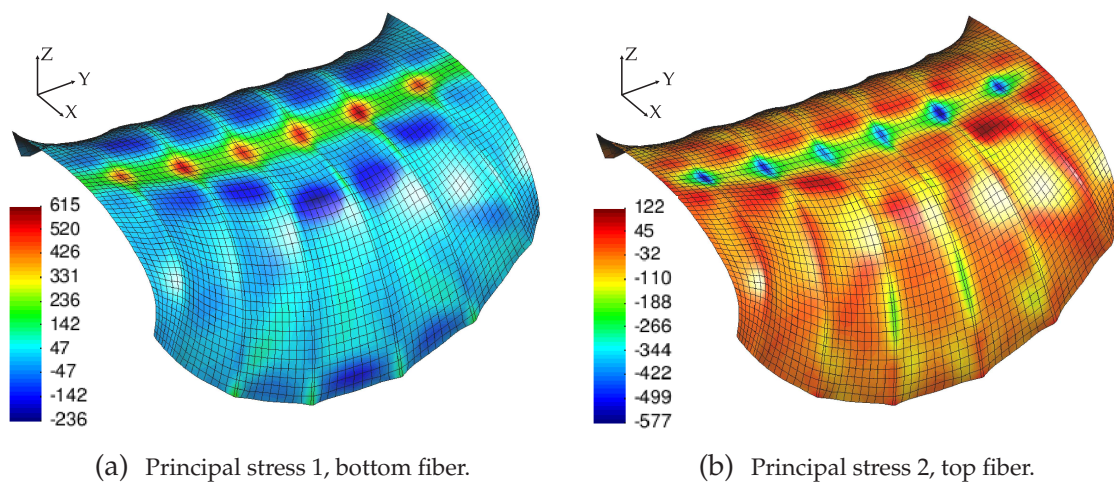


Figure 5.7: Maximum principal stresses, Concept D.

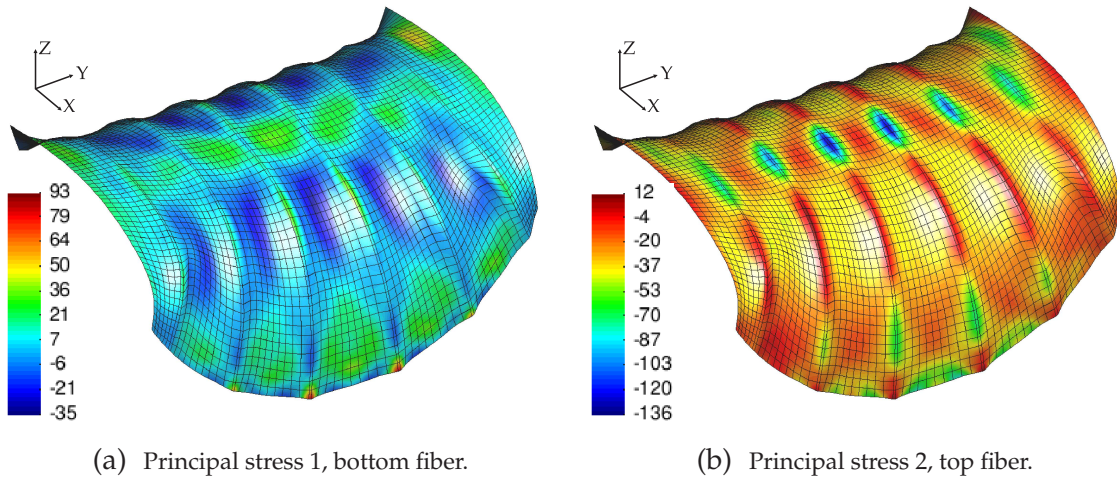


Figure 5.8: Maximum principal stresses, Concept D2.

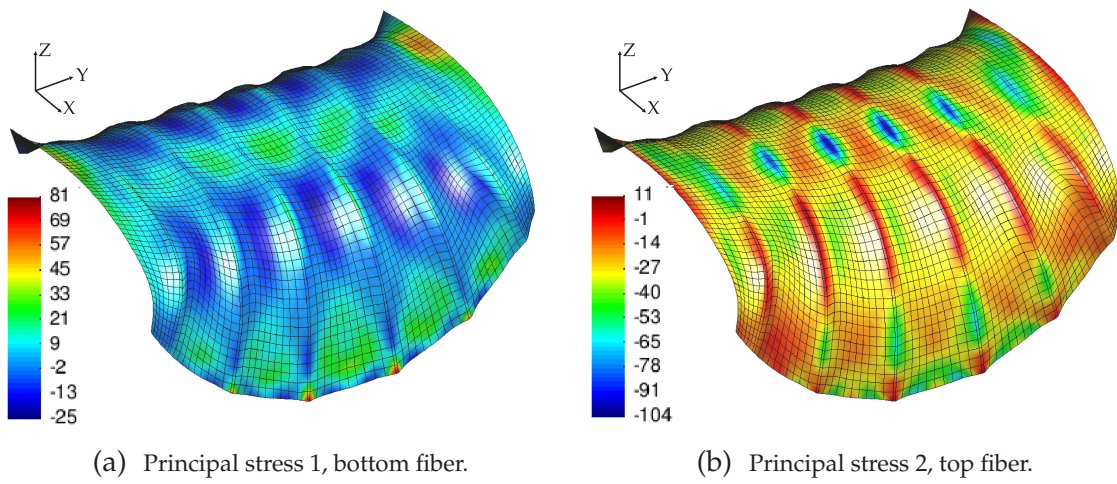


Figure 5.9: Maximum principal stresses, Concept D2, linear kinematics.

Concept	Topology / B.C.	Stress at Form Finding	λ_c
A	2 arches displacements restricted	minimal surfaces $\sigma = \bar{\sigma} \mathbf{I}$	0.36
A2	2 arches & stiffeners displacements restricted	minimal surfaces $\sigma = \bar{\sigma} \mathbf{I}$	0.94
B	6 arches displacements restricted	minimal surfaces $\sigma = \bar{\sigma} \mathbf{I}$	0.24
C	6 arches, boundary mod. displacements restricted	minimal surfaces $\sigma = \bar{\sigma} \mathbf{I}$	1.7
C2	6 arches, boundary mod. free at end of arches	minimal surfaces $\sigma = \bar{\sigma} \mathbf{I}$	1.2
D	6 arches, extended displacements restricted	minimal surfaces $\sigma = \bar{\sigma} \mathbf{I}$	1.5
D2	6 arches, extended displacements restricted	anisotropic $\sigma_1 = 2\sigma_2$	1.7
D3	6 arches, extended displacements restricted	isotropic & pressure $p = 0.005\sigma_1$	1.95

Table 5.3: Characteristics of shape concepts.

5.3 Linearized pre-buckling

As already mention in this chapter, critical points are detected when the tangent stiffness of the system becomes singular along the equilibrium path. This is when $\det(\mathbf{K}) = 0$ or when at least one of the eigenvalues ω_i of the problem $(\mathbf{K} - \omega\mathbf{I})\boldsymbol{\phi} = \mathbf{0}$ is equal to zero and represents a neutral stable configuration before instability occurs⁵. An implicit method to detect instability states is to look at the negative values of the elements of the diagonal matrix \mathbf{D} in the Cholesky decomposition of the stiffness of the system $\mathbf{K} = \mathbf{L}^T\mathbf{D}\mathbf{L}$.

The present section addresses a commonly used method which localizes directly critical points without being concerned with the demanding task of tracing equilibrium paths up to these points. The tangent stiffness matrix \mathbf{K} is considered to be linearly influenced by the displacement field \mathbf{u} . Nevertheless, the structural behavior should meet the following assumptions:

- ◇ The deformation of the structure between the initial configuration and the critical point should be small enough, so that the following applies: the material stiffness matrix \mathbf{K}_m remains practically unchanged, and the geometric stiffness matrix \mathbf{K}_g depends linearly

⁵Instability is only assured when after a neutral stability state (zero eigenvalue) the postbuckling path taken by the structure is unstable (negative slope given by negative eigenvalues)

on the applied loads (the stresses in the structure vary linearly as the load is applied). This is the case when the prebuckling behavior is practically linear.

- ◇ There are no forces acting on the structure that depends on the displacements, which means that the external load stiffness \mathbf{K}_l does not contribute to the tangent stiffness.
- ◇ The effects of imperfections do not alter structural results significantly. If the first critical load is strongly affected by imperfection, even if the estimation given by a direct method is good enough for a perfect behavior, it would be irrelevant for a real prediction.

This method sets up an eigenproblem at the reference configuration. The lowest eigenvalue gives an estimation of the critical load at which the first critical point would take place. Wriggers [Wri01] distinguish two approaches: linear and classical buckling analysis.

In linear buckling analysis, geometric (stiffness) and initial displacement matrices depend linearly on the displacement field \mathbf{u} . The general eigenvalue problem to be solved is:

$$[\mathbf{K}_e + \lambda (\mathbf{K}_u + \mathbf{K}_g)] \boldsymbol{\phi} = \mathbf{0} \quad (5.26)$$

The influence of the displacement field on the stiffness matrix is neglected when the initial displacement matrix \mathbf{K}_u is not considered in the general eigenvalue problem. This is the formulation of the second approach, the classical buckling analysis, where all components of the tangent stiffness matrix are evaluated at the initial (reference) configuration,

$$(\mathbf{K}_e + \lambda \mathbf{K}_g) \boldsymbol{\phi} = \mathbf{0} \quad (5.27)$$

This last approach is also called linearized prebuckling and it is the most common predictor of critical loads in linear elastic theory. It is suitable when elastic and initial stiffness matrices are not separately evaluated (it is usually the case of finite element codes) which would increase computational effort and implementation.

For both methods the following steps have to be calculated:

- ◇ Obtain the linear displacement field from linear theory $\mathbf{K}_e \mathbf{u}_l = \mathbf{R}_{ext}$
- ◇ Using the linear displacement field calculate geometric stiffness matrix $\mathbf{K}_g(\mathbf{u}_l)$, and initial displacement $\mathbf{K}_u(\mathbf{u}_l)$ in case of using equation (5.26).
- ◇ Solve the eigen value problem (5.27) or (5.26) where the lowest eigenvalue defines the critical load, λ_c and the associated eigenvector $\boldsymbol{\phi}_c$ gives the corresponding buckling mode.
- ◇ Compute load and displacement field at buckling from: $\mathbf{P}_c = \lambda_c \mathbf{R}_{ext}$ and $\mathbf{u}_c = \lambda_c \mathbf{u}_l$

Linearized prebuckling (equation 5.27) was included as a constraint to set a limit to the critical load during optimization. Even though the estimation of critical loads using this method

is suitable for problems where the prebuckling behavior is almost linear, the simplicity of its implementation and lower computational time involved in the calculation compared to indirect methods, makes it adequate to be part of an optimization algorithm which already requires a big amount of computational effort.

The performance of the examples shown at the end of this chapter are used to find out how accurate linear prebuckling is compared to geometrically nonlinear formulations, for the type of structures being analysed.

5.3.1 Examples

In the following two examples linearized prebuckling is employed to estimate critical loads. The first one evaluates modifications of the critical load by geometrical manipulation. The second one compares estimations of critical loads between linearized pre-buckling and non-linear results.

5.3.1.1 One-Arch Model

Figure 5.10 shows the geometry of a flat plate with one arch along it which resembles a section of one of the Concepts C or D. This model was used to study the influence of the geometry of the arch on the critical load of the plate, which is estimated using linearized prebuckling. Geometrical modifications were related to the radius of the arch. The term *outer* radius is used for several sizes of the radius without modifying the height h of the arch (see figure 5.10(b)). The term *inner* radius implies also modifications of the height of the arch (see figure 5.10(a)). Dimensions and support conditions are shown in figures 5.10(c) 5.10(d) respectively.

Table 5.4 contains the lowest eigenvalue for each configuration. The estimated critical load decreases as the height of the arch decreases. In the same way, the critical load increases as the radius increases for a constant height.

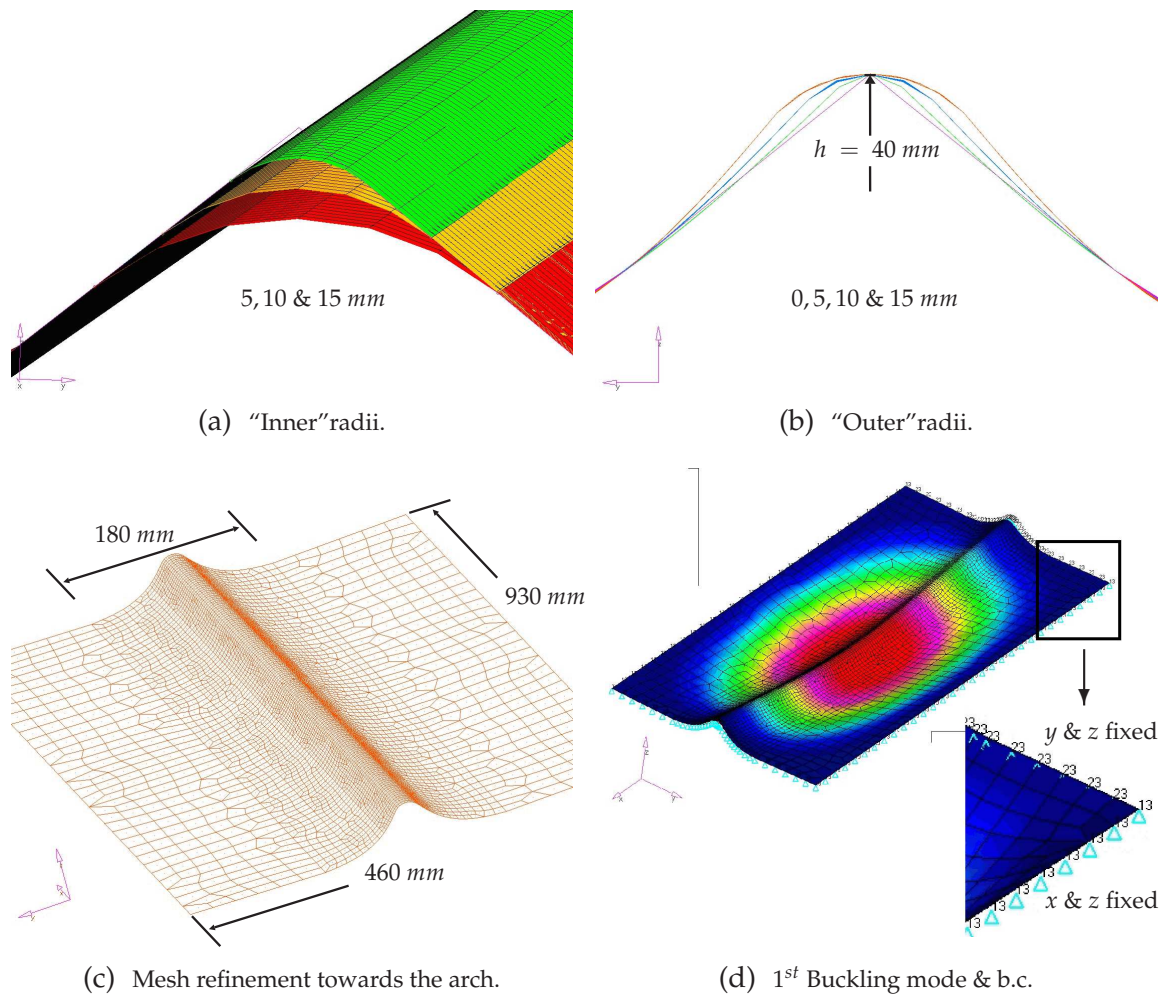


Figure 5.10: Geometric study of arches' radius. Geometry

Radius	Max. Disp.	% w.r.t 0 mm	Eigenvalue	% w.r.t 0 mm
0 mm	17.32	–	5.56	–
Inner 5 mm	17.56	1.39	5.31	-4.50
10 mm	17.85	3.06	5.02	-9.71
15 mm	18.19	5.02	4.69	-15.65
Outer 10 mm	16.83	-2.83	6.22	11.87
15 mm	16.43	-5.14	6.79	22.12

Table 5.4: One arch model. Results.

5.3.1.2 Linearized Pre-buckling v/s Non-linear Estimations

Figures 5.12 and 5.13, extracted from reference [Hör08], compare critical loads estimated by means of linearized prebuckling using the software OptiStruct (Altair) and geometrical non-linear results using CARAT. The examples are variations of the extended geometry (from Concept C to Concept D). The objective of this study was to find geometrical configurations which are able to withstand the applied load without the need of the supporting transverse beam shown in figure 5.11(b). In figures 5.12 and 5.13 the term Fix indicates the presence of such a supporting beam. Details of the nonlinear study and form finding computation can be found in [Esp08].

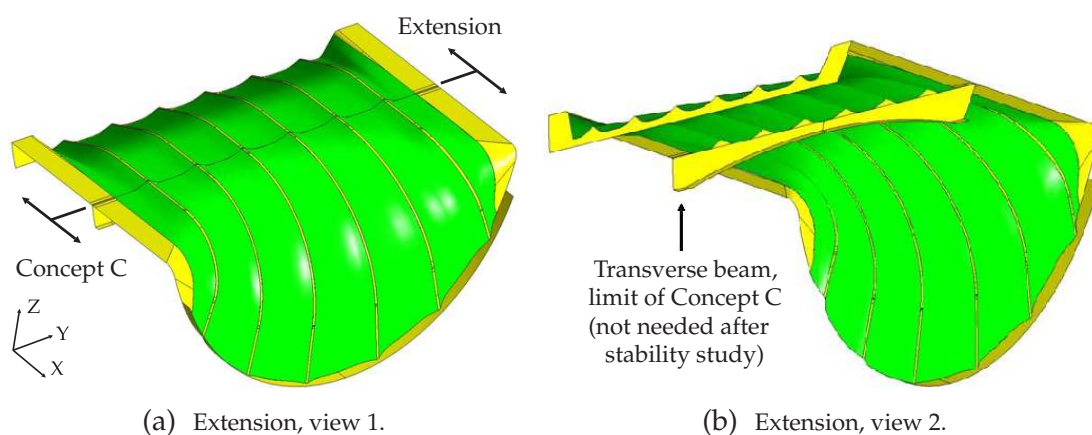


Figure 5.11: Extension of Concept C to Concept D. Source [Hör08].

As it can be concluded from the results, there is no rule that can predict non-linear critical loads from the ones approximated by linearized prebuckling or vice versa. The relation between critical loads obtain by both methods depends on the particular example which is being analysed. In some cases results provided by linearized prebuckling are a good estimation of the non-linear approximation. Nevertheless, a verification using non-linear formulations cannot be neglected.

5.4 Imperfections and their Influences in the Structural Behavior

Imperfections of ideal configurations appear as deviation from perfect parameters and may be of different kind with respect to loads, geometry and material. When structures contain some imperfection they become usually more flexible, situation that is reflected in the pre-buckling response leading to a lower limit load (see figure 5.1(b)). In the same context, the following paragraph extracted from reference [Sch00] clarifies an important characteristic of structures sensitive to imperfections: *“Physical features that distinguish highly imperfection-sensitive shells from those relative imperfection insensitivity is the different shares of membrane and bending energy in the resistance against initial buckling of a perfect shell structure”*.

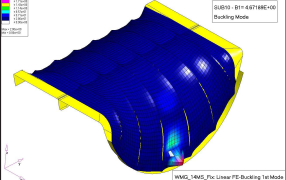
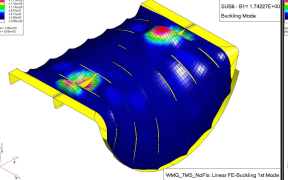
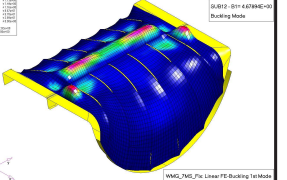
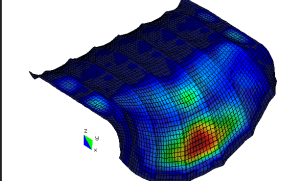
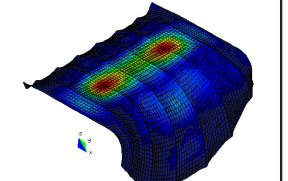
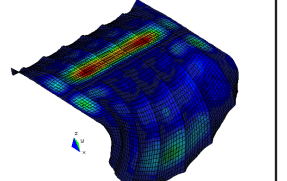
Fläche Lagerung Lastvielfache	WMG 14MS Fix	WMG 7MS NoFix	WMG 7MS Fix
1. Lastvielfaches	1,00	0,37	1,00
OS Linear 1st Buckling Mode			
Load factor	1,25	0,25	0,65
CARAT Force following load controlled simulation			

Figure 5.12: Linearized pre-buckling v/s non-linear analysis. Geometry 1. Source [Hör08].

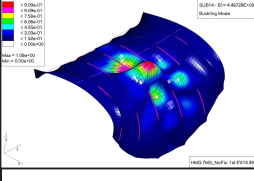
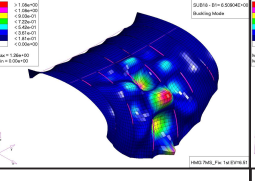
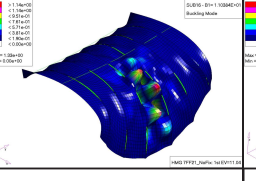
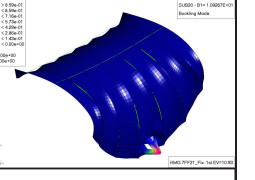
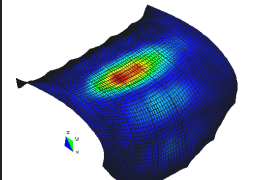
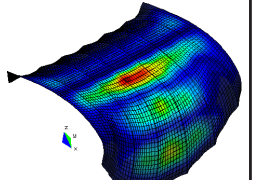
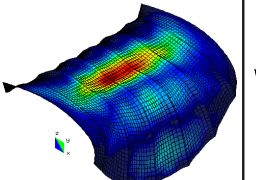
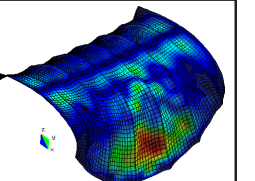
Fläche Lagerung Lastvielfache	HMG 7MS NoFix Concept D	HMG 7MS Fix	HMG 7FF21 NoFix Concept D2	HMG 7FF21 Fix
1st EV	0,96	1,39	2,37	2,34
OS 1st Buckling Mode				
Load factor	1,5	0,9	1,7	3,2
CARAT Force following load controlled simulation				

Figure 5.13: Linearized pre-buckling v/s non-linear analysis. Geometry 2. Source [Hör08].

The first question that arises when investigating the effects of imperfections is how the imperfection should be represented. It could be for example an induced strain or stress field located over a certain area of the structure, or perhaps an initial deformation configuration involving the whole member. In any case, real imperfections are not known in advance, unless they are consequence of a constant failure within an automatic manufacturing process.

One way to analyse the influence of imperfections is to carry out extensive high-quality tests on carefully designed, manufactured and controlled specimens. This is extremely costly and time consuming, particularly when a large number of specimens must be tested to ensure that a big spectrum of possible situations is covered. Another possibility is to perform numerical computations on imperfect models.

There are two strategies to approach the problem of imperfections which are associated to the computational model [Sch00]. The first one is based on the fundamental theoretical hypothesis that it is possible to estimate the structural answer of an imperfect structure from certain properties of the perfect structure. One of these methods is the perturbation energy concept [PD05]. Its advantage is that the influence of perturbation loads and geometrical imperfections is evaluated by the same physical measure, the perturbation energy. The second strategy is based on simulating the structural behavior of the shell by explicitly including in the model imperfections that may arise. The problem to be solved here is which kind of imperfection should be selected and how it should be applied.

There are three approaches regarding geometrical imperfections included in numerical models, when real data is not sufficient to generate imperfection patterns: realistic, worst and stimulating geometric imperfections [Sch00].

- ◇ Realistic imperfections try to model what is happening in reality regarding for instance manufacturing failures. These kind of deficiencies arise randomly and there is no way to model them in a deterministic manner, unless the same anomalies are induced in a systematic manufacturing process. Stochastic methods would be the best tool to treat them.
- ◇ The worst imperfection approach searches for the worst imperfection pattern over the structure that could generate for instance the lowest critical load. Some studies use the lowest linear eigenmode [NBCS96]. In case a system presents clustered eigenmode, a linear combination of them would lead to the worst imperfection pattern [NYCS02]. Now, if the pre-buckling behavior is highly nonlinear, the worst pattern should include nonlinear eigenmodes [LOW95]. In reference [RR95] nonlinear eigenmodes are included as imperfections in the optimization of thin-walled shells whose formulation is based on geometrical non-linearity. Nevertheless, even single dimple imperfections localized over a small region may be worse than eigenmodes patterns which involve the whole structure. It is also important to have in mind that besides all efforts of finding the worst imperfection pattern, its probability of occurring in practice could be very low in the most optimistic case. The maximum amplitude of the worst imperfection pattern should have real dimensions, and it should therefore be verified using

physical models. In practice, it is common to use a fraction of the thickness for shell structures [NBCS96], [NYCS02].

- ◇ The third and last approach is the stimulating geometric imperfection, where an equivalent geometric imperfection pattern is chosen as simple as possible, which can help to reduce computational costs when a large number of numerical simulations has to be performed. This simple pattern should stimulate the characteristic physical shell bucking behavior. Thus, it must have a certain geometric similarity to one of the critical eigenmodes. As it is also the case of worst imperfections, the amplitude of stimulating imperfections should be calibrated somehow.

Besides all advanced algorithms that may be implemented in a finite element code, physical verification of numerical models by performing real tests (benchmarks) is not only important for calibration purposes, but to understand that numerical models are indeed not reality.

5.4.1 Imperfection Analysis of Concept D2

Load and geometric imperfections were simulated for Concept D2. Both types of imperfection stimulate the deformation mode at the first limit point over a small area on one of the central arches as it is shown in figures 5.14(e) and 5.14(f). Six nodes were either loaded or deformed to generate the stimulating pattern.

The magnitude of each single load was chosen to be the amount of pressure acting over a standard finite element of the corresponding discretization which has an area of 5000 mm^2 .

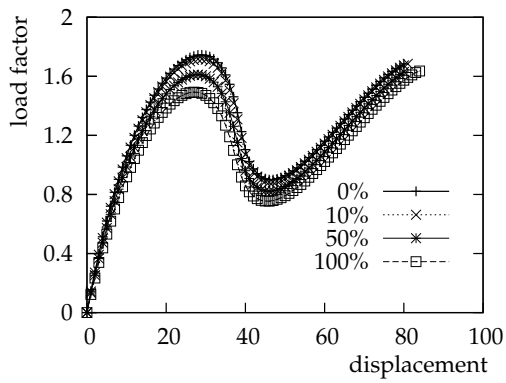
The magnitude of every displacement of the geometric imperfection was set to be equal to the thickness of the shell.

% of Imperfection	Load Imperfection		Geometric Imperfection	
	λ_c	Knock-down factor	λ_c	Knock-down factor
0	1.74	1.00	1.74	1.00
10	1.72	0.99	1.69	0.97
50	1.61	0.92	1.47	0.84
100	1.49	0.86	1.22	0.70

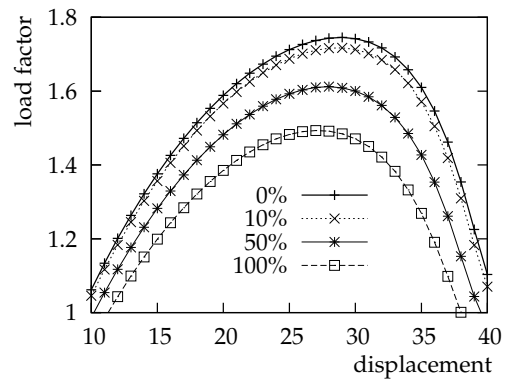
Table 5.5: Imperfections of Concept D2. Knock-down factors.

Table 5.5 contains critical loads and knock-down factors (ratio of critical loads of imperfect and perfect structure) for several fractions of the applied imperfection. Knock-down factors are generally used to give a safety factor to the critical load of perfect structures.

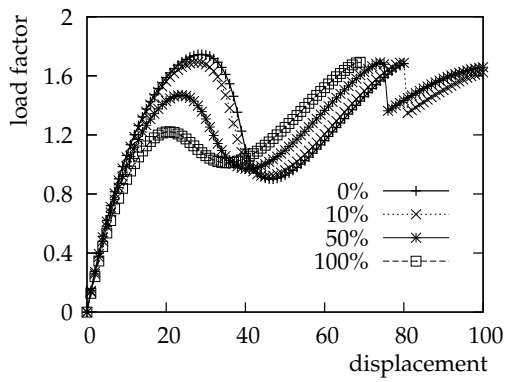
⁶The maximum displacement at the critical region due to only load imperfection was of 1.31 mm .



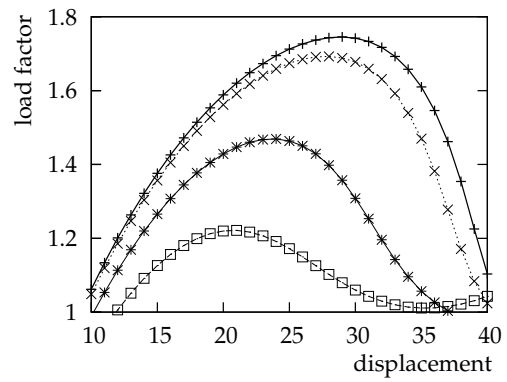
(a) Load imperfection.



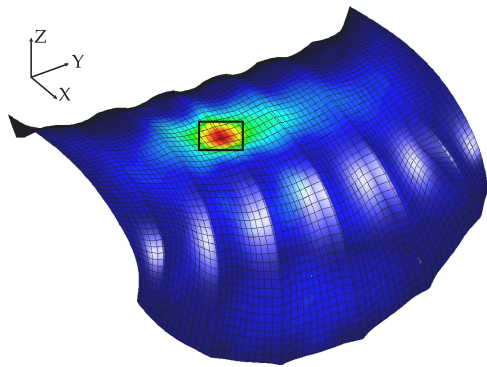
(b) Load imperfection, detail.



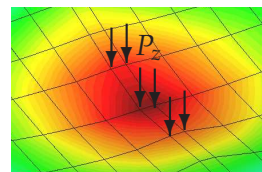
(c) Geometric imperfection.



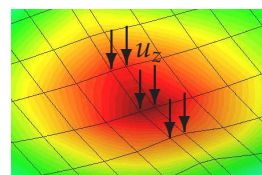
(d) Geometric imperfection, detail.



(e) Deformation mode for stimulating imperfections. Nonlinear displacements.



Load imperfection
 $6 \times (P_z = 600 \text{ N}).$
 $P_z = \text{load over one FE}_N$
 $= 5000 \text{ mm}^2 \times 0.12 \frac{\text{N}}{\text{mm}^2}.$



Geometric imperfection
 $6 \times (u_z = 6 \text{ mm}).$
 Shell-thickness = 6 mm.

(f) Load and geometric stimulating imperfections applied to six nodes along the critical arch.

Figure 5.14: Imperfection analysis of Concept D2.

Chapter 6

Sensitivity Analysis of Discrete Systems

6.1 Introduction

One of the fundamental components of the optimization model is the sensitivity analysis of structural responses. It provides information about the structural behavior resulting from modifying independent parameters in the optimization problem. This information is taken by the optimizer (mathematical optimization) to calculate the tendency towards structural improvement through selected indicators or structural responses known also as objective function and constraints.

The mathematical formulation of a general nonlinear optimization problem takes the form

$$\begin{aligned} \text{minimize : } & f(\mathbf{s}); & \mathbf{s} \in \mathbb{R}^n \\ \text{subject to : } & g_j(\mathbf{s}) = 0; & j = 1, \dots, m_e \\ & g_j(\mathbf{s}) \leq 0; & j = m_e + 1, \dots, m \\ & \mathbf{s}_l \leq \mathbf{s} \leq \mathbf{s}_u \end{aligned} \tag{6.1}$$

where f is the objective function and \mathbf{g} equality and inequality constraints. m_e is the number of equality constraints, whereas m stand for the total number of constraints. The optimal combination of the independent variables \mathbf{s} (optimization variables; see section 6.1.2) gives the minimum value of the objective function and at the same time fulfills selected constraints. The restrictions for upper and lower limits (bound restrictions \mathbf{s}_l and \mathbf{s}_u respectively) imposed to the variables are also known as side- or gage-constraints.

Constraints define the feasible domain of the solution according to the criteria defined by the designer who decides about the magnitude of the design window for the corresponding formulation. The objective function of an optimization problem consists of one or several responses which have to be improved. This improvement is expressed as a minimization (or maximization) of this function constructed out of the selected responses. Objective and constraints are not only a function of the optimization variables but in general also a function of state variables like the displacement field \mathbf{u} , which give information about the structural state due to applied boundary conditions. Evaluations and gradients (sensitivity analysis) of these responses allow gradient based optimizers to decide about the next variation of

optimization variables in the direction of improvement.

The quality of the influence of each variable over any significant quantity also guides the designer in the formulation of a well posed optimization problem. Variables which are not influencing the structural behavior can be removed from the formulation. In the same way, redundant constraints might be excluded as well.

Optimization algorithms might also improve the convergence of the solution and save computational effort by localizing the active set of constraints, since only this set of functions is important for the next improvement of the solution. Within this context, the authors in reference [HG92] suggest the existence of four basic steps in many optimization techniques: the selection of the set of active constraints, the determination of a search direction based on the objective function and the selected active constraints, the step size of the computed search direction, and the convergence step where the decision of performing a new step is taken. Mathematical programming theory for optimization can be found for instance in references [Ble90], [Pol97], [HG92] and [NW06].

An important issue regarding optimization algorithms is that they can be considerably affected by the diversity in magnitude of different type of design variables. In order to overcome this kind of problems, the usual technique is to scale all optimization variables, so that the variation of every one of them affects the solution in a similar degree by having a similar range of variations. The same procedure is applied for constraints, which are usually normalized by an allowable value.

Since objective and constraints are already discretized regarding the unknown structural parameters \mathbf{u} using finite elements, formulations regarding sensitivity analysis should be related to discrete systems. If sensitivities are computed before discretization, the field of study is called variational sensitivity, which has the advantage that the resulting sensitivity equations can be solved not only using the finite element method, but by means of other techniques [HG92]. Furthermore, the following sensitivity analysis techniques are based on linear static structural behavior.

After sensitivity analysis methods are introduced, semi-analytical sensitivities of stress and buckling constraints needed in the current optimization problem are briefly presented. No particular finite element formulation is included in sensitivity derivations.

6.1.1 Optimization Strategies

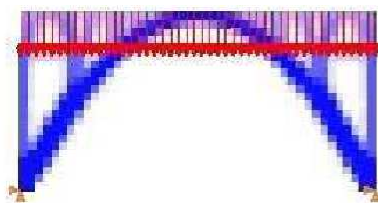
The type of design variable chosen for a particular optimization problem, will define the kind of optimization task to be solved. Four optimization tasks have been characterized in the following paragraphs (see also figure 6.1).

Sizing optimization Design variables in sizing optimization are cross-sectional quantities, while structural topology and geometry remain unchanged. In optimization problems of truss structures cross sectional areas are taken as design variables. Cross sectional thicknesses are generally used for structural components subjected to bending, as it is the case of bars, plates and shells.

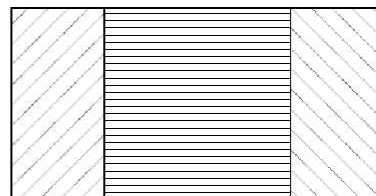
Fiber orientation optimization This kind of optimization searches for the optimal orientation of the material direction over structural members composed of anisotropic materials, like composites.

Shape optimization In shape optimization the geometry of the structure is modified to increase its performance according to the objective function. Topology and cross sectional dimensions remain unchanged. Geometrical quantities are usually used as design variables.

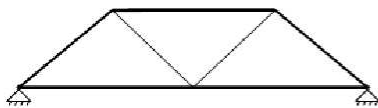
Topology optimization Topology optimization has to do with structural configuration where the material will be optimally distributed over a certain area or volume. A common task is to distribute a fixed area or volume in order to obtain the minimal structural compliance (strain energy). Shape variables are for instance densities over discrete regions.



Topology optimization



Fiber orientation optimization



Sizing optimization



Shape optimization

Figure 6.1: Optimization strategies. Source [Dao05].

In practice, optimization strategies are also combined, so that more than one type of optimization variables are included in the optimization model. In this way, the merged variable space can be exploited.

6.1.2 Variable Linking

In the formulation of an structural optimization problem there exist different types of variables which are necessary to be distinguished in order to understand the different relations between them. Throughout this work, three levels of variables are interconnected with each other, regarding shape optimization:

- ◇ Optimization variables \mathbf{s} , are normalized quantities updated by the optimizer at each optimization step towards improvement. They are the variables of the optimization model.
- ◇ Design variables \mathbf{y} , which belong to the selected geometrical model (design model) and consequently define the structural geometry. They are equivalent to the Cartesian coordinates of the geometrical coefficients that belong to the free form surface selected as variables during shape optimization or the thickness of the structure during sizing optimization.
- ◇ Structural variables \mathbf{x} are structural quantities modified during optimization and used by the structural analysis solver (variables of the structural analysis model) to compute structural response. They are equal to the discrete nodal coordinates that are modified during shape optimization or the individual thicknesses of the finite elements in sizing optimization.

In the context of shape optimization using CAD-based design elements, the relation between these three kind of variables is assigned by the optimization model and correspond to the linking level 3a in the classification given by Bletzinger [Ble90]. Here, \mathbf{y} are a linear combination of \mathbf{s} , and \mathbf{x} are a linear combination of \mathbf{y} . For instance, for a certain optimization variable s_k linked to design variables \mathbf{y}_l which are related to structural variables \mathbf{x}_m , the relation is written as (see equation 4.2)

$$\mathbf{x}_m = \mathbf{S}(u_m, v_m) = \Phi_l(u_m, v_m) \underbrace{[\mathbf{P}_l^0 + \mathbf{n}_l s_k]}_{\mathbf{y}_l}, \quad (6.2)$$

where \mathbf{n}_l constitute the linking matrix \mathbf{N} of linear relations between optimization and design variables (see equation 6.32). Vector \mathbf{n}_l could represent for instance pre-defined moving directions (like normal to surface direction), symmetric/anti-metric considerations as well as linear combinations, change of basis, projection or continuity relations [BRKR93]. Φ_l are the basis functions of the free form surface and establish the linear relation between structural and design variables. They constitute the linking matrix Φ (see equation 6.32). Parameters u_m and v_m are the surface parameters associated to the structural variable \mathbf{x}_m , and \mathbf{P}_i^0 is the initial position of the corresponding geometrical coefficient which remains constant during optimization.

Variable scaling is applied to the optimization variables in order to avoid related convergence problems of gradient based optimizers. One way of doing this, is to set similar bounds for all optimization variables by using the bounds of the corresponding linked design variables (see [Hör04b]).

6.2 Finite differences Approximation

Finite difference approximation is the simplest approach for calculating derivatives of responses with respect to optimization variables. The simplicity of the implementation contrasts with the high computational cost of the technique when the number of optimization variables is large. The method requires several solutions of the system of equations (6.6), with the consequent computation of the inverse of \mathbf{K} by means of decomposition techniques. The number of times the matrix \mathbf{K} must be inverted depends on the finite different technique that is been used: two times for each optimization variable s_i when using first order approximations like forward-difference

$$\frac{d\varphi}{ds_i} \approx \frac{\Delta\varphi}{\Delta s_i} = \frac{\varphi(s_i + \Delta s_i) - \varphi(s_i)}{\Delta s_i}, \quad (6.3)$$

three times when using second order approximations like central-difference

$$\frac{d\varphi}{ds_i} \approx \frac{\Delta\varphi}{\Delta s_i} = \frac{\varphi(s_i + \Delta s_i) - \varphi(s_i - \Delta s_i)}{2\Delta s_i}, \quad (6.4)$$

and even more for higher order approximations. Therefore, first and second order approximations are commonly used in practice.

When using finite differences the selection of an appropriate step size (step size dilemma) is decisive in the elimination of accuracy problems, which are associated to two sources of errors: truncation and condition errors (for details see [IHA85]). The truncation error occurs by neglecting higher order terms in the Taylor series expansion of the perturbed function, whereas condition errors arise due to the numerical evaluation of the function, where the round-off error due to computer accuracy might become important when the equilibrium equation (6.6) is solved by a lengthy or ill-conditioned numerical process [HG92].

6.3 Analytical Sensitivity Analysis of Discrete Systems

Besides the accuracy of the results, analytical sensitivities become more efficient than numerical approximations when the number of optimization variables \mathbf{s} increases. The analytical methodology takes advantage of the already decomposed stiffness matrix of the system.

To evaluate the sensitivity analysis of a structural response, a discretized function φ depending on optimization variables \mathbf{s} and state (response) variables \mathbf{u} (displacement field) is considered. It is assumed that a modifications of optimization variables will also modify the structural configuration together with its stiffness, and as a consequence produces an influence in the response \mathbf{u} . The sensitivities of the function $\varphi(\mathbf{s}, \mathbf{u}(\mathbf{s}))$ with respect to the variables \mathbf{s} are obtained by taking total derivatives

$$\frac{d\varphi}{ds} = \frac{\partial\varphi}{\partial\mathbf{s}} + \frac{\partial\varphi}{\partial\mathbf{u}} \frac{d\mathbf{u}}{ds} \quad (6.5)$$

The total derivatives of φ include an explicit part which is usually easy to obtain or equal to zero and an implicit term through the dependence of \mathbf{u} . The total derivatives $d\mathbf{u}/ds$ in the second component cannot be obtained directly and have to be calculated using the discretized formulation of equilibrium equations, which are linear about the displacement field \mathbf{u}

$$\mathbf{K}\mathbf{u} = \mathbf{R}; \quad \mathbf{u} = \mathbf{K}^{-1}\mathbf{R} \quad (6.6)$$

Taking derivatives with respect to the optimization variables \mathbf{s} in equation (6.6), and solving for $d\mathbf{u}/ds$, the following expression is obtained

$$\frac{d\mathbf{u}}{ds} = \mathbf{K}^{-1} \left(\frac{d\mathbf{R}}{ds} - \frac{d\mathbf{K}}{ds} \mathbf{u} \right) \quad (6.7)$$

where the term in parenthesis is called the pseudo load vector

$$\mathbf{R}^* = \frac{d\mathbf{R}}{ds} - \frac{d\mathbf{K}}{ds} \mathbf{u}. \quad (6.8)$$

The pseudo load vector is the load that have to be applied to the structure to obtain the displacement sensitivity field $d\mathbf{u}/ds$ in equation (6.7).

The total derivative of the response φ , is computed by combining equations (6.5) and (6.7) to obtain

$$\frac{d\varphi}{ds} = \frac{\partial\varphi}{\partial\mathbf{s}} + \frac{\partial\varphi}{\partial\mathbf{u}} \mathbf{K}^{-1} \left(\frac{d\mathbf{R}}{ds} - \frac{d\mathbf{K}}{ds} \mathbf{u} \right) \quad (6.9)$$

Equation (6.9) can be solved by two different methods, direct and adjoint, depending on the sequence the implicit derivatives are solved.

6.3.1 Direct Method

Also called design space method, the direct method solves first for $d\mathbf{u}/ds$ using equation (6.7). This system of equations has to be solved $n \cdot n_{LC}$ times, where n is the number of optimization variables \mathbf{s} and n_{LC} is the number of load cases. Afterward, the dot product of this result with the vector $\partial\varphi/\partial\mathbf{u}$ is calculated in order to obtain the explicit term in the derivation of φ in equation (6.5). The vector $\partial\varphi/\partial\mathbf{u}$ has to be computed for each structural response φ .

6.3.2 Adjoint Method

Also called state space method, the adjoint method computes the implicit term of equation (6.9) using a different sequence of matrix operations, leading to a different computational effort. This difference becomes advantageous compared to the direct method when the

number of optimization variables is significantly large with respect to the number of active constraints.

This approach defines an adjoint vector λ which is the solution of the system

$$\mathbf{K}\lambda = \frac{\partial \varphi}{\partial \mathbf{u}} \quad (6.10)$$

that has to be solved for the objective and the active set of constraints. The solution of (6.10) ($\lambda = (\partial \varphi / \partial \mathbf{u}) \mathbf{K}^{-1}$, using the symmetry of \mathbf{K}) is finally multiplied by the pseudo load vector to obtain

$$\frac{d\varphi}{ds} = \frac{\partial \varphi}{\partial s} + \lambda \left(\frac{d\mathbf{R}}{ds} - \frac{d\mathbf{K}}{ds} \mathbf{u} \right) \quad (6.11)$$

The computational effort of each method and consequently the selection of one of them for the particular problem, is thus driven by the number of times the corresponding system of equations involving the global stiffness \mathbf{K} has to be solved. In case the number of optimization variables times the number of load cases is larger than the number of objective plus active constraints ($n \cdot n_{LC} > n_\varphi$), the adjoint method would be the better choice. Otherwise, the direct method should be the alternative.

The task that is left is the sensitivity computation of the global stiffness matrix and the vector of external forces in order to calculate the pseudo load vector of equation (6.8). Both sensitivities are needed for the direct and adjoint approaches. Their computation is performed at element level, so that only affected elements depending on the considered optimization variable are assembled into the global sensitivity matrix

$$\frac{d\mathbf{K}}{ds} = \sum_{i=1}^{nelem} \frac{d\mathbf{k}_i^e}{ds} \quad (6.12)$$

where *nelem* is the total number of elements.

This computation can be done analytically, where the sensitivities of equation (6.12) have to be calculated for every specific finite element. Sensitivities of each component involved in the computation of the stiffness matrix

$$\mathbf{k}^e = \int_{\Omega^\theta} \mathbf{B}^T \mathbf{C} \mathbf{B} \det(\mathbf{J}) d\Omega^\theta \quad (6.13)$$

have to be considered as it is the case for shape variables. In equation (6.13) $\det(\mathbf{J})$ stands for the determinant of the Jacobian [Hug00].

For a standard isoparametric element, the sensitivities of \mathbf{k}^e are computed using

$$\frac{d\mathbf{k}^e}{ds} = \int_{\Omega^\theta} \left(\frac{d\mathbf{B}^T}{ds} \mathbf{C} \mathbf{B} \det(\mathbf{J}) + \mathbf{B}^T \mathbf{C} \frac{d\mathbf{B}}{ds} \det(\mathbf{J}) + \mathbf{B}^T \mathbf{C} \mathbf{B} \frac{d(\det(\mathbf{J}))}{ds} \right) d\Omega^\theta \quad (6.14)$$

which involves a higher programming effort. In cases where the constitutive law depends on \mathbf{s} , sensitivities of the material matrix \mathbf{C} have to be considered as well. Reference [Cam04] for instance, shows analytical sensitivities of a shell element with Reissner-Mindlin Kinematics with respect to shape variables.

For problems with a large number of discrete displacement variables \mathbf{u} the analytical sensitivity approach is more efficient than finite difference approximation, since for the computation of the sensitivities for each optimization variable at every optimization step the global stiffness \mathbf{K} has been already factorized for the computation of vector \mathbf{u} in equation (6.6).

The second alternative that can be chosen at this point is to approximate sensitivities of element stiffness matrix and load vector by means of finite differences. This approach is called semi-analytical sensitivity analysis [HG92] which is advantageous when stiffness sensitivities are too complex, as it is the case when shape variables are included in the optimization model, and when the derivation has to be done for many element types.

6.4 Semi-Analytical Sensitivity Analysis of Discrete Systems

This approach combines the advantages of reducing complexity for sensitivity calculation of elemental stiffness matrices

$$\frac{d\mathbf{K}}{ds} = \sum_{i=1}^{nelem} \frac{d\mathbf{k}_i^e}{ds} \approx \sum_{i=1}^{nelem} \frac{\Delta\mathbf{k}_i^e}{\Delta s} \quad (6.15)$$

and saving computational costs by factorizing the global stiffness \mathbf{K} only once for each structural configuration. Besides the approximation of the components of the pseudo load vector, all other sensitivities in equation (6.9) are obtained analytically. The number of finite elements involved in the calculation of equation (6.15) in case of using design elements in the construction of the geometrical model (chapter 4) will depend on how many geometrical coefficients (design variables) are linked to the current optimization variable s (see section 6.1.2) and how large is the region of influence related to the linked geometrical coefficients. This fact will reduce the computational effort by computing only the necessary elemental sensitivities. For B-splines, as explained in section 4.3.2.2, the modification of a control point $P_{i,j}$ affects the surface over the area $[u_i, u_{i+p+1}) \times [v_j, v_{j+p+1})$ in the parametrical space (see also section 6.6).

Although the semi-analytical approach uses the advantage of the already decomposed stiffness matrix as it is the case for analytical sensitivities, accuracy errors arise due to approximations (see section 6.2).

In some cases there is another source of error that increases with refinement of the finite element mesh and applies for shape optimization variables. The source of error arises with

respect to the rigid body rotation behavior of the approximated stiffness matrix derivative [BFD08]. The finite elements that are affected are the ones whose stiffness depends of different powers of the independent variables as it is the case of elements including bending stiffness [HG92] [Ble04]. The error becomes even more important with the increment of slenderness and thickness [HG92]. References [OR91], [HG92] and [BFD08] give examples where this behavior is shown. There exist several solutions to the problem. Some of them are listed in reference [BFD08]. The authors in [HG92] suggest the use of central difference approximation of the stiffness matrix, which implies an increment in the computational cost. In reference [Ora96] the author proposes an improved semi-analytical sensitivity analysis based on the lemma of Carl Neumann [Hör01]. In reference [BFD08], a method for the computation of correction factors based on product spaces of rigid body rotation vectors is presented, where the element stiffness matrix is modified by this factors in order to obtain "exact" sensitivities. This method is applicable to all kind of finite elements without major modifications. It is important to mention that the different studies using beam and shell elements in reference [BFD08] demonstrate that the accuracy problems of semi-analytical sensitivities depends on the kinematic assumptions of the finite element formulation. The errors with respect to the exact solution are more important for Euler-Bernoulli and Kirchhoff formulations than in Timoshenko and Reissner-Mindling kinematics and depends on the magnitude of the ratio between perturbation and element length $\Delta s/L_e$.

6.5 Objective and Constraints

Generally, objective and constraints of shape optimization problems are non-linear with respect to the independent variables \mathbf{s} . This is not the exception for the optimization formulation developed in this work. The considered objective function is the total weight of the structure which has to be minimized

$$f = \int_{\Omega} \rho dv \quad (6.16)$$

The constraints included in the optimization problems of chapter 7 are related to stress and linearized prebuckling, which restrict the strength of the material and the critical load respectively.

6.5.1 Stress Constraint

The von Mises stress is restricted at the upper and lower fibers of the shell using the following mathematical formulation

$$g_{\sigma_v} = \frac{\sigma_v}{\sigma_a} - 1 \leq 0 \quad (6.17)$$

where the von Mises Stress in the plane of the elements is given by [Oeh98]

$$\sigma_v = \sqrt{\sigma_x^2 + \sigma_y^2 - \sigma_x \sigma_y + 3\tau_{xy}^2}. \quad (6.18)$$

σ_a is the allowable value. Stress components in the plane of the element (membrane stresses) referred to the local Cartesian coordinate system are obtained from the relation

$$\boldsymbol{\sigma} = \mathbf{CB}(\mathbf{s}) \mathbf{u}(\mathbf{s}) \quad (6.19)$$

where \mathbf{C} is the material matrix and \mathbf{B} relates strain and displacements of the discretized system

$$\boldsymbol{\varepsilon} = \mathbf{B}(\mathbf{s}) \mathbf{u}(\mathbf{s}). \quad (6.20)$$

The material matrix \mathbf{C} for isotropic material regarding in-plane stresses takes the form

$$\mathbf{C} = \frac{E}{1-\nu^2} \begin{bmatrix} 1 & \nu & 0 \\ \nu & 1 & 0 \\ 0 & 0 & \frac{1}{2(1-\nu)} \end{bmatrix}. \quad (6.21)$$

The sensitivity of the stress field with respect to the optimization variables is written as (see eq. 6.5)

$$\begin{aligned} \frac{d\boldsymbol{\sigma}}{d\mathbf{s}} &= \frac{\partial \boldsymbol{\sigma}}{\partial \mathbf{s}} + \frac{\partial \boldsymbol{\sigma}}{\partial \mathbf{B}} \frac{d\mathbf{B}}{d\mathbf{s}} + \frac{\partial \boldsymbol{\sigma}}{\partial \mathbf{u}} \frac{d\mathbf{u}}{d\mathbf{s}} \\ &= \mathbf{C} \frac{d\mathbf{B}}{d\mathbf{s}} \mathbf{u} + \mathbf{CB} \frac{d\mathbf{u}}{d\mathbf{s}} \end{aligned} \quad (6.22)$$

Finally, the sensitivities of the von Mises stress with respect to optimization variables is computed as

$$\frac{d\sigma_v}{d\mathbf{s}} = \frac{\partial \sigma_v}{\partial \mathbf{s}} + \frac{\partial \sigma_v}{\partial \boldsymbol{\sigma}} \frac{d\boldsymbol{\sigma}}{d\mathbf{s}} \quad (6.23)$$

The first term, the explicit one, vanishes since σ_v does not depend explicitly on \mathbf{s} . First and second components of the second term are calculated using equations (6.24) and (6.22) respectively.

$$\frac{\partial \sigma_v}{\partial \boldsymbol{\sigma}} = \frac{1}{2\sigma_v} \begin{bmatrix} 2\sigma_x - \sigma_y & 2\sigma_y - \sigma_x & 6\tau_{xy} \end{bmatrix} \quad (6.24)$$

6.5.2 Buckling Constraint

The linear buckling constraint

$$g_\lambda = \frac{\lambda}{\lambda_a} - 1 \leq 0 \quad (6.25)$$

restricts the factor λ that estimates the buckling load at which the corresponding buckling mode $\boldsymbol{\phi}$ occurs. The values of λ and $\boldsymbol{\phi}$ are obtained from the eigenvalue problem

$$(\mathbf{K}_e + \lambda \mathbf{K}_g) \boldsymbol{\phi} = 0 \quad (6.26)$$

One of the important assumptions of the method is that the results are not significantly influenced by the displacement field (see section 5.3). The matrix \mathbf{K}_e is the elastic stiffness of the system and \mathbf{K}_g is the global geometrical stiffness (see also section 5.2.1.4).

The sensitivity of eigenvalues with respect to optimization variables \mathbf{s} is obtained by taking total derivatives in equation (6.26) and premultiplying the result by the eigenvector $\boldsymbol{\phi}^T$

$$\boldsymbol{\phi}^T \frac{d\lambda}{ds} \mathbf{K}_g \boldsymbol{\phi} + \boldsymbol{\phi}^T \left(\frac{d\mathbf{K}_e}{ds} + \lambda \frac{d\mathbf{K}_g}{ds} \right) \boldsymbol{\phi} + \boldsymbol{\phi}^T (\mathbf{K}_e + \lambda \mathbf{K}_g) \frac{d\boldsymbol{\phi}}{ds} = 0 \quad (6.27)$$

Solving for the sensitivities $d\lambda/ds$ and using the symmetry of \mathbf{K}_e and \mathbf{K}_g ($\boldsymbol{\phi}^T (\mathbf{K}_e + \lambda \mathbf{K}_g) = 0$) we have [HG92]

$$\frac{d\lambda}{ds} = - \frac{\boldsymbol{\phi}^T \left(\frac{d\mathbf{K}_e}{ds} + \lambda \frac{d\mathbf{K}_g}{ds} \right) \boldsymbol{\phi}}{\boldsymbol{\phi}^T \mathbf{K}_g \boldsymbol{\phi}} \quad (6.28)$$

where $\boldsymbol{\phi}$ is the eigenvector related to λ .

The normalization equation for eigenvectors

$$\boldsymbol{\phi}^T \mathbf{K}_g \boldsymbol{\phi} = 1 \quad (6.29)$$

is introduced to simplify calculations. \mathbf{K}_g is symmetric and positive definite assuring a well definition of the solution in (6.28).

6.6 Sensitivities of Free Form Surfaces

In case analytical sensitivities of objective and constraints are to be computed, additional sensitivities of discrete nodal coordinates w.r.t optimization variables have to be included. From equation (6.2), the total derivative of the coordinate i , which belongs to node \mathbf{x}_m , with respect to the optimization variables s_k is computed as

$$\frac{dx_m^i}{ds_k} = \sum_{l=1}^l \left(\sum_{j=1}^3 \frac{\partial x_m^i}{\partial y_l^j} \frac{dy_l^j}{ds_k} \right) = \sum_{l=1}^l \Phi_l(u_m, v_m) \sum_{j=1}^3 n_l^j \quad (6.30)$$

where l is equal to all design variables linked to s_k .

In the computation of sensitivities, the piece-wise property of B-splines is also considered. Thus, by modifying a design variable y_l , the affected nodal coordinates are the ones whose surface parameters are located within the region of influence shown in figure 6.2.

For instance the analytical sensitivities of a structural response φ which also depends on structural variables \mathbf{x} and state variables \mathbf{u} , $\varphi(\mathbf{s}, \mathbf{x}(\mathbf{s}), \mathbf{u}(\mathbf{x}(\mathbf{s})))$ are given by

$$\frac{d\varphi}{ds} = \frac{\partial \varphi}{\partial \mathbf{s}} + \frac{\partial \varphi}{\partial \mathbf{x}} \frac{d\mathbf{x}}{ds} + \frac{\partial \varphi}{\partial \mathbf{u}} \underbrace{\frac{\partial \mathbf{u}}{\partial \mathbf{x}} \frac{d\mathbf{x}}{ds}}_{\frac{d\mathbf{u}}{ds}} \quad (6.31)$$

The total derivatives $d\mathbf{x}/ds$ which are present in the last two terms of equation (6.31) are computed as the product of the linking matrices

$$\frac{d\mathbf{x}}{ds} = \boldsymbol{\Phi} \mathbf{N} \quad (6.32)$$

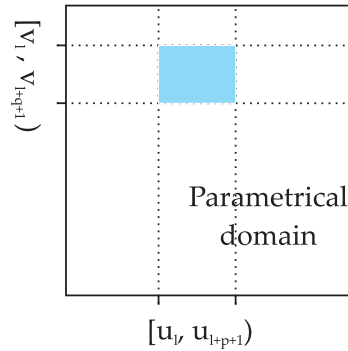


Figure 6.2: Affected region by modifying a design variable y_l .

as explained by equation (6.30).

6.7 Test Example for Numerical Sensitivities

Figure 6.3 shows a finite element mesh and a geometrical model of the extended version of the pressurized bulkhead. This design was selected to check the accuracy of the semi-analytical sensitivities with respect to the overall finite difference approximation as shown in figure 6.4. Numerical approximations of sensitivities for objective and constrains (overall finite difference) were calculated by means of forward differences, whereas the numerical approximations for the sensitivities of the stiffness matrix (SA sensitivities) was done using central differences, in order to reduce the error regarding shape variables and bending stiffness as explained in section 6.4. This error is no longer visible for sensitivities of the objective function in the range of a step size Δs between $1E - 5$ and $1E - 9$ (see fig. 6.4(a)). It reduces to about 1.1% for the stress constraint over the same range of Δs for the corresponding optimization variable (see fig. 6.4(b)). The location of the selected finite element for this constraint is indicated in figure 6.3(a) .

The sensitivities shown in figure 6.4 were calculated with respect to two different optimization variables. Figure 6.3(d) shows the control points which are linked to each optimization variable. The first optimization variable (OV1) is linked to control points which run along both central arches, whereas the second optimization variable (OV2) is linked to geometrical coefficients related to the central surface.

Figures 6.3(b) and 6.3(c) show the finite element mesh, where the elements that have been removed are the ones affected by control point 30 and OV2 respectively. An element is affected by a control point, if one of its nodes is found to be in the region of influence of this control point, as shown in figure 6.2 (see also section 4.3.2.2).

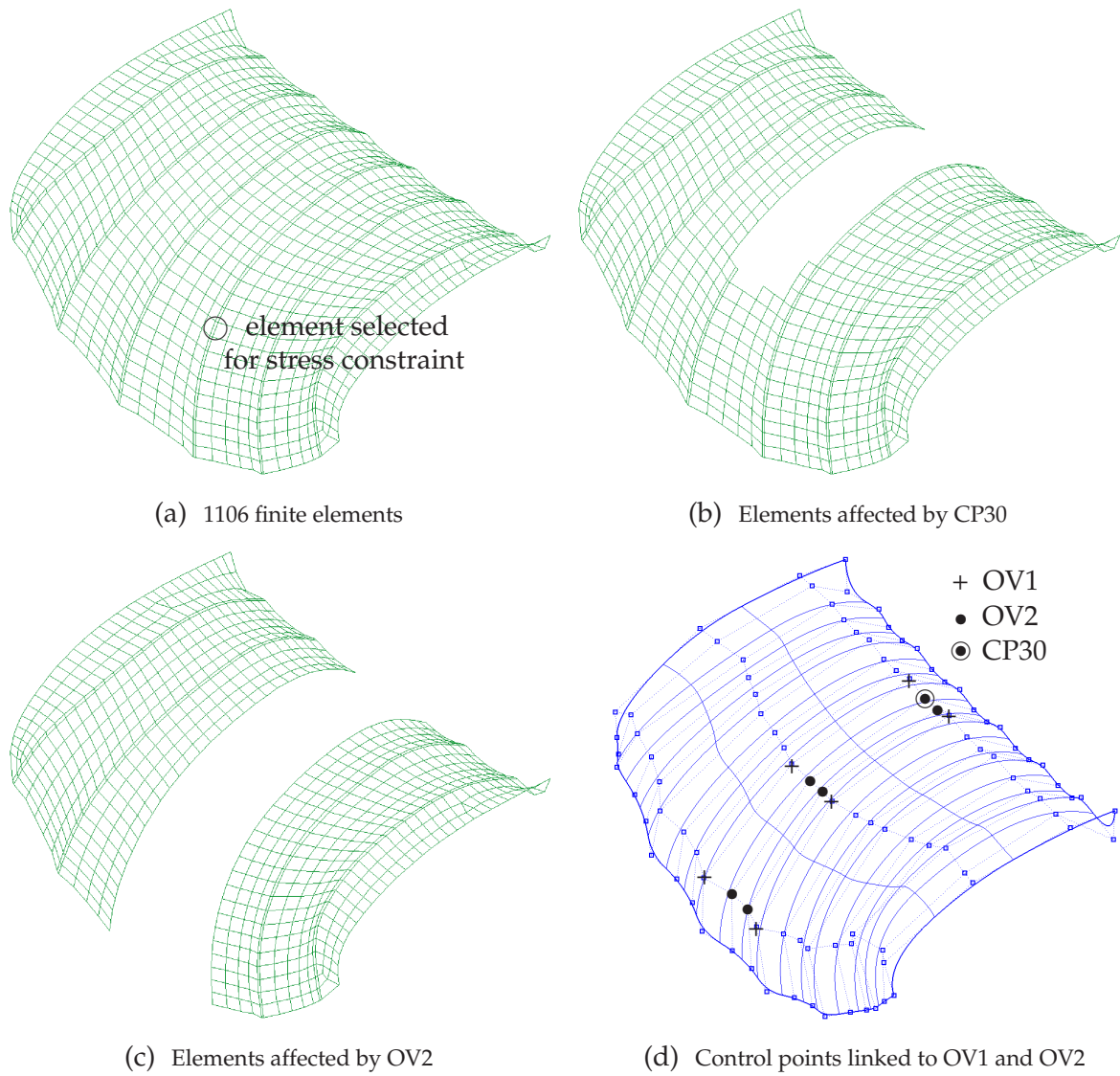
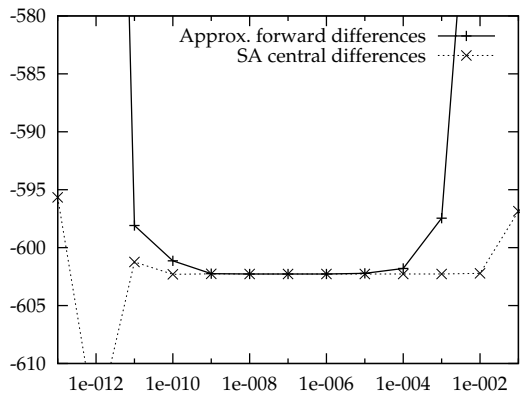
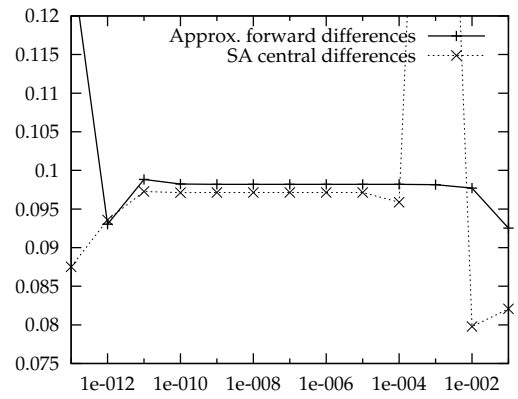


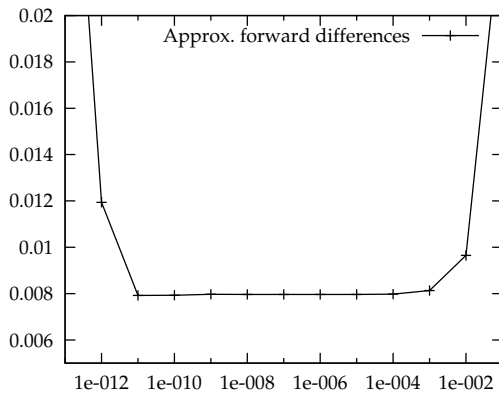
Figure 6.3: Regions of influence and control point network (20x5).



(a) Objective function (weight), OV2



(b) Stress constraint, OV1



(c) Stability constraint, OV2

Figure 6.4: Sensitivity approximations of structural responses w.r.t. opt. variables.

Chapter 7

Applications

The present chapter includes numerical examples of the design process explained in chapter 1. One of the geometrical configurations of the extended bulkhead, computed using form finding in chapter 3, and verified using geometrically nonlinear analysis in chapter 5, is taken as example to go through all stages of the design process, including optimization and non-linear verification.

The following optimization formulations include shape, sizing and a combination of both strategies. Geometric models for shape optimization are selected from fitted surfaces generated as explained in chapter 4.

7.1 General Parameters for Numerical Examples

Table 7.1 includes values of general parameters for the examples presented in the following sections regarding: material properties, objective and constraints for optimization, as well as loading and boundary conditions.

Material model	Isotropic
Elasticity Modulus	45000 N/mm^2
Poisson ratio	0.3
Density	$1.6 \times 10^{-6} \text{ kg/mm}^3$
Objective	Total weight
Constraint 1	Allowable LPB of 3.0
Constraint 2	Allowable stress of 200 N/mm^2
Pressure load	0.12 N/mm^2
Support along boundary	x, y and z displacements restricted

Table 7.1: General parameters for applications

7.2 Form Finding and Geometrical Model

Figure 7.1 shows the equilibrium shape calculated using form finding over the selected model for optimization, concept D2 (see figures 3.2(b) and 5.6(c)).

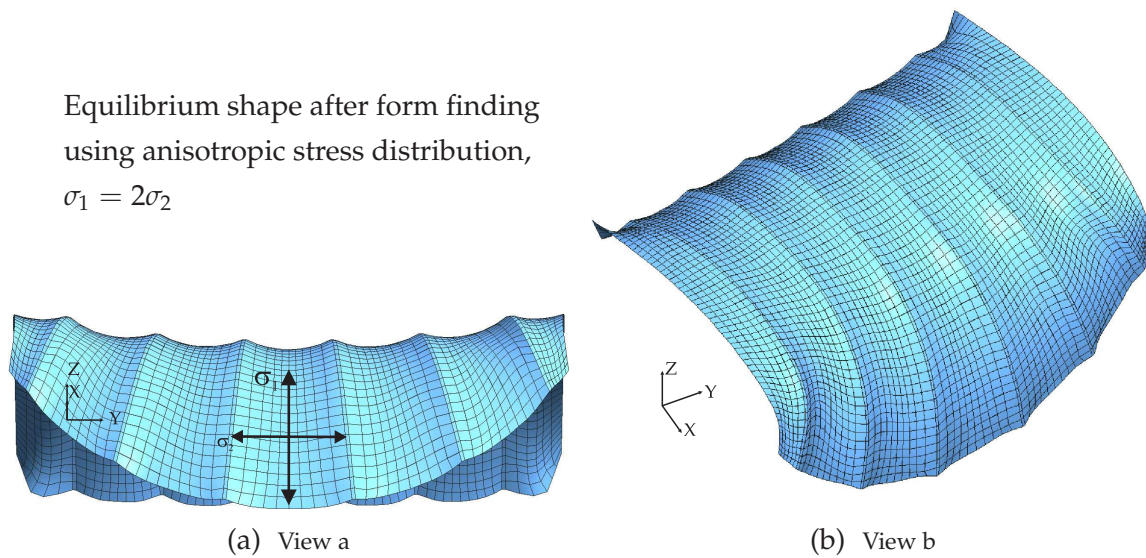


Figure 7.1: Concept D2. Equilibrium shape.

The feasibility of the resulting configuration was verified by a geometrically nonlinear finite element simulation. Figure 7.2 shows a critical load factor higher than 1.7 at which the structure becomes unstable (see also figure 5.6).

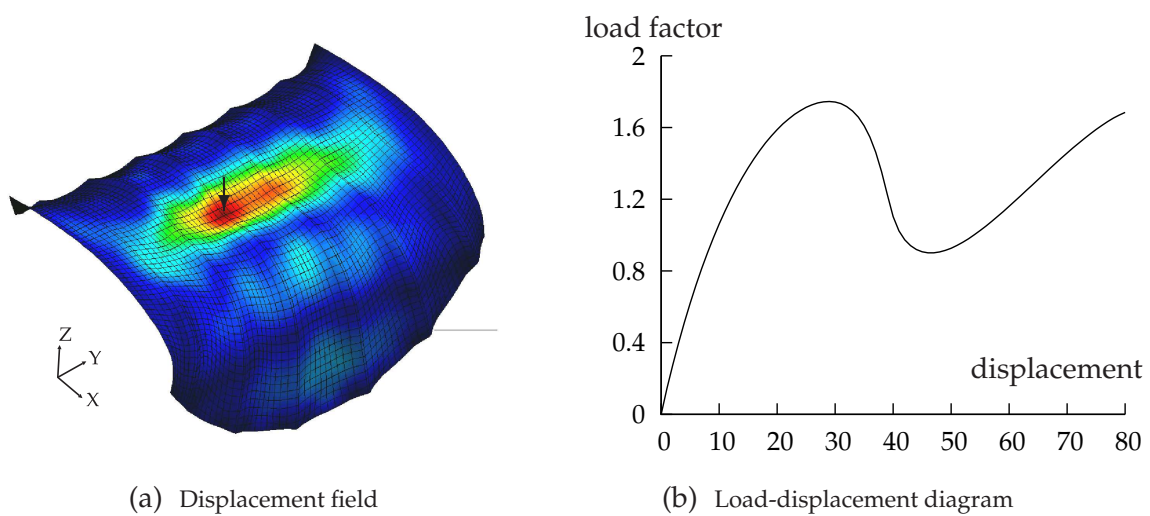


Figure 7.2: Non-linear analysis concept D2. Initial design.

7.2.1 Generation of Geometrical Models - Surface fitting

This subsection contains several examples of approximated B-spline surfaces generated from 2 different base surfaces. Finally, a base surface, and an approximated one are selected as geometrical models for optimization.

Both figures 7.3 and 7.4 contain three approximated surfaces for concept D2 obtained from two different base surfaces. Both base surfaces on figures 7.3(a) and 7.4(a) were calculated using bilinear interpolation (section 4.4) from a network of 20x5 and 20x7 nodes respectively. The corresponding surface parameters of the selected data and knot vectors were calculated using the chord length method and the averaging technique respectively (equations 4.14 and 4.24). All approximated surfaces have uniform knot vectors. Surface-divisions on the figures represent knot values. Mean/maximum errors and standard deviations w.r.t nodal data are also indicated.

For all geometrical models, one row of control points in direction u runs along the top of the arches, whereas for every inner surface (between two arches), two rows of CP also in u direction, control their shape. The approximation accuracy of each surface depends on: the selected polynomial degree along both parametric directions, the total number of control points, the surface parameters for every data point, and selected knot vectors.

Base surface of figure 7.4(a) and approximated surface of figure 7.4(c) are chosen as geometrical model for shape optimization. Even though both surfaces were generated from the same nodal data and have the same amount of control points, the different methodologies used for their computation produce a different distribution of control points and knot spans, leading to different (even if slightly) geometrical representations.

7.2.2 Modification in the Number of Geometrical Coefficients

This section contains two examples of approximated surfaces generated by surface fitting where the number of Geometrical coefficients is modified along certain regions of the model (see section 4.4.6). The purpose of these examples, is to only show the effects of such modifications, since none of the resulting surfaces is used later in shape optimization.

Figures 7.5 and 7.6 show examples of knot insertion and removal for concept D2 along the parametrical direction u . Initial surfaces were taken from figures 7.4(c) and 7.4(d) respectively.

For knot insertion, knot values 0.3 and 0.7 were inserted into the existing knot vector $\mathbf{U} = \{0, 0, 0, 0.2, 0.4, 0.6, 0.8, 1, 1, 1\}$. For knot removal, knots 0.286 and 0.714 were extracted from the existing knot vector $\mathbf{U} = \{0, 0, 0, 0.143, 0.286, 0.428, 0.571, 0.714, 0.857, 1, 1, 1\}$. For each of the inserted knots, two new CP replace one of the old ones (rows 1, 2, 4, 6 and 7 of the initial representation remain unchanged). As expected, the shape of the surface is not

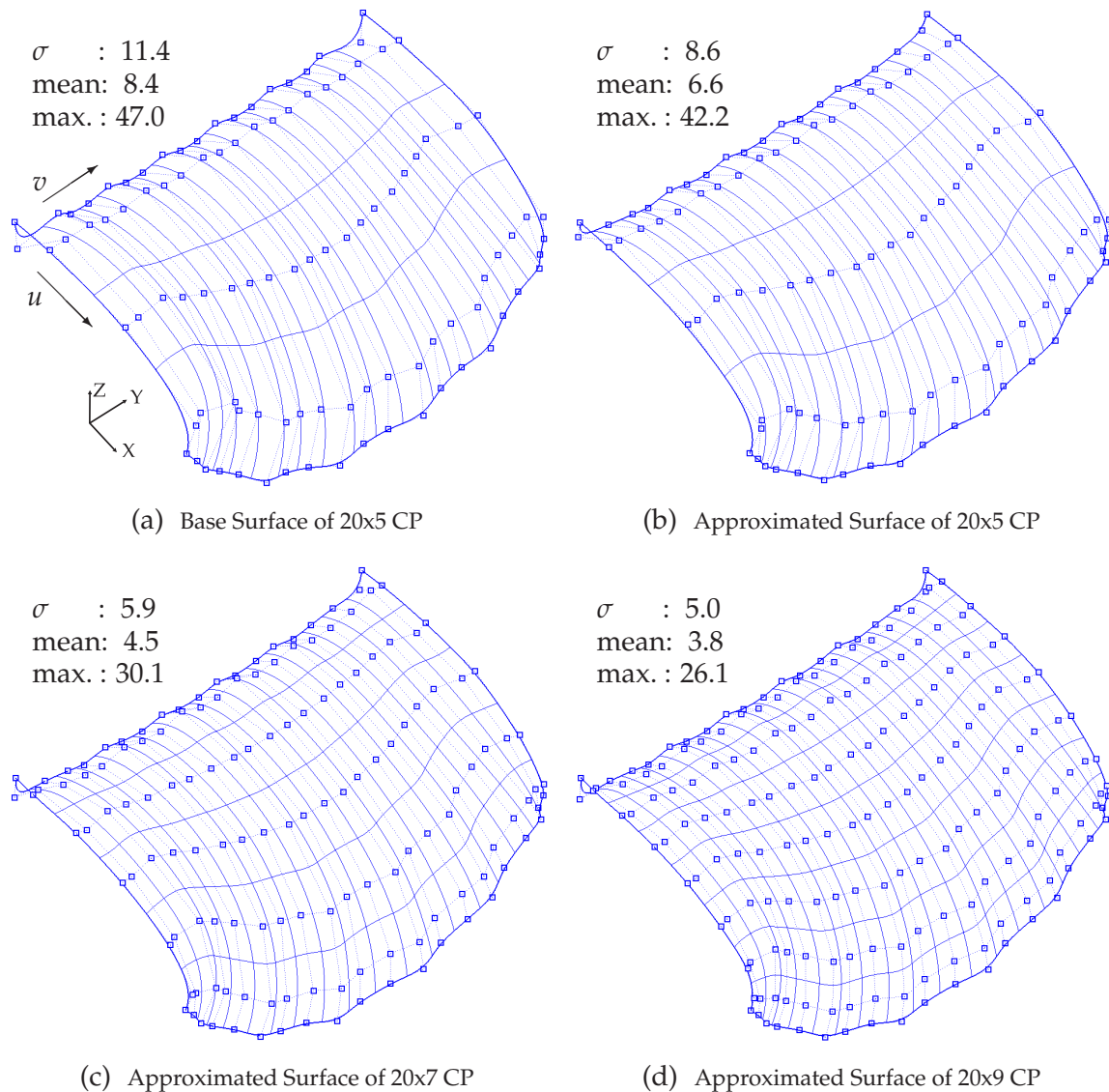


Figure 7.3: Approximated surfaces, degree 2x2. Base surface of 20x5 CP. Approx. errors.

modified.

Knot removal is usually associated with an error, since now with less geometrical coefficients the new surface has to approximate the old geometry. This fact is observed when comparing errors of surfaces before and after knot removal on figure 7.6. For this example, every time a knot is removed, three rows of CP are replaced by two new rows as explained in section 4.4.6.2.

Knot insertion and knot removal are local operations which can be used to modify geometrical models by refining or decreasing the number of CP over smaller regions of higher interest for the designer. Nevertheless, these operations cannot modify parametric sub-regions, due to the nature of B-Splines (inserting/removing a single knot, for instance in \mathbf{U} , will modify the surface along the whole parametric direction v).

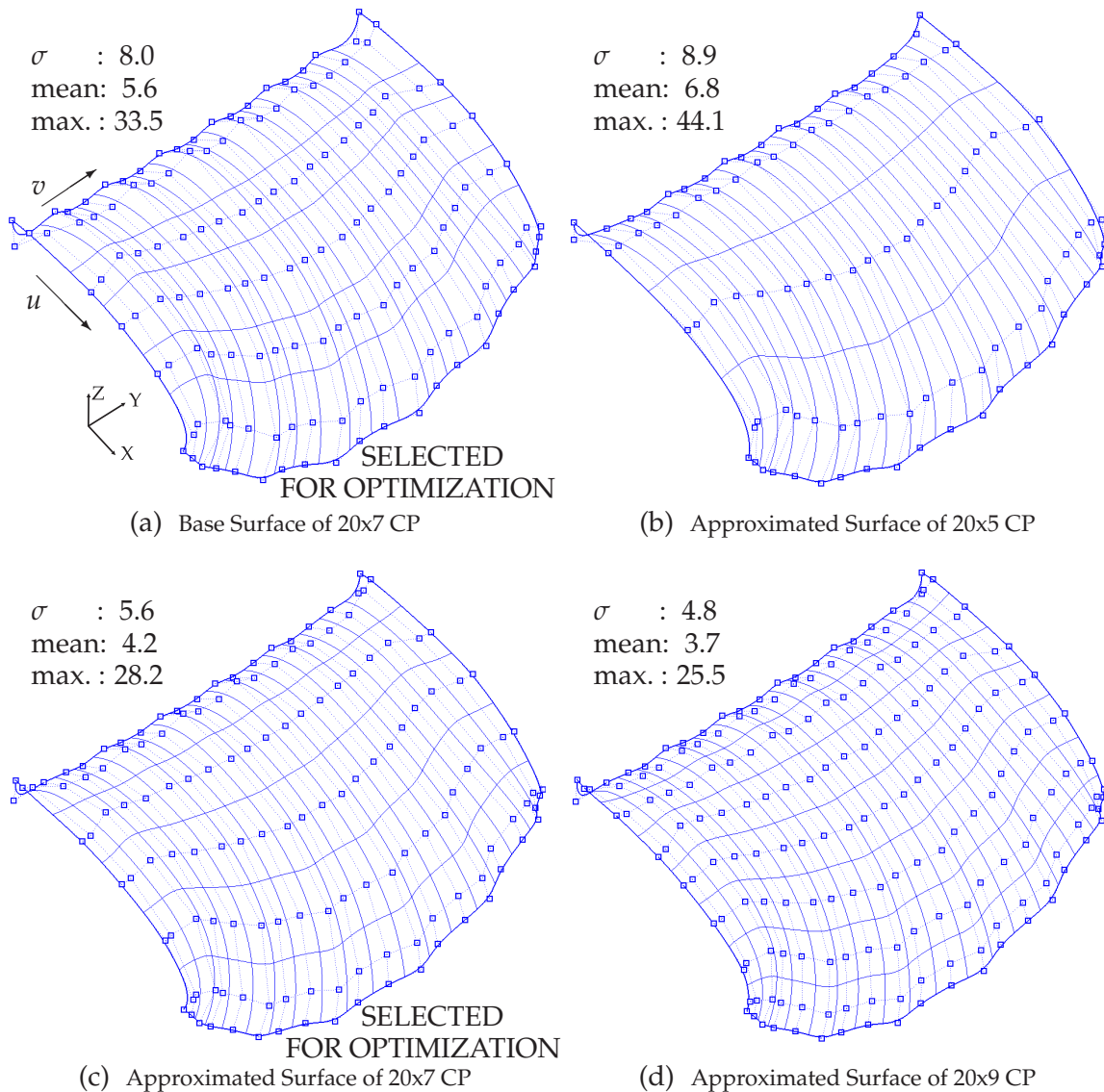


Figure 7.4: Approximated surfaces, degree 2x2. Base surface of 20x7 CP. Errors.

In case the total number of CP has to be globally modified, fitting a new surface over the initial data-set would be the most reasonable solution, since now the whole cloud of CP supports the approximation (compare approximation errors between fig. 7.6(b) and fig. 7.4(c)).

7.3 Optimization and Geometrically Non-Linear Verification

This section calculates the final optima of Concept D2 by using both selected geometrical models shown in figures 7.4(a) and 7.4(c), base and approximated surface respectively. First, specifications are provided regarding: variable linking for modifications in shape and

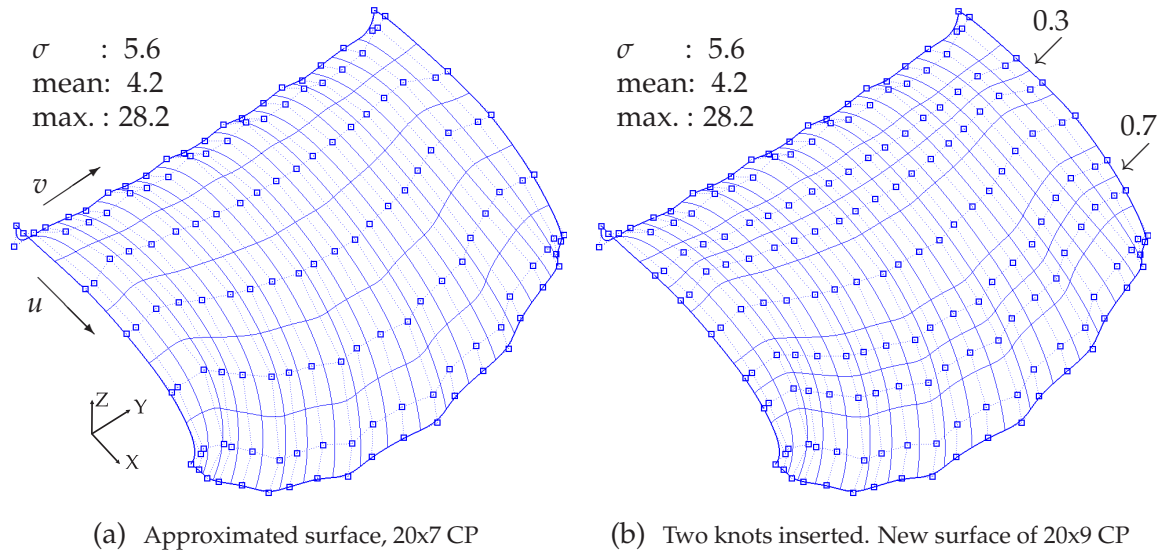


Figure 7.5: Knot insertion. Comparison between errors.

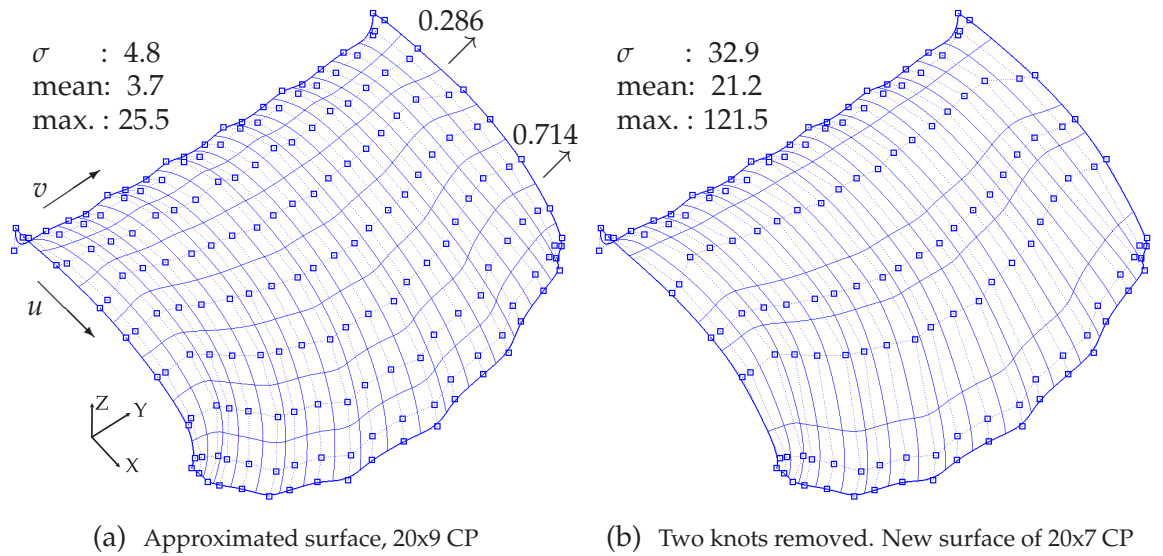


Figure 7.6: Knot removal. Comparison between errors.

thickness, as well as finite element mesh and geometrical restrictions for optimization.

7.3.1 Variable Linking in Shape Optimization

Figure 7.7(a) shows the variable linking, along one row (parametric direction v) of control points for one of the geometrical models. Shape modification is symmetric w.r.t the plane xz . Every control point linked to one optimization variable is indicated with the same symbol.

Since five control points modify the surface between boundaries along parametric direction u , a total of 35 optimization variables are left in the optimization model.

Figure 7.7(b) shows the region of influence of control points 66 and 75 over the finite-element mesh. The finite elements which are modified when these control points are relocated, were removed from the figure. The region of influence is first calculated at parametrical level and later transformed into the geometrical domain using the mapping $S(u, v)$ as explained in section 4.2.

The direction of movement of every control point during optimization, was set to be the normal to surface at the point on the surface, which gives the minimum distance to the corresponding CP.

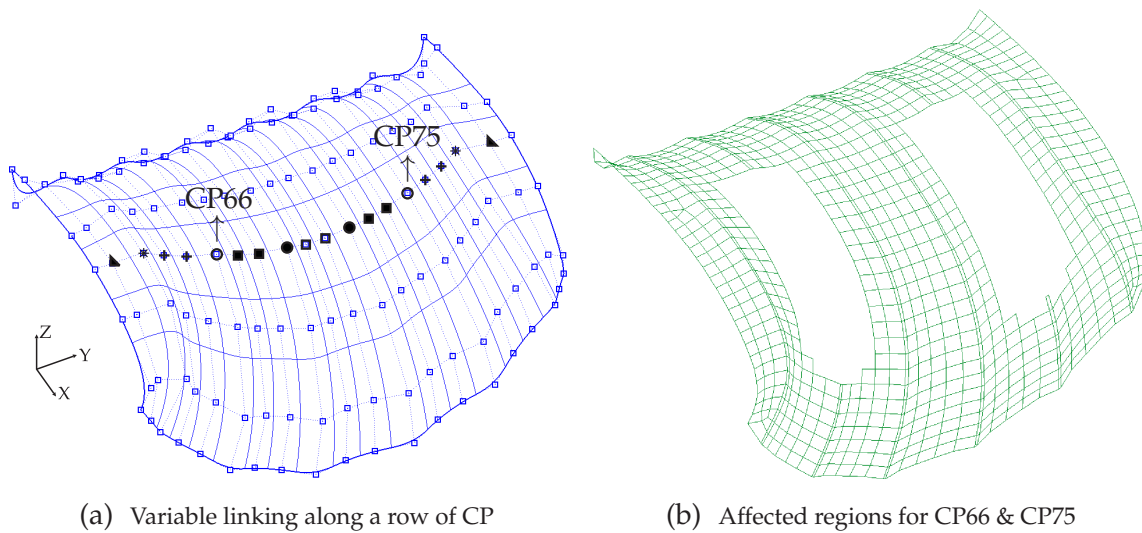


Figure 7.7: Variable linking and through CP affected regions. Surface of 20x7 CP.

7.3.2 Variable Linking in Sizing Optimization

21 design variables were used to modify the thicknesses of the finite elements in the structural model when sizing optimization was included. Figure 7.8 shows the linking between optimization and structural variables, represented by regions on the surface which have the same color, along central, bottom and top rows. The first 12 variables modify the FE-Thickness on surfaces between arches, whereas the remaining 9 variables are assigned to the elements which are located along the arches. Symmetry was also considered about the plane xz .

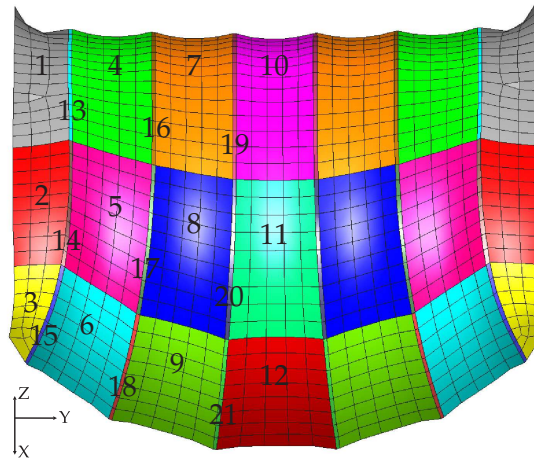


Figure 7.8: Distribution of design variables for sizing optimization.

7.3.3 FE-Discretization and Geometrical Restriction

Figure 7.9 contains the arrangement of the finite element mesh used for optimization. It reduces the number of nodes (together with the number of degrees of freedom) from 3519 to 1170 compared to the mesh used to define the equilibrium shape using form finding. The reason for this d.o.f. reduction, is the saving in computational time, since an optimization calculation is highly demanding.

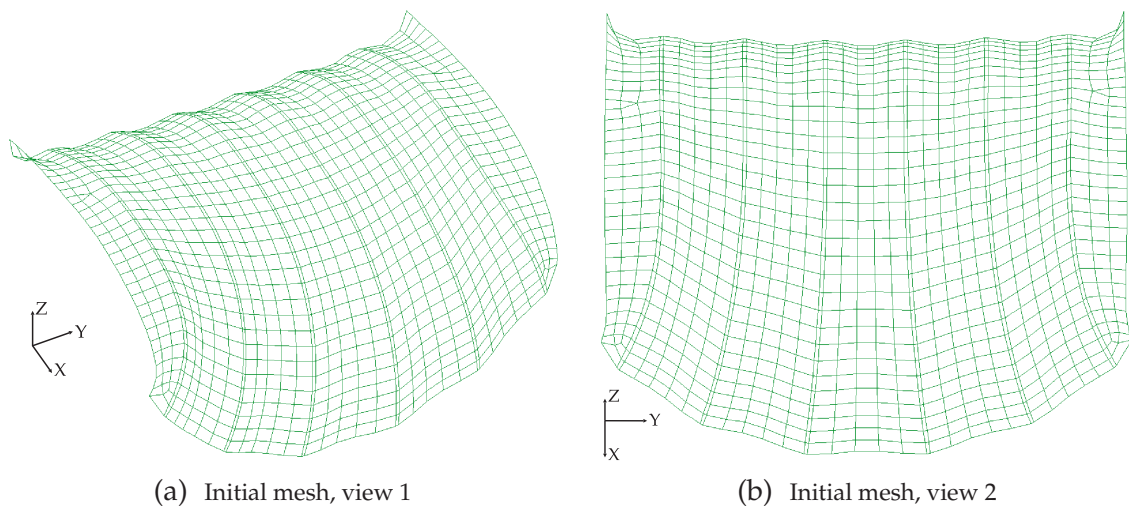


Figure 7.9: Initial finite element mesh for optimization.

Figure 7.10 displays the geometrical conflict the selected surfaces have with the landing gear. This problem has to be eliminated during optimization. Due to the absence of geometrical constraint at the time the examples were analysed, the optimum was found after several optimizations, by relocating control points responsible for penetrations between surfaces, before each optimization began.

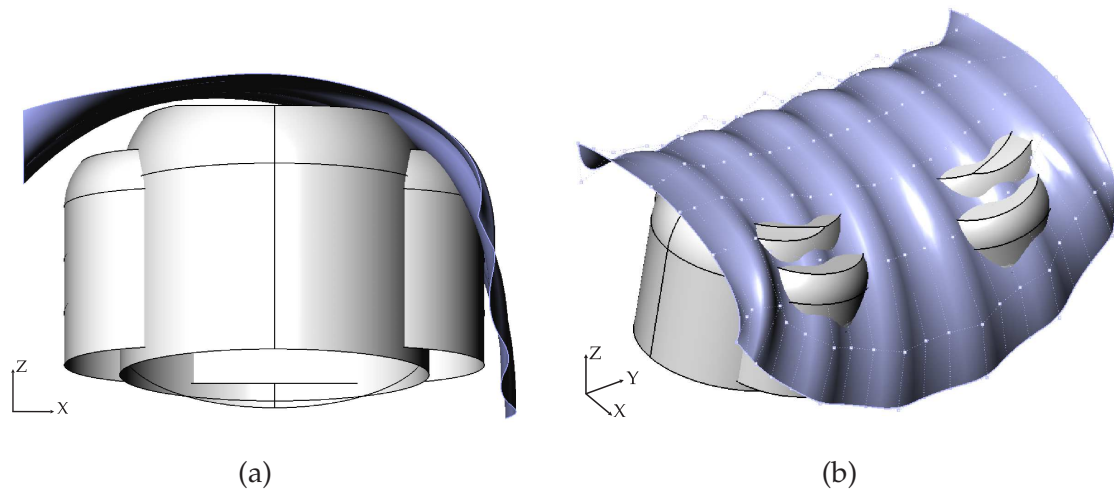
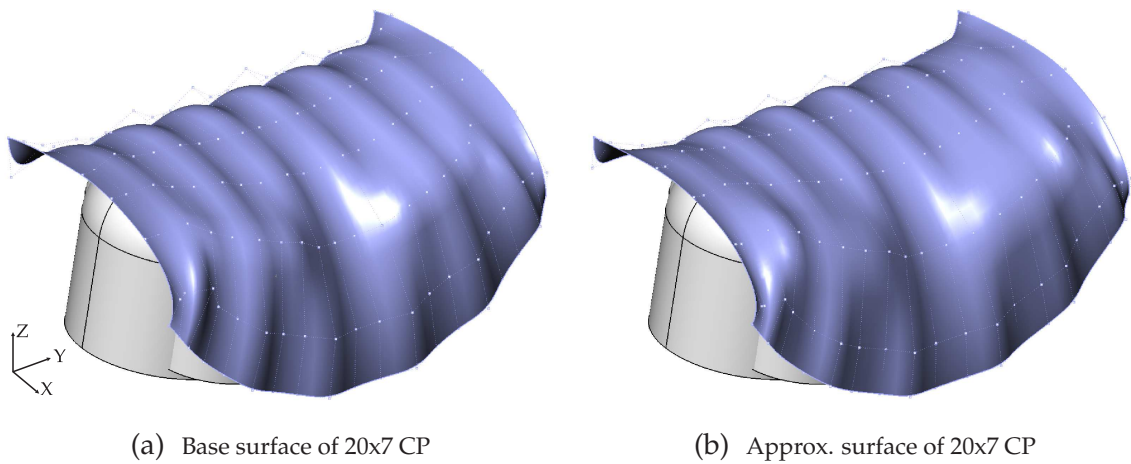


Figure 7.10: Landing-gear conflict.

Figure 7.11 shows base and approximated surfaces selected for optimization, after the first relocation of control points.



(a) Base surface of 20x7 CP

(b) Approx. surface of 20x7 CP

Figure 7.11: First modification of CP.

7.3.4 Results

Shape and sizing optimization techniques are used to find optimal configurations over two geometrical models, base and approximated surfaces indicated in figure 7.4. The results are divided into two main sections depending on the type of optimization used in the solution: shape optimization followed by sizing optimization, and combination of shape and sizing applied simultaneously. In each section, results related to base and approximated surfaces are given using graphs and self-explanatory images. The collection of figures, for each optimization type and geometrical model, begins with the sequence of optimization configurations, which include control point repositioning. Because of the absence of a suitable geometrical constraint, at the time the calculations were performed, and the wish of deviating as less as possible from the initial shape, after each optimization, only the CP responsible for geometry penetration were relocated. The new position was reached by moving the CPs along the related direction of movement; normal to surface. Their lower limits (new location) were set to be fixed before the next optimization was started. The remaining figures contain the geometry of the optimum that belongs to the final optimization sequence, including optimization history (of the final optimization sequence) followed by a load-displacement diagram showing the maximum load factor the structure reaches before instability occurs. Maximum values of the principal stresses σ_1 and σ_2 of the finite element mesh for a load factor λ equal to one, are the last information in the sequence of figures. For sizing optimization, the optimal thickness distribution is also provided.

It is important to mention that during optimization, the direction of the pressure-loading remains unchanged with respect to the initial configuration, due to software restrictions. This is another reason, why a geometrically nonlinear verification is so important in order to check the performance of the final optimum, where the pressure direction is updated at each optimization step.

No explicit imperfections were applied to the geometrical models. Nevertheless, there are geometrical differences between symmetrical regions of the structure due to approximations associated to surface fitting (symmetry was not considered in fitting step). As a consequence, some symmetrical control points w.r.t the xz plane, show maximum differences of approximately seven millimeters in space. Moreover, the finite element mesh generated for optimization, which is later projected onto the corresponding geometrical model is not 100% symmetric. All these modeling "imperfections" are translated into geometrical imperfections, and remain in the model as a sort of approximation for "real" simulated imperfections.

7.3.4.1 Shape Optimizaiton Followed by Sizing Optimization

Base Surface - Shape Optimization

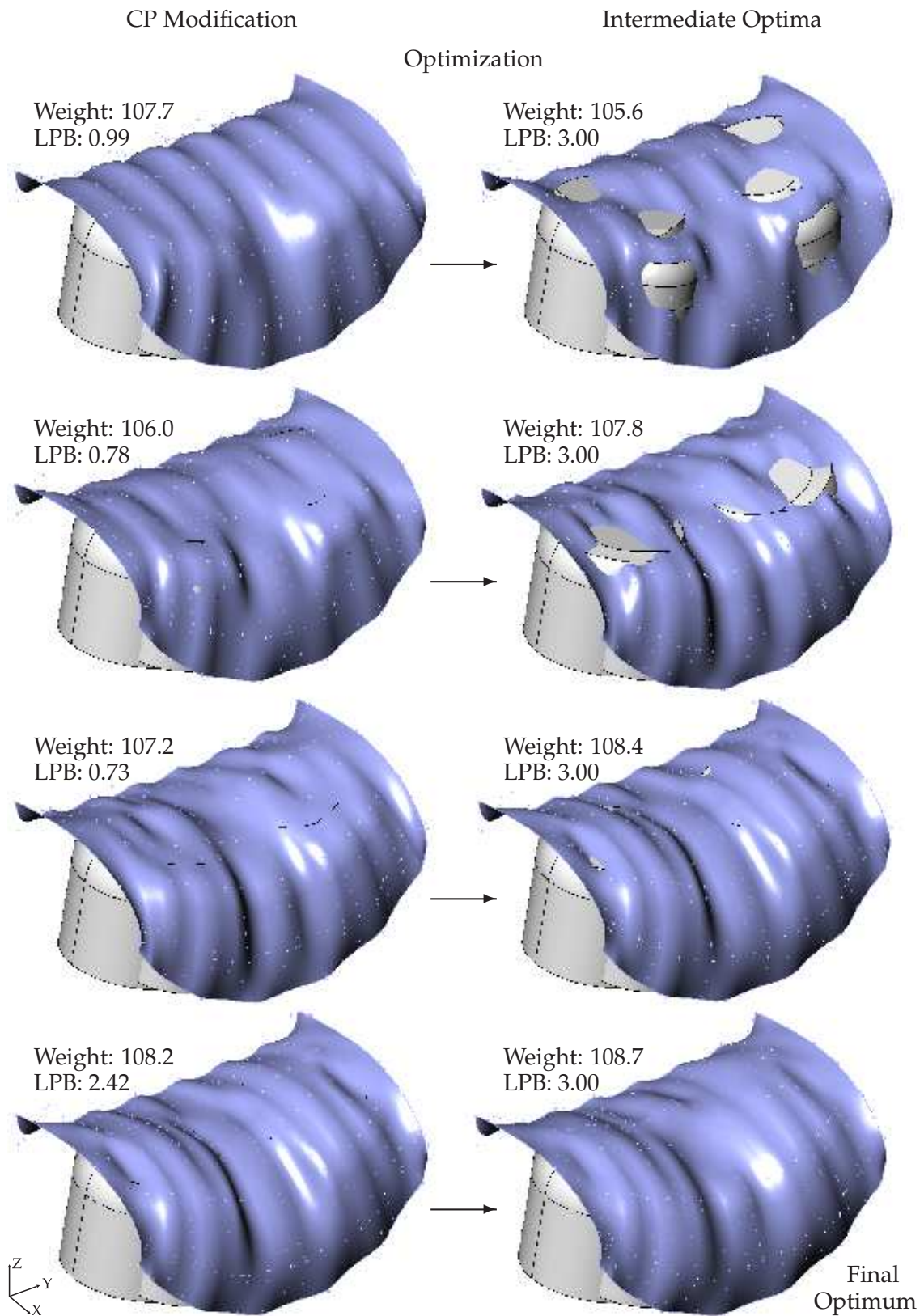


Figure 7.12: Control point modification. Shape optimization - Base surface.

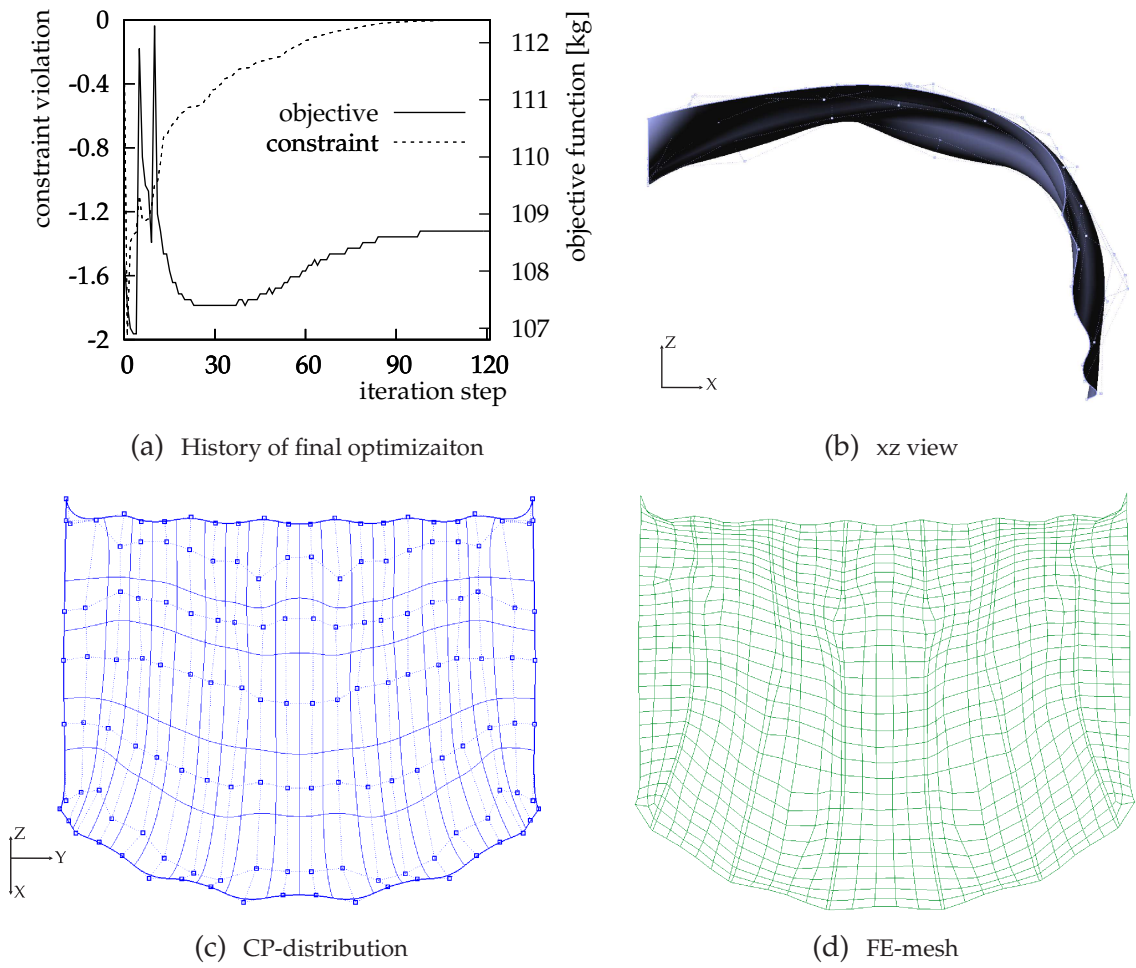


Figure 7.13: Final configuration. Shape optimization - Base surface.

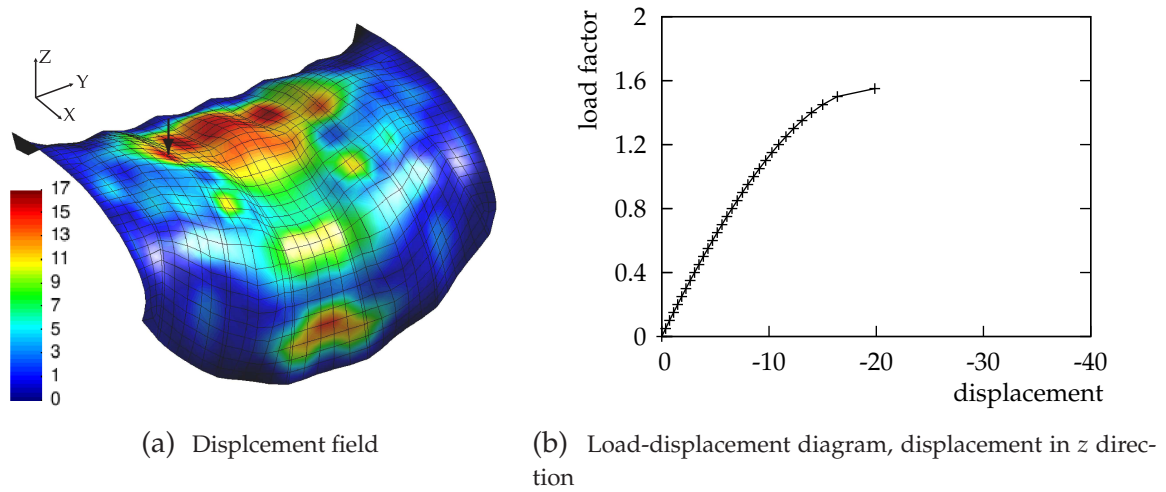
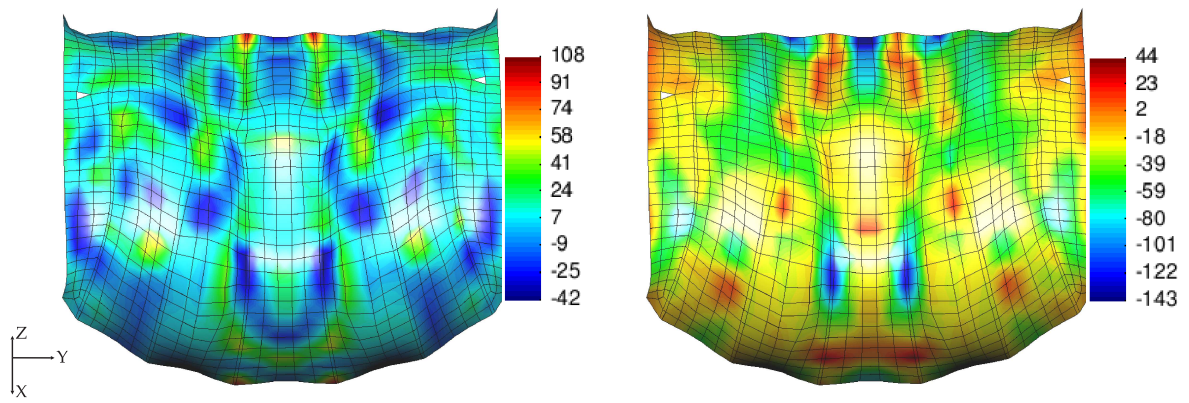


Figure 7.14: Non-linear results. Shape optimization - Base surface.



(c) Principal stress 1, max. value. Load factor 1.0 (d) Principal stress 2, max. value. Load factor 1.0

Figure 7.14: Non-linear results. Shape optimization - Base surface. (cont)

Base Surface - Sizing Optimization

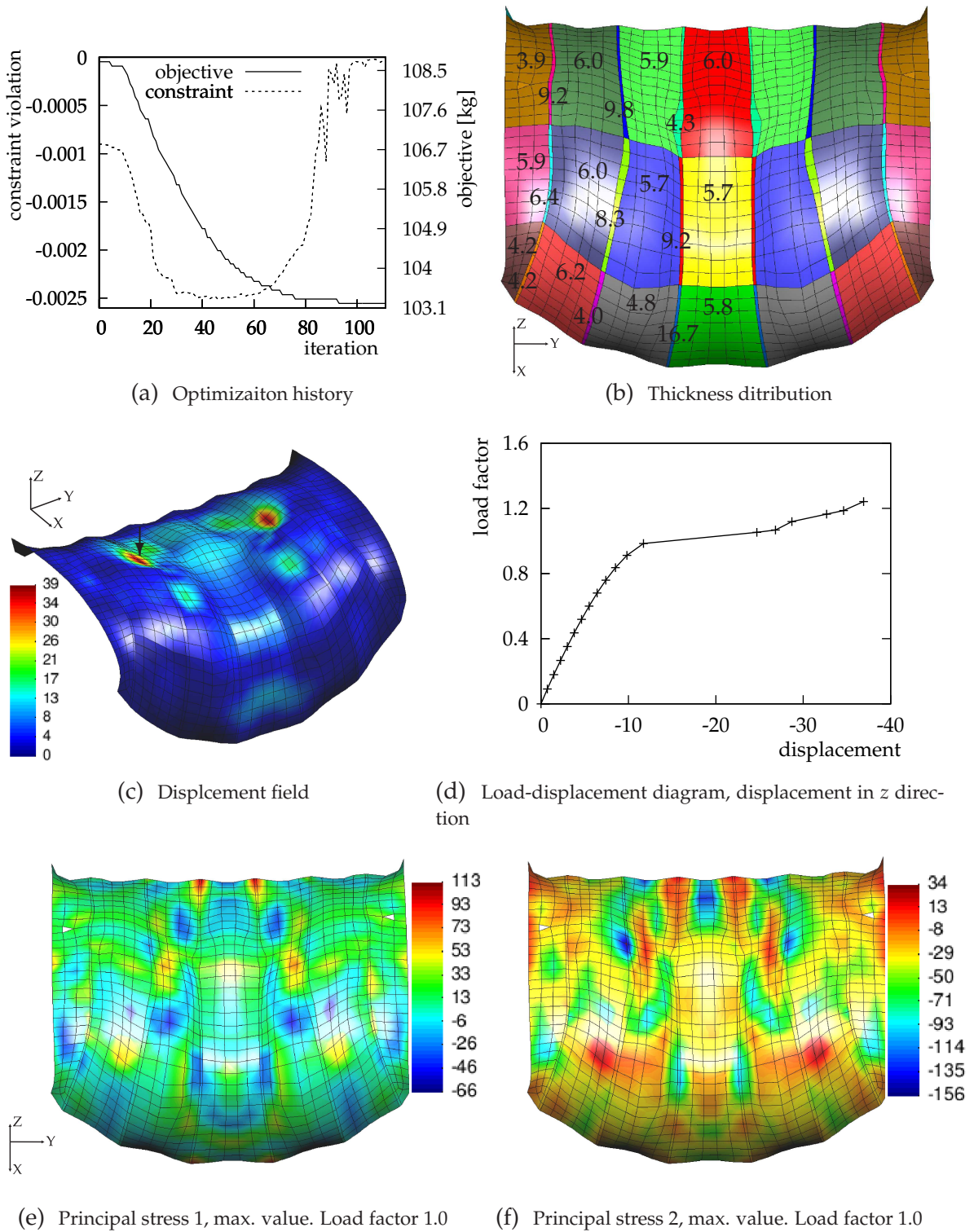


Figure 7.15: Final analysis. sizing (after shape) optimization - Base surface.

Approximated Surface - Shape Optimization

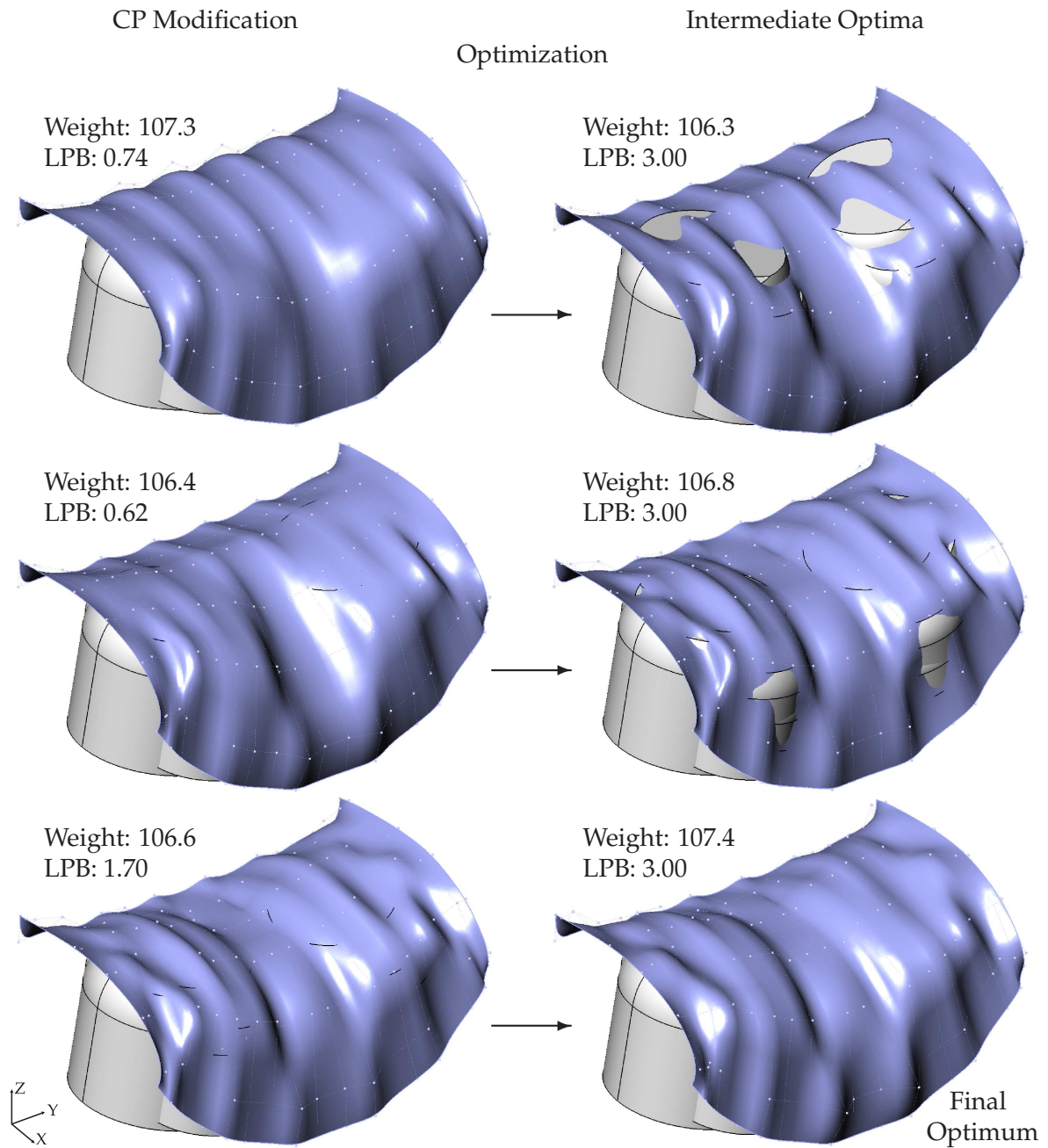


Figure 7.16: Control point modification. Shape optimization - Approximated surface.

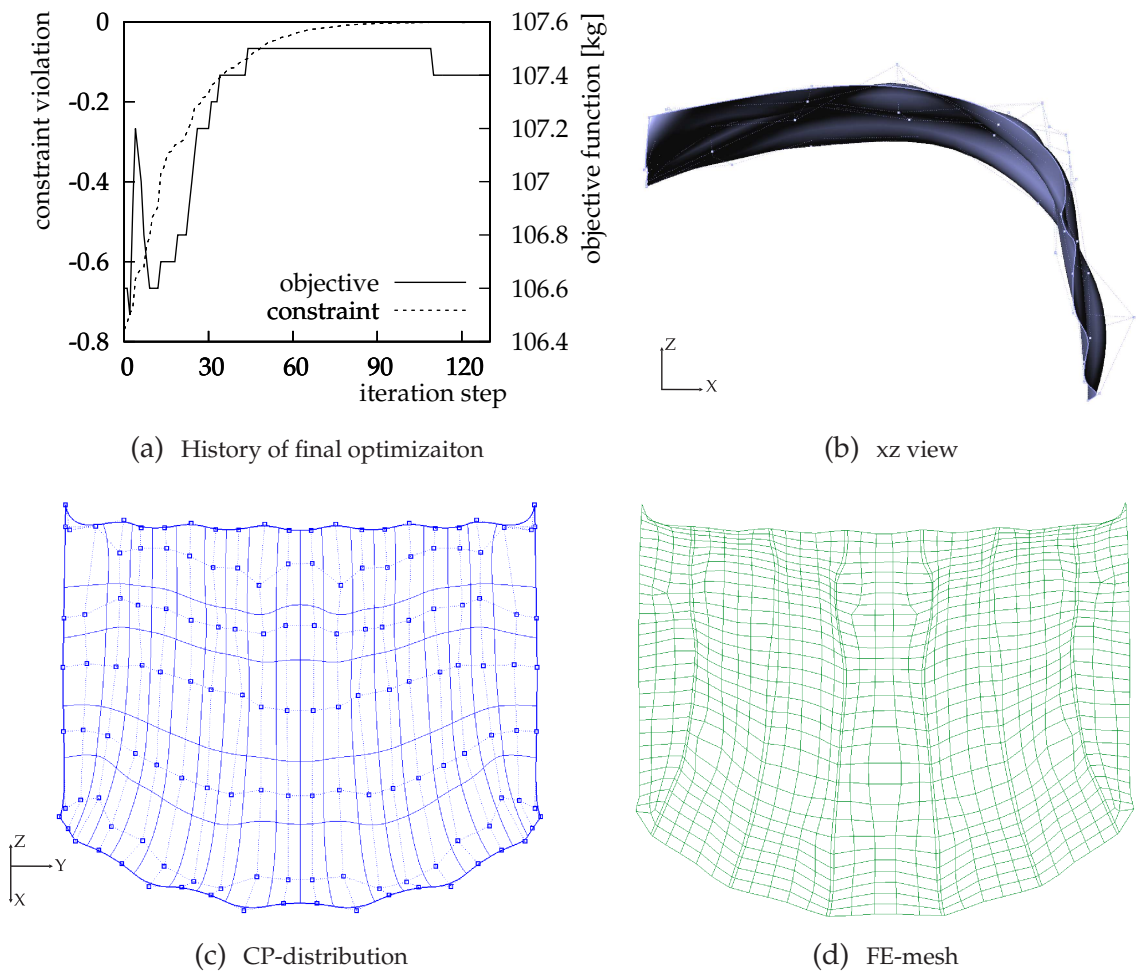


Figure 7.17: Final configuration. Shape optimization - Approximated surface.

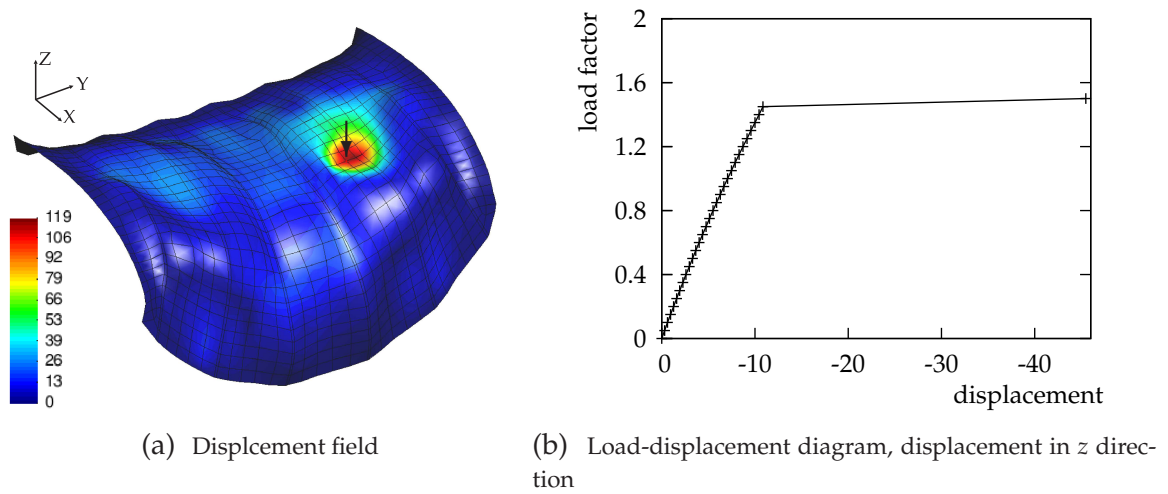
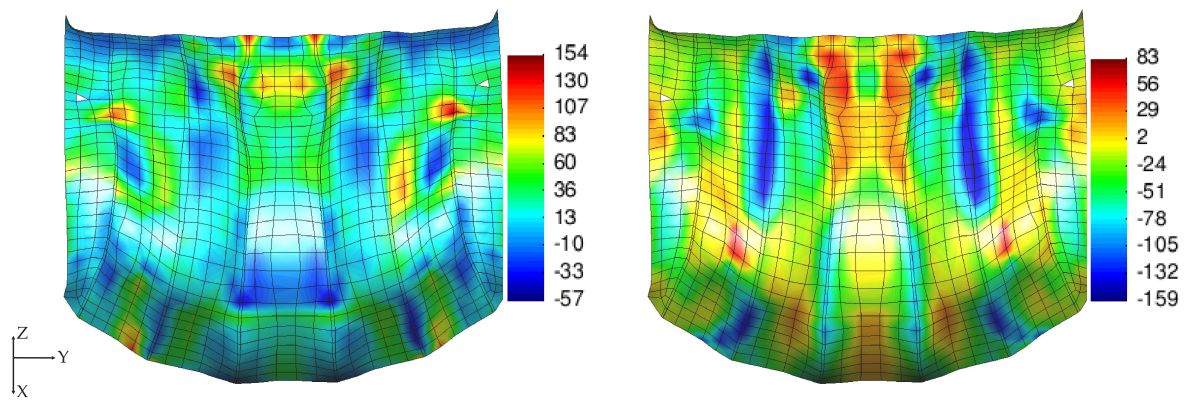


Figure 7.18: Non-linear results. Shape optimization - Approximated surface.



(c) Principal stress 1, max. value. Load factor 1.0 (d) Principal stress 2, max. value. Load factor 1.0

Figure 7.18: Non-linear results. Shape optimization - Approximated surface. (cont)

Approximated Surface - Sizing Optimization

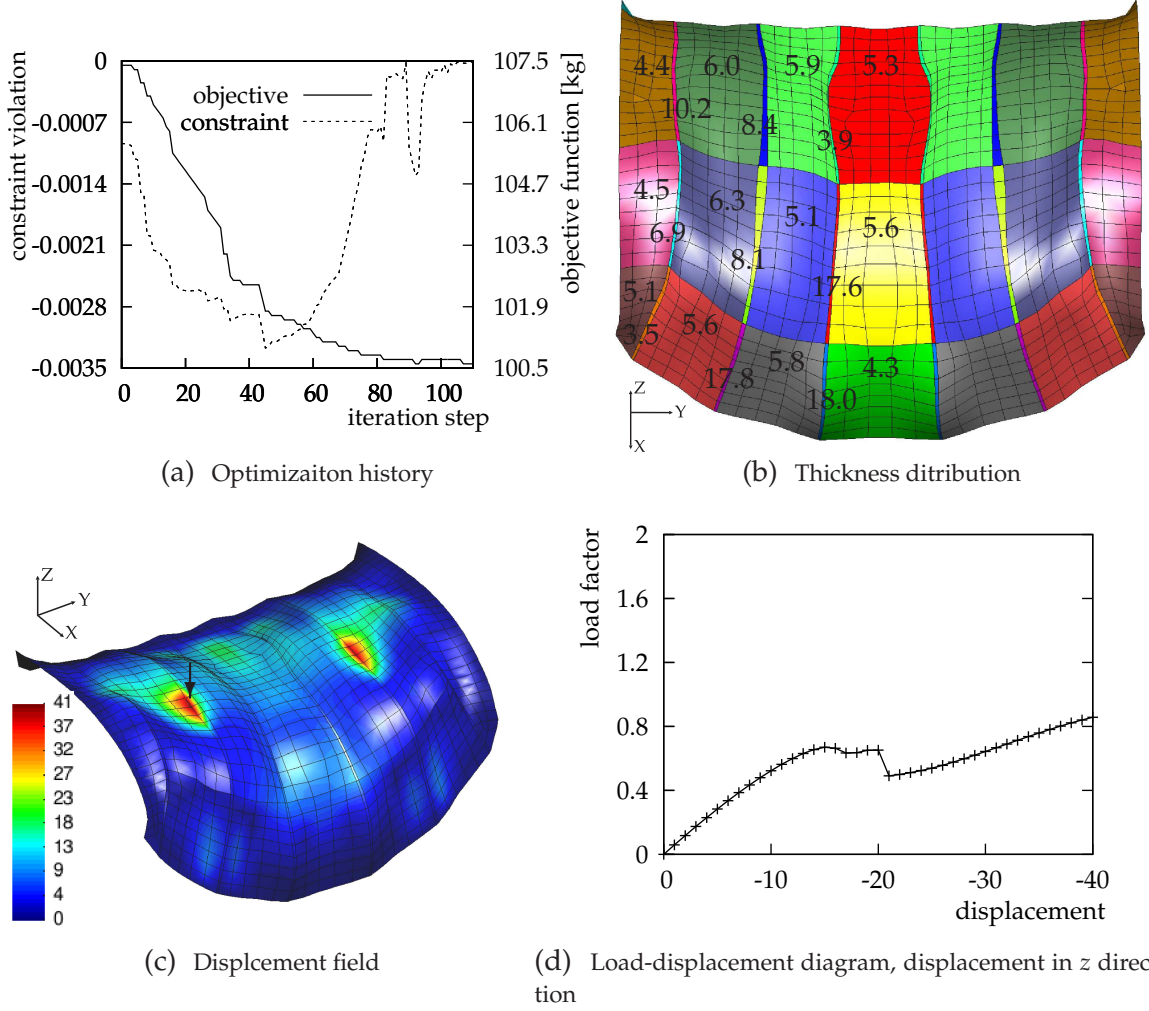


Figure 7.19: Final analysis. sizing (after shape) optimization - Approximated surface.

7.3.4.2 Simultaneous Shape and Sizing Optimization

Base Surface

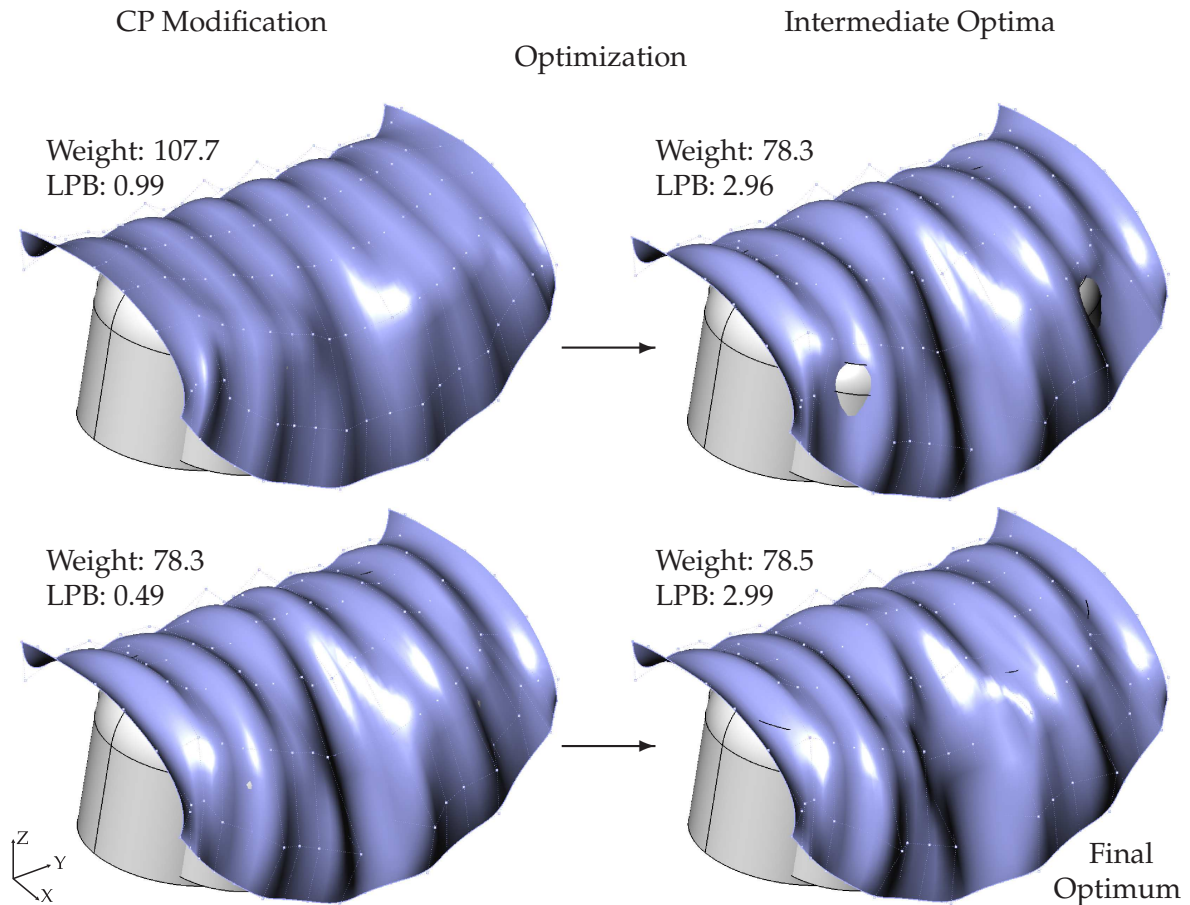


Figure 7.20: Control point modification. Shape & sizing optimization - Base surface.

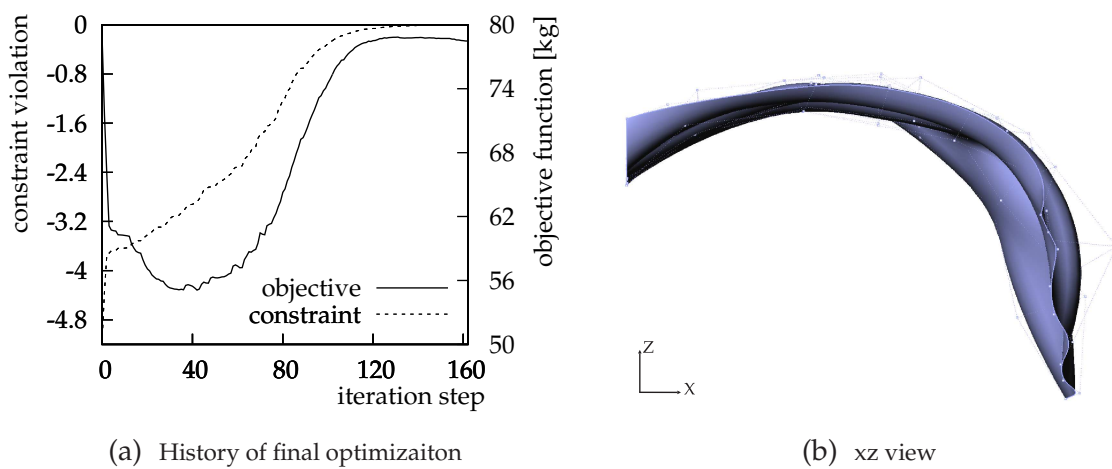


Figure 7.21: Final configuration. Shape & sizing optimization - Base surface.

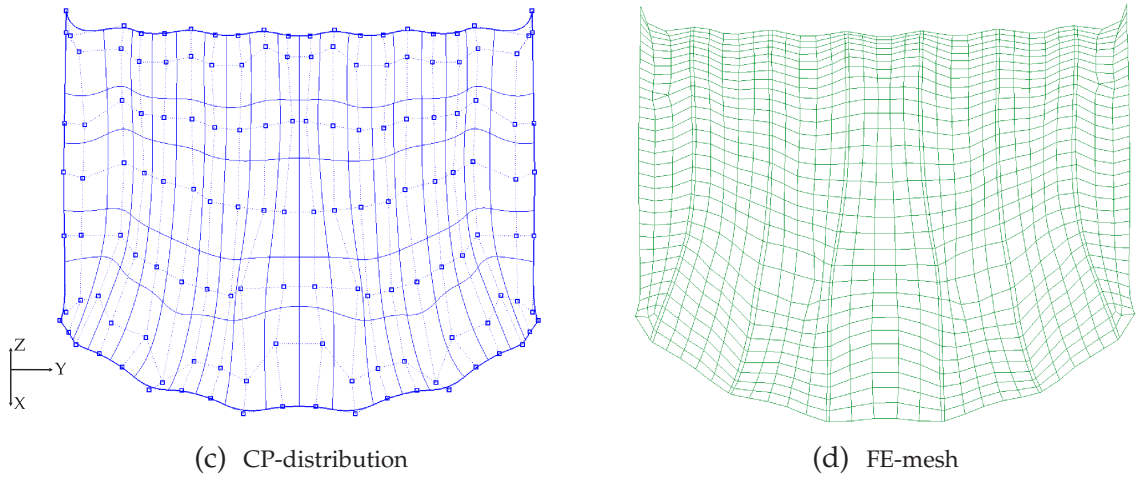


Figure 7.21: Final configuration. Shape & sizing optimization - Base surface. (cont)

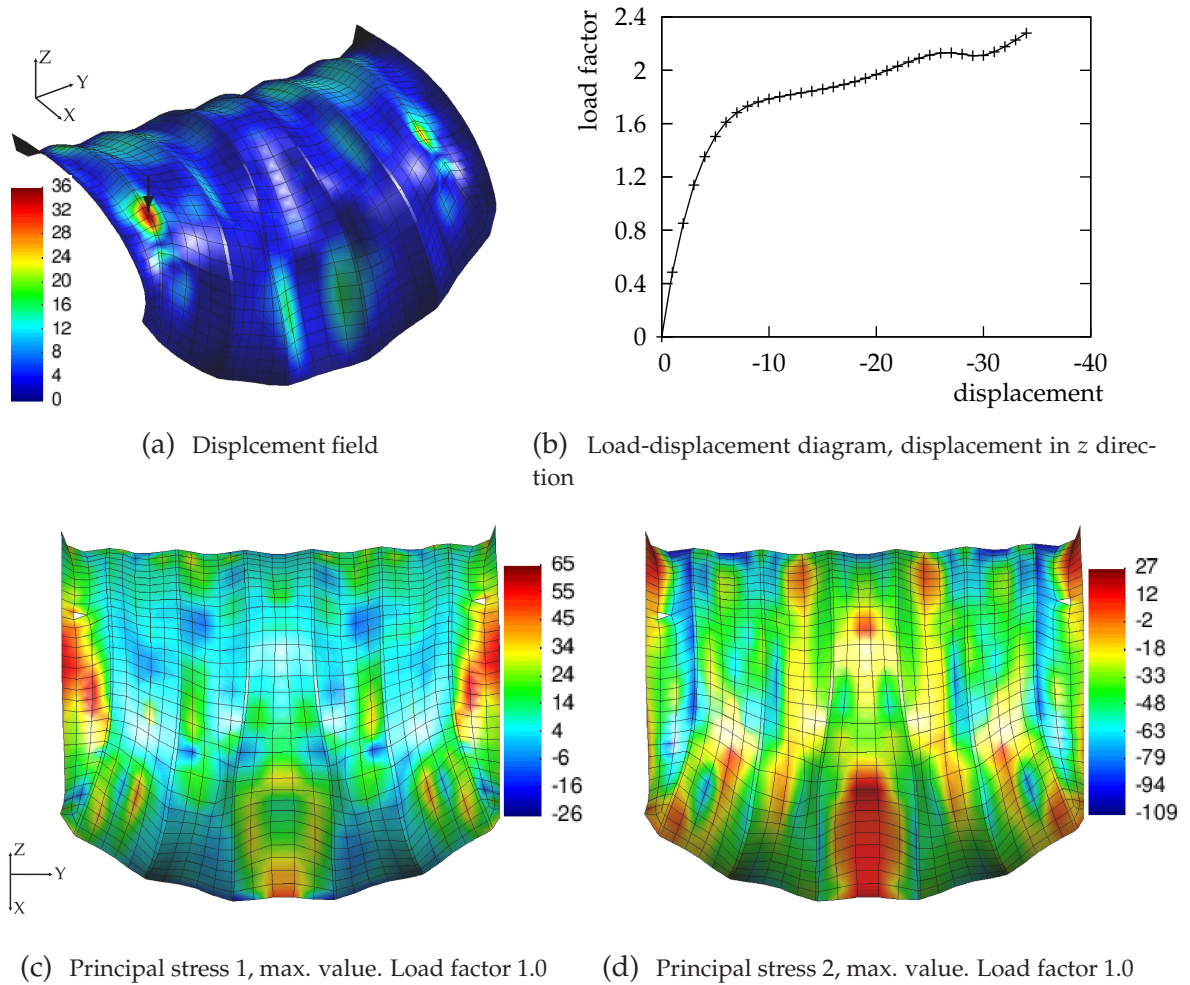


Figure 7.22: Non-linear results. Shape & sizing optimization - Base surface.

Approximated Surface

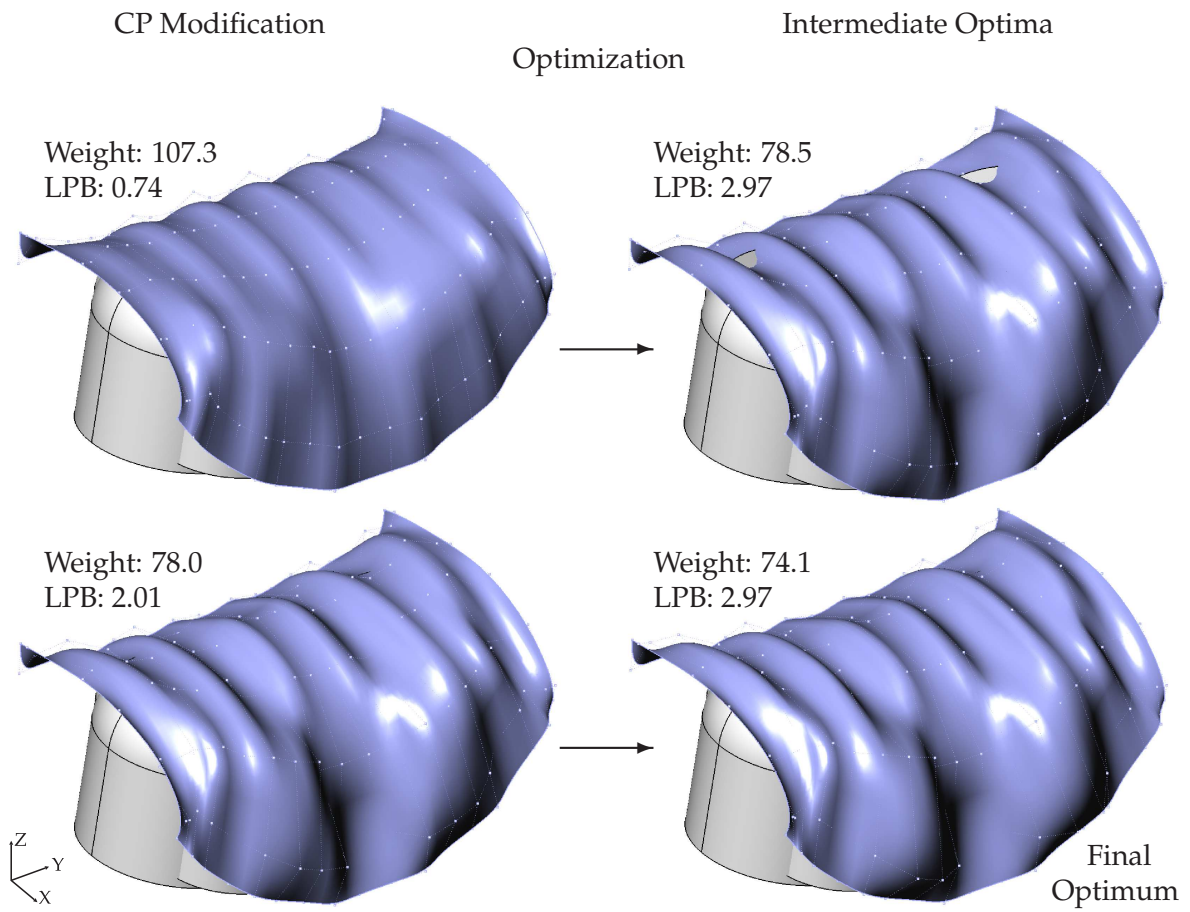


Figure 7.23: Control point modification. Shape & sizing opt. - Approximated surface.

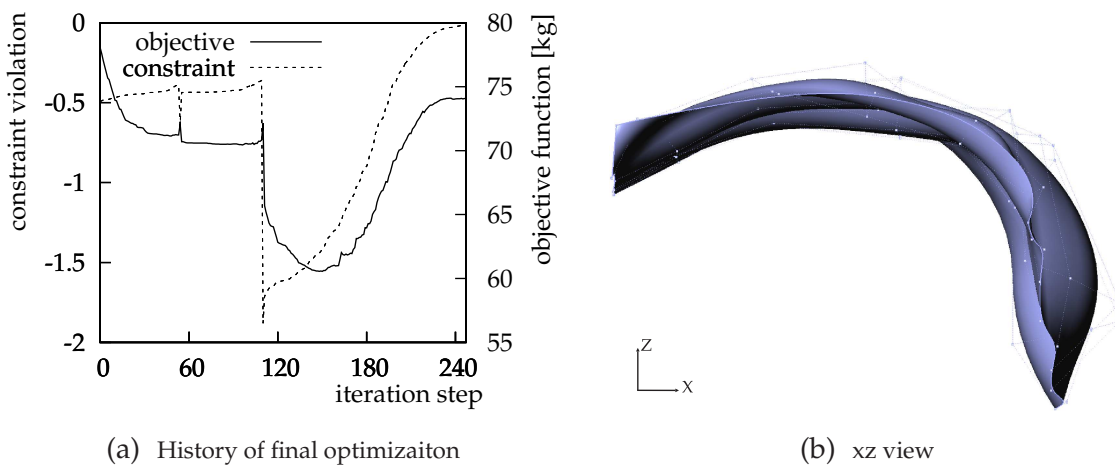


Figure 7.24: Final configuration. Shape & sizing optimization - Approximated surface.

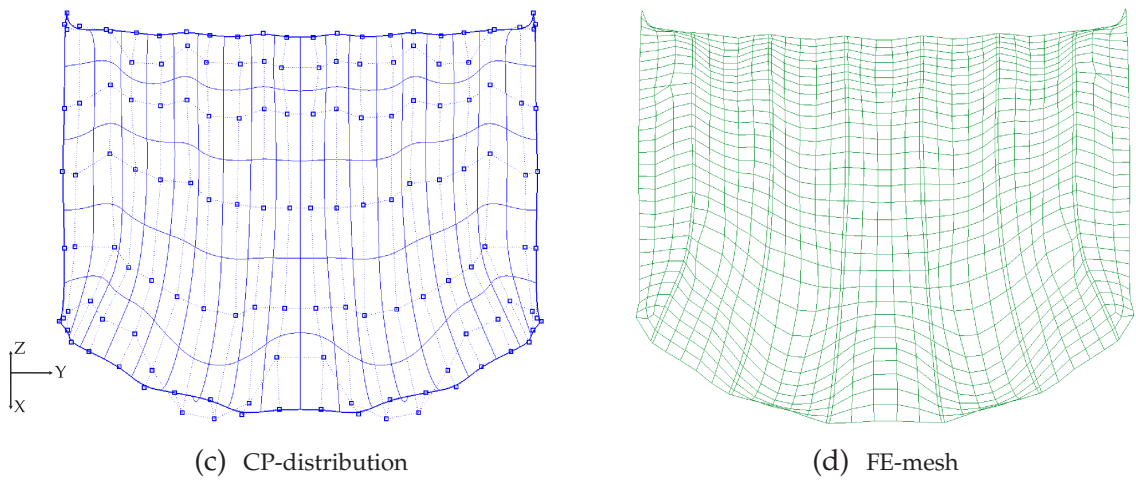


Figure 7.24: Final configuration. Shape & sizing optimization - Approximated surface. (cont)

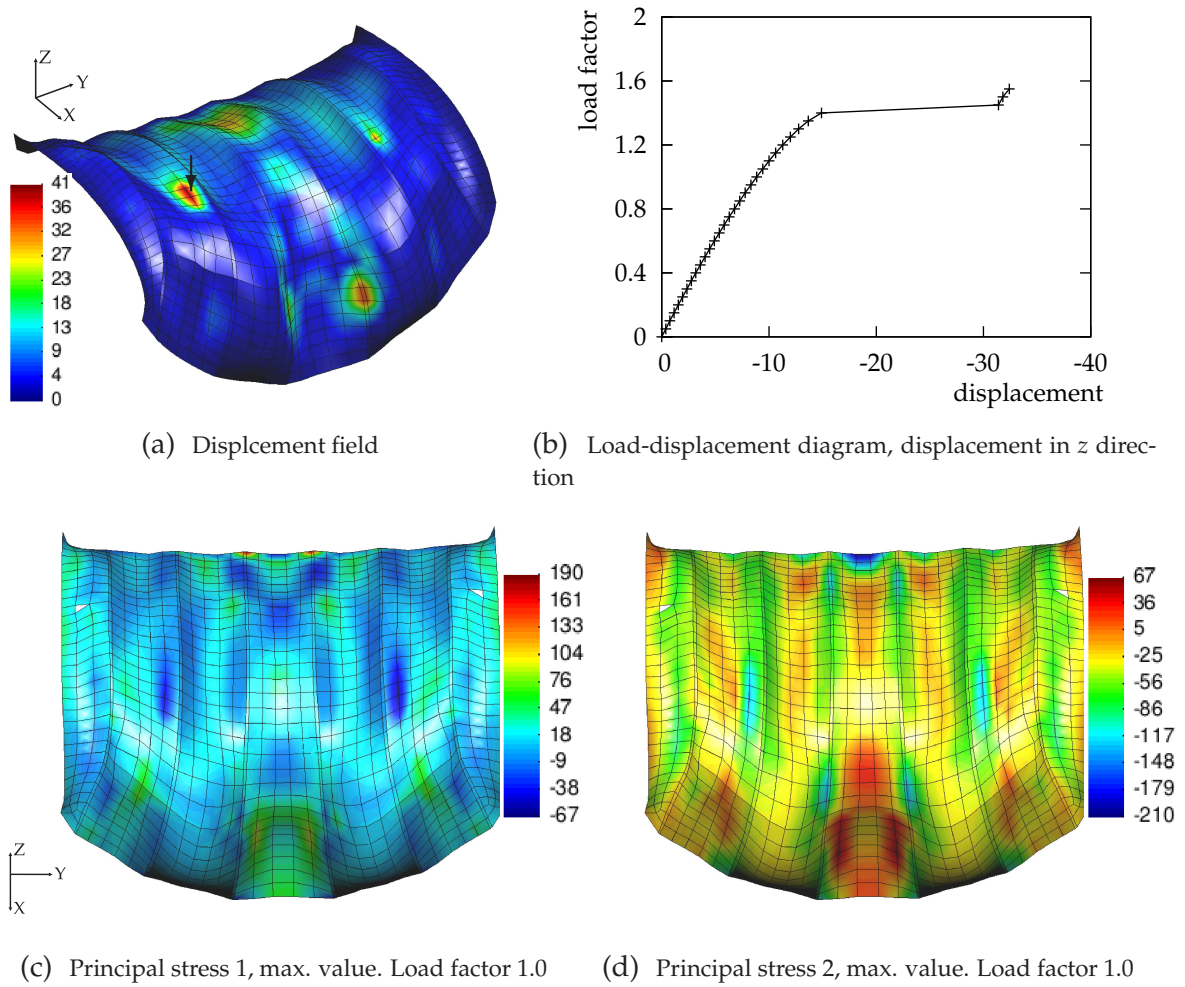
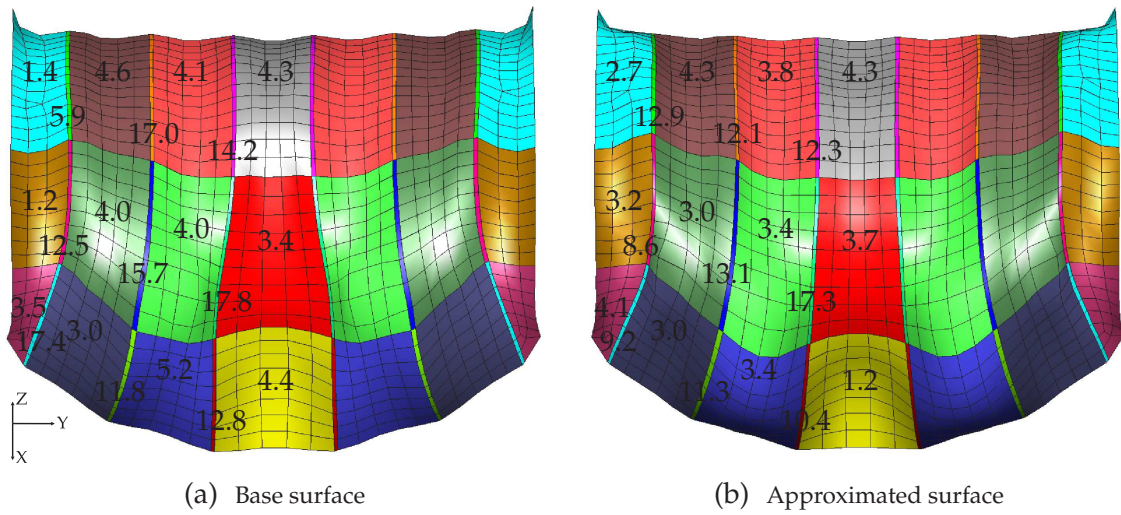


Figure 7.25: Non-linear results. Shape & sizing optimization - Approximated surface.

Final Thickness Distribution**Figure 7.26:** Thickness distribution for final optima.

7.3.5 Final Remarks

The presented design process for pressurized bulkheads has been successfully applied to the previously illustrated examples. Some observations that arose during the process are commented in the following paragraphs.

Specially after shape optimization but also after combined shape and sizing optimization the optimal shape differs from the starting design in terms of topology. Some of the initial six arches tend to disappear or blend together generating bigger and sometimes smoother arches. Different geometric and optimization models allowing a higher freedom in shape generation would probably end up differing even strongly from the initial topology. This could be a disadvantage in case the designer is concerned about guiding the final optimum towards a pre-conceived topology, situation that can be controlled by manipulating the optimization model. For instance, modifying variable linking or including additional geometric constraints. Nevertheless, we have to keep in mind, that the relocation of control points before each optimization sequence, influences also the final optimal shape.

Even though base and approximated surfaces contain the same number of control points, the differences in the geometrical configuration as a result of using different approaches are reflected on the different geometrical tendencies during optimization of both, shape and shape combined with sizing, optimizations. Another important source of variation in the different final optima, is the steering of the optimization algorithm, which may follow different local minima each time.

Because of the differences in the estimated critical load between linearized prebuckling and path-following algorithms (see also section 5.3.1.2), it is fundamental to perform a non-linear verification not only of the critical load but also of the stress state as well as other structural responses which could be of interest for a particular example and which are affected by large displacements. The absence of follower loads within the optimization implementation is another approximation factor in the linearized prebuckling method during optimization.

Although most of the final optima are within acceptable limits regarding non-linear verification, a subsequent validation of the results concerning manufacturing of the material has to be done (not included in the present work). This situation can also be controlled during optimization by adding manufacturing restrictions in the geometry, for instance curvature restrictions. Nevertheless the selection of the optimization model (number of variables and variable linking) strongly influences the final smoothness of the geometry.

Concerning numerical results, and further observations, the following can be said:

- ◇ From the load-displacement diagrams only the case of sizing optimization performed after shape optimization of the geometrical model corresponding to the base surface shows a final design whose critical load factor is less than 1.0.

- ◇ Maximum stress values in the stress-distribution figures (geometrical nonlinear simulation) are still within the linear material range imposed for the analysis.
- ◇ Mesh refinement on the final optima could improve the accuracy of the results.
- ◇ A more accurate analysis regarding imperfections including more realistic manufacturing defects in the modeling would provide more practical results.
- ◇ The geometry along the boundary of the structure was not considered as variable during optimization. Other kind of examples would probably include it, in order to have an even higher flexibility to define the optimal shape.
- ◇ The inclusion of weights-parameters at each control point of the geometrical model (NURBS) would provide a higher degree of flexibility, for instance in a post-optimization stage. Nevertheless, higher mesh distortions are to be expected, and should be controlled.
- ◇ Geometrical restrictions use the undeformed configurations as reference without taking into account deformations due to the applied load.
- ◇ No filtering algorithm, or stabilization technique, regarding smoothness of the thickness distribution was including in sizing optimization. One of the possible solutions would be to assign an additional B-spline over the midsurface of the shell only for thickness control.

Chapter 8

Conclusions and Outlook

The presented methodology for the design of pressurized thin-walled shells could be used and demonstrated for one of the geometrical configurations studied through this work. This shows the potentials of the method and also the possibility of using it for similar structural components considering perhaps different types of loading.

Once again the use of structural optimization strategies might lead to final configurations that the designer cannot always predict, fulfilling at the same time the particularly imposed restrictions. For the same reason, in some cases the geometrical arrangement of the final optimum might not be a suitable one in terms of, for instance, architectural reasons. Nevertheless the design can always be guided to a more adequate solution by including additional constraints in the formulation.

Geometrical solutions using form finding produce harmonic shapes and suitable structural configurations to carry external loads mainly by means of membrane strains. However, the design of thin-walled shells also includes bending stresses, and deviations of form finding designs are needed in order to adjust the shape to the current restrictions regarding load and boundary conditions.

Additional constraints could be considered in fitting algorithms in order to increase accuracy in surface approximation. On the other hand, a high degree of accuracy in surface fitting used to generate geometrical models for shape optimization becomes less significant when the number of geometrical coefficients is restricted to a certain limit because of requirements in shape control, for example: restricting the space of possible shapes, minimizing the risk of having sharp changes in curvature or preventing unnecessary increments in computational costs.

When optimizing slender structures, like the ones investigated in this work, the importance of a geometrically non-linear verification should not be underestimated. Differences between critical loads obtained by means of linearized prebuckling and geometrically non-linear analysis over the same structural configuration are in some cases significant. This fact might not be only be important in terms of stability, but also in other structural responses which are also displacement dependent. In the same context, geometrically non-linear formulations are fundamental in performing imperfection studies in case imperfection-sensitive structures are analysed.

When optimizing slender structures, like the ones investigated in this work, the importance of a geometrically non-linear verification should not be underestimated. Differences between critical loads obtained by means of linearized prebuckling and geometrically non-linear analysis over the same structural configuration are in some cases significant. This fact might not be only important in terms of stability, but also in other structural responses which are also displacement dependent. In the same context, geometrically non-linear formulations are fundamental in performing imperfection studies in case imperfection-sensitive structures are analysed.

If the material behavior goes beyond elastic limits, as it may eventually happen when post-buckling regions are of interest for the analysis, the inclusion of nonlinear material formulations in the constitutive equations would be advisable.

An important improvement for the presented design process would be the inclusion of geometrically nonlinear formulations, not only as a method for verification, but rather directly in the structural analysis used to calculate responses of interest for optimization. In this case, important increments in computational time should be expected.

Bibliography

- [BFD08] K.-U. Bletzinger, M. Firl, and F. Daoud. Approximation of derivatives in semi-analytical structural optimization. *Computers & Structures*, 86:1404–1416, 2008.
- [BFLW08] K.-U. Bletzinger, M. Firl, J. Linhard, and R. Wüchner. Optimal shapes of mechanically motivated surfaces. *Computer Methods in Applied Mechanics and Engineering*, Online Publication, 2008.
- [BKS94] K.-U. Bletzinger, S. Kimmich, and Hans Stegmüller. User manual of carat. institut für baustatik, prof. dr.-ing. e. ramm, universität stuttgart, 1994.
- [Ble90] K.-U. Bletzinger. *Formoptimierung von Flächentragwerken*. PhD thesis, Universität Stuttgart, 1990.
- [Ble98] K.-U. Bletzinger. Form Finding and Optimization of Membranes and Minimal Surfaces. Lehrstuhl für Statik, Technische Universität München, June 1998. Lecture notes, prepared for the Ph.D.-course/Advanced school on Advanced Topics in Structural Optimization.
- [Ble04] K.-U. Bletzinger. Lecture notes of structural optimization, chair of structural analysis, 2004.
- [BLM00] T. Belytschko, W.K. Liu, and B. Moran. *Nonlinear Finite Elements for Continua and Structures*. John Wiley & Sons Ltd, Chichester, England, 2000.
- [BR99] K.-U. Bletzinger and E. Ramm. A general finite element approach to the form finding of tensile structures by the updated reference strategy. *International Journal of Space Structures*, 14 No. 2:131–145(15), 1999.
- [BRKR93] K.-U. Bletzinger, R. Reitinger, S. Kimmich, and Ekkehard Ramm. Shape optimization with program carat. *International Series of Numerical Mathematics*, 110, 1993.
- [BS96] C. Blanc and C. Schlick. Accurate parametrization of conics by nurbs. *IEEE Computer Graphics and Applications*, 16(6):64–71, 1996.
- [Bus89] D. Bushnell. *Computerized buckling analysis of shells*. Kluwer Academic Publishers, 1989.
- [BW04] K.-U. Bletzinger and R. Wüchner. Form- Trägt - Formfindung vorgespannter Membrantragwerke. in: 8. Dresdner Baustatik Seminar - Kreative Ideen im Ingenieurbau. Dresden, 2004.

- [BWDC05] K.-U. Bletzinger, R. Wüchner, F. Daoud, and N. Camprubí. Computational methods for form finding and optimization of shells and membranes. *Comput. Methods Appl. Mech. Engrg.*, 194:3438–3452, 2005.
- [Cam04] N. Camprubí. *Design and Analysis in Shape Optimization of Shells*. PhD thesis, Technische Universität München, 2004.
- [CB03] D. Chapelle and K.J. Bathe. *The Finite Element Analysis of Shells - Fundamentals*. Springer-Verlag, Cambridge, MA, USA, 2003.
- [CH09] S. Cho and S.-H. Ha. Isogeometric shape design optimization: exact geometry and enhanced sensitivity. *Structural and Multidisciplinary Optimization*, 38:53–70, 2009.
- [CRE01] E. Cohen, R. F. Riesenfeld, and G. Elber. *Geometric Modeling with Splines*. A K Peters, 2001.
- [Cri81] M. A. Crisfield. A fast incremental/iterative solution procedure that handles snap-through. *Computer & Structures*, 13:55–62, 1981.
- [Dao05] F. Daoud. *Formoptimierung von Freiformschalen*. PhD thesis, Technische Universität München, 2005.
- [dB78] C. de Boor. *A Practical Guide to Splines*. Springer-Verlag, New York, 1978.
- [DCB05] F. Daoud, N. Camprubí, and K.-U. Bletzinger. Filtering and regularization shape optimization techniques for optimization with cad-free parametrization. In *Book of Abstracts of Third M.I.T Conference on Computational Fluid and Solid Mechanics*, (K.-J. Bathe, ed.), M.I.T Cambridge, MA USA, 2005.
- [DS96] J. E. Dennis and R. B. Schnabel. *Numerical Methods for Unconstrained Optimization and Nonlinear Equations*. SIAM, 1996.
- [EAD] EADS. Illustrations from different internal reports regarding studies of pressurized shell-structures.
- [Esp08] Pablo Andres Suarez Espinoza. Shape design by means of form finding and stability analysis of a bulkhead, structural component in aircraft systems. Technical report, Lehrstuhl für Statik, Technische Universität München, 2008.
- [Far92] G. Farin. From conics to nurbs: A tutorial and survey. *IEEE Computer Graphics and Applications*, 12(5):78–86, 1992.
- [Far99] G. E. Farin. *NURBS*. Peters, 1999.
- [Far02] G.E. Farin. *Curves and Surfaces for CAGD: a Practical Guide*. Morgan Kaufmann, fifth edition, 2002.
- [Fel01] C. A. Felippa. *Nonlinear Finite Element Methods*. Department of Aerospace Engineering Sciences and Center for Space Structures and Controls, University of Colorado, Boulder, USA, August 2001. Material assembled from lecture notes.

- [FM04] B. Forster and M. Mollaert. *European Design Guide for Tensile Surfaces Structures*. TensiNet, 2004.
- [FWB07] M. Firl, R. Wüchner, and K.-U. Bletzinger. In plane regularization of parameter free shape optimization problems. In *7th World Congress on Structural and Multidisciplinary Optimization*, 2007.
- [FWB09] M. Firl, R. Wüchner, and K.-U. Bletzinger. Regularization of shape optimization problems. *Submitted to Structural and Multidisciplinary Optimization*, 2009.
- [GHH99] Z. Gürdal, R.T. Haftka, and P. Hajela. *Design and Optimization of Laminated Composite Materials*. John Wiley & Sons Ltd, Danvers, MA, USA, 1999.
- [HCB05] T.J.R Hughes, J.A. Cottrell, and Y. Bazilevs. Isogeometric analysis: Cad, finite elements, nurbs, exact geometry and mesh refinement. *Comput. Methods Appl. Mech. Engrg.*, 194:4135–4195, 2005.
- [Her05] M. Herrenbrück. Formfindung und stabilitätsuntersuchungen eines druckschotts im flugzeubau. Master’s thesis, Lehrstuhl für Statik, TU München, 2005.
- [HG92] R.T. Haftka and Z. Gürdal. *Elements of Structural Optimization*. Kluwer Academic Publishers, Dordrecht, The Netherlands., 1992.
- [HG00] K. Hormann and G. Greiner. *Modeling and Visualization*, chapter Quadrilateral remeshing, pages 153–162. 2000.
- [Hol00] G.A. Holzapfel. *Nonlinear Solid Mechanics*. John Wiley & Sons Ltd, Chichester, 2000.
- [Hör94] K. Hörsting. *Rationalisierung der Fertigung langfaserverstärkter Verbundwerkstoffe durch den Einsatz multiaxialer Gelege*. PhD thesis, Technische Hochschule Aachen, 1994.
- [Hor00] K. Hormann. *Fitting free form surfaces. Principles of 3D Image Analysis and Synthesis, volume 556 of The International Series in Engineering and Computer Science*. Kluwer Academic Publishers, Boston, MA, 2000.
- [Hör01] H.R.E.M. Hörnlein. Effiziente semi-analytische gradientenberechnung in der strukturoptimierung. Technical report, DASA Ottobrunn, MT24, 2001.
- [Hor03] K. Hormann. From scattered samples to smooth surfaces. In *In Proceedings of Geometric Modeling and Computer Graphics*, 2003.
- [Hör04a] H.R.E.M Hörnlein. Composite bauweisen für rumpfschottanwendungen (cobra): Topologieschott. Technical Report EADS-S-STY-0296-A, EADS Militärflugzeuge, Juli 2004.
- [Hör04b] H.R.E.M Hörnlein. *LAGRANGE User Manual Volume I*. EADS, Military Aircraft, Dept: MT24, D-81663, München, 06 2004.

- [Hör05] H.R.E.M Hörnlein. Composite bauweisen für rumpfschottanwendungen (cobra): Formfindung der membranefläche. Technical Report EADS-S-STY-0301-A, EADS Militärflugzeuge, Juli 2005.
- [Hör08] H.R.E.M Hörnlein. Cobra, muschelschott mit druckboden, stabilität: Linear vs. non-linear. opes 44. Technical report, EADS Militärflugzeuge, 2008.
- [Hug00] T.J.R. Hughes. *The Finite Element Method: Linear Static and Dynamic Finite Element Analysis*. Dover Publication, Inc., 2000.
- [IHA85] J. Iott, R..T. Haftka, and H.M. Adelman. Selecting step sizes in sensitivity analysis by finite differences. Technical report, NASA TM-86382, 1985.
- [Jar09] A. Jarasjarunkiat. *Nonlinear Analysis of Pneumatic Membranes From Subgrid to Interface*. PhD thesis, Technische Universität München, 2009.
- [KBW09] J. Kiendl, K.-U. Bletzinger, and R. Wüchner. Isogeometric shell analysis with kirchhof-love elements. *Submitted to Computer Methods in Applied Mechanics and Engineering*, May 5, 2009.
- [Kel03] C. T. Kelley. *Solving Nonlinear Equations with Newton's Method*. SIAM, 2003.
- [Koc04] K.-M. Koch. *Bauen mit Membranen*. München, 2004.
- [Kör02] T. Körwien. *Konfektionstechnisches Verfahren zur Herstellung von endkonturnahen textilen Vorformlingen zur Vesteifung von Schalensegmenten*. PhD thesis, Universität Bremen, FB Produktionstechnik, 2002.
- [Kos04] F. Koschnick. *Geometrische Lockingeffekte bei Finite Elementen und ein allgemeines Konzept zu ihrer Vermeidung*. PhD thesis, Technische Universität München, 2004.
- [KW91] M. Kleiber and C. Woźniak. *Nonlinear Mechanics of Structures*. Kluwer Academic Publishers, Warszawa, Poland, 1991.
- [Lee89] E.T.Y Lee. Choosing nodes in parametric curve interpolation. *Computer Aided Design*, 21(6):363–370, 1989.
- [Lin09] Johannes Linhard. *Numerisch-mechanische Betrachtung des Entwurfsprozesses von Membrantragwerken*. PhD thesis, Technische Universität München, 2009.
- [LOW95] Z. Lu, H. Obrecht, and W. Wunderlich. Imperfection sensitivity of elastic and elastic-plastic torispherical pressure vessel heads. *Thin-Walled Structures*, 23:21–39, 1995.
- [LWB07] J. Linhard, R. Wüchner, and K.-U. Bletzinger. "upgrading" membranes to shells. the ceg rotation free shell element and its application in structural analysis. *Finite Elements in Analysis and Design*, 44:63–74, 2007.
- [Lyc93] T. Lyche. *Knot insertion and Deletion Algorithms for B-spline Curves and Surfaces*. 1993.

- [MK95] W. Ma and J.P. Kurth. Parameterization of randomly measured points for least squares fitting of b-spline curves and surfaces. *Computer Aided Design*, 27(9):663–675, 1995.
- [MK98] W. Ma and J.-P. Kruth. Nurbs curve and surface fitting for reverse engineering. *The International Journal of Advanced Manufacturing Technology*, 14:918–927, 1998.
- [NBCS96] M. P. Nemeth, V. O. Britt, T. J. Collins, and J. H. Starnes. Nonlinear analysis of the space shuttle superlightweight external fuel tank. Technical Report 3616, National Aeronautics and Space Administration, Langley Research Center, Hampton, Virginia, 1996.
- [NW06] J. Nocedal and S. Wright. *Numerical Optimization*. Springer-Verlag, 2006.
- [NYCS02] M. P. Nemeth, R. D. Young, T. J. Collins, and J. H. Starnes. Effects of initial geometric imperfections on the non-linear response of the space shuttle superlightweight liquid-oxygen tank. *Int. J. Non-linear Mechanics*, 37:723–744, 2002.
- [Oeh98] M. Oehm. Numerisch effiziente gradientenberechnung von spannungsrestriktionen bezüglich der formvariablen. Studienarbeit, Universität-GH Siegen, 1998.
- [OR91] N. Olhoff and J. Rasmussen. Study of inaccuracy in semi-analytical sensitivity analysis - a model problem. *Structural Optimization*, 3:203–213, 1991.
- [Ora96] S. Oral. An improved semi-analytical method for sensitivity analysis. *Structural Optimization*, 11(1):67–69, 1996.
- [PD05] J. Pontow and D. Dinkler. Impefection sensitivity and limit loads of spherical shells under radial pressure. In *PAMM Proc. Appl. Mech*, volume 5, pages 253–254. WILEY-VCH Verlag GmbH & Co. KGaA, Weinheim, 2005.
- [Pie89] L. Piegl. Modifying the shape of rational b-splines. part 1: curves. *Computer Aided Design*, 21(10):509–518, 1989.
- [Pol97] E. Polak. *Optimization, Algorithms and Consistent Approximations*. Springer-Verlag, 1997.
- [PT97] L.A. Piegl and W. Tiller. *The NURBS book*. Springer-Verlag, Berlin, 1997.
- [PT00a] L. A. Piegl and W. Tiller. Curve interpolation wiht arbitrary end derivatives. *Engineering with Computers*, 16:73–79, 2000.
- [PT00b] L. A. Piegl and W. Tiller. Least-squares b-spline curve approximation with arbitrary end derivatives. *Engineering with Computers*, 16:109–116, 2000.
- [PT00c] L. A. Piegl and W. Tiller. Reducing control points in surface interpolation. *IEEE Computer Graphics and Applications*, 20:70–74, 2000.
- [PT00d] L. A. Piegl and W. Tiller. Surface approximation to scanned data methods in applied mechanics and engineering. *The Visual Computer*, 16:386–395, 2000.

- [PT02] L. A. Piegl and W. Tiller. Surface skinning revised. *The Visual Computer*, 18:273–283, 2002.
- [RCC08] M. Ritto-Correa and D. Camotin. On the arc-length and other quadratic control methods: Established, less known and new implementation procedures. *Computers & Structures*, 86:1353–1368, 2008.
- [Rei94] R. Reitinger. *Stabilität und Optimierung imperfektionsempfindlicher Tragwerke*. PhD thesis, Institut für Baustatik der Universität Stuttgart, 1994.
- [Rik84] E. Riks. Some computational aspects of the stability analysis of nonlinear structures. *Computer Methods in Applied Mechanics and Engineering*, 47:219–259, 1984.
- [Rog01] D. F. Rogers. *An Introduction to NURBS*. Morgan Kaufmann Publishers, 2001.
- [RR95] R. Reitinger and E. Ramm. Buckling and imperfection sensitivity in the optimization of shell structures. *Thin-Walled Structures*, 23:159–177, 1995.
- [SAS06] S.M. Shamsuddin, M.A. Ahmed, and Y. Samian. Nurbs skinning surface for ship hull design based on new parameterization method. *Int. J. Manuf. Technol.*, 28:936–941, 2006.
- [Sch95] G. Schuhmacher. *Multidisziplinäre, fertigungsgerechte Optimierung von Faserverbund-Flächentragwerken*. PhD thesis, Fachbereich Maschinentechnik der Universität-Gesamthochschule Siegen, 1995.
- [Sch00] H. Schmidt. Stability of steel shell structures general report. *Journal of Constructional Steel Research*, 55:159–181, 2000.
- [SF00] M. F. Sintef and M. S. Floater. Meshless parameterization and b-spline surface approximation. In *The Mathematics of Surfaces IX*, 2000.
- [Spe05] G. Spenninger. Konstruktion und berechnung drapierter multiaxialgelege am beispiel einer rumpfschottmembran. Master’s thesis, EADS Militärflugzeuge München, Abteilung MT212, Structural Concepts, 2005.
- [SR84] K. Schweizerhof and E. Ramm. Displacement dependent pressure loads in nonlinear finite element analyses. *Computers & Structures*, 18(6):1099–1114, 1984.
- [SW03] C. G. Small and J. Wang. *Numerical Methods for Nonlinear Estimating Equations*. Oxford university press, 2003.
- [Tok00] Y. Tokuyama. Skinning-surface generation based on spine-curve control. *The Visual Computer*, 16:134–140, 2000.
- [Wei00] Y. Başar D. Weichert. *Nonlinear Continuum Mechanics of Solids*. Springer-Verlag, Berlin, 2000.
- [WFC08] W. Wall, M. Frenzel, and C. Cyron. Isogeometric structural shape optimization. *Computer methods in applied mechanics and engineering*, 197:2976–2988, 2008.

- [Woo88] C. Woodward. Skinning techniques for interactive b-spline interpolation. *Computer Aided Design*, 20(10):441–451, 1988.
- [Wri01] P. Wriggers. *Nichtlineare Finite-Element-Methoden*. Springer-Verlag, Berlin, 2001.
- [Wüc07] R. Wüchner. *Mechanik und Numerik der Formfindung und Fluid-Struktur-Interaktion von Membrantragwerken*. PhD thesis, Technische Universität München, 2007.
- [Yan05] P. I. Yanev. *Numerical algorithms for estimating least squares problems*. PhD thesis, Institut d’informatique université de Neuchâtel Switzerland, 2005.
- [ZT05] O.C. Zienkiewicz and R.L. Taylor. *The Finite Element Method*. Elsevier Butterworth-Heinemann, Burlington, MA, USA, sixth edition, 2005.